Investigation of ion-track morphology and annealing behavior using small-angle X-ray scattering

Boshra Afra

A thesis submitted for the degree of
Doctor of Philosophy
The Australian National University

May 2013

Declaration

This thesis is an account of research undertaken between June 2009 and May 2013 at the Department of Electronic Materials Engineering, Research School of Physics and Engineering, College of Physical and Mathematical Sciences, The Australian National University, Canberra, Australia.

Except where acknowledged in the customary manner, the material presented in this thesis is, to the best of my knowledge, original and has not been submitted in whole or part for a degree in any university.

Boshra Afra
May 2013

To mum and dad for the limitless
effort they put into my education.

تقدیم به مامان و بابا به خاطر زحمت
بی اندازه ای که برای تحصیل من کشیدند.

Acknowledgements

The past few years were probably the most challenging years of my life so far. The best and worst moments of my PhD journey have been shared with many people and I would like to thank everyone who in one way or another contributed to this thesis.

Firstly I would like to thank Dr. Patrick Kluth for giving me the opportunity to become a PhD under his supervision. Thanks Patrick for transforming my research interests into something concrete and fundamentally important in the field of materials science and guiding me through the rapids of this exciting intellectual exploration. Thank you for all the advice, ideas, inspiration, moral support and patience.

I am indebted to Prof. Mark Ridgway for sharing his experience, knowledge and wisdom and for the discussions that never failed to provide me with encouragement and new direction. I would also like to express my appreciation to Prof. Aidan Byrne for his insights and keeping his interest in my work despite his busy schedule.

I very much enjoyed the interactions and fruitful discussions I had with Profs. Christina Trautmann, William Weber, Marcel Toulemonde, Kai Nordlund, Rod Ewing, and Drs. Maik Lang, Olli Pakarinen, and Flyura Djurabekova. Thank you for your interest in my project and for your valuable collaboration.

The work undertaken in this thesis is profoundly benefited from the Australian Synchrotron. I am grateful for all the beam times, the excellent free coffee essential for the night shifts and the support from all the staff specially the SAXS/WAXS beam line scientists, Nigel, Stephen, and Adrian.

My sincere thanks go to Raquel and David S. for their kind support from day one, their invaluable experiences they shared with me, their warm friendship, and for securing a place where I could rest my fatigued mind. Also many thanks to Thomas, David L., Leandro, Felipe, Stefan, and all the past and present EME members, my friends and colleagues.

Special thanks to best sister ever, Hoda, and to Mehrdad for their love, optimism and support.

Finally and most importantly, I would like to thank the love of my life, my dearest husband, Mahdi. He knows why.

Abstract

When heavy ions with energies in the range of hundreds of MeV to GeV penetrate a solid, they lose their energy through inelastic interactions with the target electrons and can leave narrow cylindrical trails of permanent damage along their path, known as ion tracks. Ion tracks are typically a few nanometers in diameter and can be up to tens of micrometers long. When these tracks are annealed at elevated temperatures, they shrink in size and eventually the damage inside the material can recover. In this project ion tracks are studied in Durango apatite, San Carlos olive and synthetic quartz. In minerals such as apatite track formation can result from spontaneous fission of naturally occurring uranium inclusions that produces high energetic fragments. These so called "fission-tracks" are used for dating and constraining the thermal history of geological samples. The current dating methods, however, utilize chemical etching, which destroys the primary damage such that essential information on the actual scale of the underlying radiation damage is irrevocably lost. A detailed understanding of the un-etched track damage in minerals and its dependence on geologically relevant conditions is of fundamental importance for the application of etched tracks in geo- and thermochronology. Tracks in olivine are used for identification of cosmic rays in meteorites. Many meteorites contain different amounts of olivine which is a crystalline mineral susceptible to ion-track formation from high energetic cosmic particles. Studying the annealing behavior of ion tracks in meteorites can lead to estimation of the temperature of the mineral during track formation. In quartz, swift heavy ion irradiation leads to a change in the refractive index of the material inside the narrow tracks and provides new possibilities for fabrication and micromachining of optical devices. Annealing of ion tracks in quartz is of interest as for example device fabrication processes often involve elevated temperatures.

In this work synchrotron-based small-angle X-ray scattering in combination with *in situ* and *ex situ* annealing experiments is used to study the morphology and damage recovery of un-etched ion tracks. It is demonstrated that SAXS is a powerful tool for studying ion-track damage in a variety of materials as it is sensitive to small density changes at the nanometer scale that often occur in the damaged regions. It is a non-destructive technique and can be used to determine changes in the track radii with sub-nanometer precision. Short acquisition times make it well suited for studying track annealing kinetics *in situ*.

In all three materials, the scattering intensities of the tracks are best fitted with a cylindrical model with a constant density and sharp track boundaries consistent with amorphous material inside the track.

In quartz, analysis of the SAXS data at room temperature indicated a weak dependence on the electronic energy loss at values above 17 keV/nm, in contrast to values previously reported from Rutherford backscattering spectrometry measurements and predictions from an inelastic thermal spike model. The observed discrepancies are discussed with respect to the formation of a defective halo around an amorphous track core, the existence of high stresses and/or the possible presence of a boiling phase in quartz predicted by the thermal spike model. Annealing of ion tracks in quartz revealed a complex behavior: below 600 °C a small yet reproducible variation in the track radius is described by an analytical model considering the ion tracks as cylindrical elastic inclusions and the temperature dependence of the elastic constants of amorphous SiO_2 and quartz as the track and matrix material, respectively. At temperatures above 800 °C, re-crystallisation of the amorphous damage is apparent and the tracks start to shrink in size. Isothermal annealing of the tracks at three temperatures above 800 °C yields an activation energy of approximately 4.6 eV which is comparable with previously reported values for epitaxial regrowth of amorphised quartz.

In apatite and olivine, SAXS measurements of ion tracks indicate a similar increase in the radius with the electronic energy loss as well as a similar change in the electron density of ∼1% of the tracks compared to their matrix. However, annealing of ion tracks in the both minerals revealed a different damage recovery behavior. In both minerals, annealing leads to a gradual decrease of the track radius consistent with re-crystallisation of the amorphous material. The damage recovery rate, however, is significantly smaller in olivine compared to apatite, despite the initially very similar track morphology. In apatite, damage recovery of the tracks is characterised by structural relaxation followed by recrystallization with an activation energy of approximately 0.72 eV. In olivine, full recovery of the track damage also involves fragmentation of the cylindrical tracks above the temperate of about 600 °C and possibly oxidation of the material.

The work presented in this thesis has aided in developing the possibilities that small-angle X-ray scattering can provide for studying the morphology and annealing behavior of nano sized damage structures. The high accuracy with which the track radii can be determined using SAXS, the nondestructive, artifact-free measurement methodology, as well as the data analysis models introduced in this work provide an effective means for in-depth studies of ion-track morphology and annealing behavior in a variety of materials.

Publications

Measurements of ion tracks in metallic glasses by small angle x-ray scattering
M.D. Rodriguez, C. Trautmann, **B. Afra**, R. Giulian, N. Kirby, and P. Kluth
GSI Scientific Report 2009, MATERIALS-06, p. 428.

Ion Track Annealing Kinetics in Apatite
B. Afra, M. Lang, M.D. Rodriguez, N. Kirby, R.C. Ewing, C. Trautmann, and P. Kluth
GSI Scientific Report 2010, PNI-MR-05, p. 373.

Annealing Studies on Ion Tracks in Metallic Glasses
M.D. Rodriguez, **B. Afra**, C. Trautmann, N. Kirby, and P. Kluth
GSI Scientific Report 2010, PNI-MR-06, p. 374.

Annealing kinetics of latent particle tracks in Durango apatite
B. Afra, M. Lang, M.D. Rodriguez, J. Zhang, R. Giulian, N. Kirby, R.C. Ewing, C. Trautmann, M. Toulemonde, and P. Kluth
Physical Review B: Condensed Matter and Materials, 83, 064116 (2011) 1-5.

Ion Tracks in Amorphous $Fe_{80}B_{20}$*: The Effect of Pre-Irradiation Annealing*
M.D. Rodriguez, C. Trautmann, **B. Afra**, N. Kirby, and P. Kluth
GSI Scientific Report 2011, PNI-MR-04, p. 402.

SAXS study of ion tracks in San Carlos olivine and Durango apatite
B. Afra, M.D. Rodriguez, M. Lang, R.C. Ewing, N. Kirby, C. Trautmann, and P. Kluth
Nuclear Instruments and Methods in Physics Research: Section B, 286 (2012) 243-246.

Morphology and annealing kinetics of ion tracks in minerals
P. Kluth, **B. Afra**, M.D. Rodriguez, M. Lang, C. Trautmann, and R. C. Ewing
The European Physical Journal, Heavy Ion Accelerator Symposium on Fundamental and Applied Science, 35, 03003 (2012).

Modification of Fe-B based metallic glasses using swift heavy ions
M.D. Rodriguez, C. Trautmann, M. Toulemonde, **B. Afra**, T. Bierschenk, R. Giulian, N. Kirby and P. Kluth
The European Physical Journal, Heavy Ion Accelerator Symposium on Fundamental and Applied Science, 35, 03004 (2012).

Morphology of swift heavy ion tracks in metallic glasses
M.D. Rodriguez, **B. Afra**, C. Trautmann, M. Toulemonde, T. Bierschenk, J. Leslie, R. Giulian, N. Kirby, and P. Kluth
Journal of Non-Crystalline Solids, 358 (2012) 571-576.

SAXS investigations of morphology of swift heavy ion tracks in α-quartz
B. Afra, M. D. Rodriguez, C. Trautmann, O. H. Pakarinen, F. Djurabekova, K. Nordlund, T. Bierschenk, R. Giulian, M. C. Ridgway, G. Rizza, N. Kirby, M. Toulemonde and P. Kluth
Journal of Physics: Condensed Matter, 25 (2013) 045006.

The influence of swift heavy ion irradiation on the recrystallization of amorphous $Fe_{80}B_{20}$
M.D. Rodriguez, **B. Afra**, C. Trautmann, N. Kirby, and P. Kluth
Microelectronic Engineering, 102 (2013) 64-66.

Effect of doping on the radiation response of conductive $Nb - SrTiO_3$
W. X. Li, M. D. Rodriguez, P. Kluth, M. Lang, N. Medvedev, M. Sorokin, J. Zhang, **B. Afra**, M. Bender, D. Severin, C. Trautmann, and R. C. Ewing
Nuclear Instruments and Methods in Physics Research: Section B, 302 (2013) 40-47.

Tracks and voids in amorphous Ge induced by swift heavy ion irradiation
M. C. Ridgway, T. Bierschenk, R. Giulian, **B. Afra**, M. D. Rodriguez, L. L. Araujo, A. P. Byrne, N. Kirby, O. H. Pakarinen, F. Djurabekova, K. Nordlund, M. Schleberger, O. Osmani, N. Medvedev, B. Rethfeld, and P. Kluth
Physical Review Letters, 110, 245502 (2013).

Temperature dependent formation of ion tracks in natural quartz and apatite
D. Schauries, M. Lang, O. H. Pakarinen, S. Botis, **B. Afra**, M. D. Rodriguez, K. Nordlund, D. Severin, M. Bender, C. Trautmann, R. C. Ewing, N. Kirby, and P. Kluth
Journal of Applied Crystallography, Accepted (2013).

Latent ion tracks in amorphous silicon
T. Bierschenk, R. Giulian, **B. Afra**, M.D. Rodriguez, D. Schauries, S. Mudie, O.H. Pakarinen, F. Djurabekova, K. Nordlund, O. Osmani, N. Medvedev, B. Rethfeld, M.C. Ridgway, and P. Kluth
Physical Review Letters, Submitted.

Effect of electronic energy loss on ion track formation in amorphous Ge
T. Bierschenk, **B. Afra**, M.D. Rodriguez, R. Giulian, C. Trautmann, S. Mudie, M.C. Ridgway, and P. Kluth
Nuclear Instruments and Methods in Physics Research: Section B, Submitted.

Annealing behavior of ion tracks in olivine, apatite, and britholite
B. Afra, M. Lang, T. Bierschenk, M.D. Rodriguez, W.J. Weber, C. Trautmann, R.C. Ewing, N. Kirby, and P. Kluth
Nuclear Instruments and Methods in Physics Research: Section B, Submitted.

The shape of ion tracks in natural apatite
D. Schauries, **B. Afra**, T. Bierschenk, M. Lang, M.D. Rodriguez, C. Trautmann, W. Li, R.C. Ewing, and P. Kluth
Nuclear Instruments and Methods in Physics Research: Section B, Submitted.

Contents

List of Figures

List of Tables

Chapter 1

Introduction

1.1 Background

The fission reaction of radioactive atoms was first discovered by Hahn and Strassmann in 1939 [1]. In a fission reaction, the unstable nucleus splits into two daughter nuclides. These fragments are often asymmetric, resulting in nuclides of unequal masses. The masses of the fission fragments often consist of heavy (M_H) and light (M_L) nuclei. The mass ratio between the fragments, (M_H/M_L), can vary between 2, in the extreme case, and 1.4, which is the most frequent scenario [1]. The masses of fission products cover a broad distribution. For instance, for the fission of ^{238}U, typical light masses have mass numbers ranging from 85-105 and heavy masses ranging from 135-155 [1].

Minerals such as apatite and zircon can incorporate and retain small amounts of uranium and thorium [2, 3] which are radioactive and decay spontaneously or by bombardment with particles such as neutrons or protons. The spontaneous fission of ^{238}U releases a kinetic energy of about 170 MeV and produces two energetic nuclear fragments [4] that move at 180° away from each other. These high energetic particles slow down in matter predominantly by electronic excitations and ionisations and can induce narrow trails of highly-damaged material so called “fission tracks” [5, 6, 1] which are about 10 nm in diameter and up to 20 μm long. This process is shown schematically in figure 1.1.

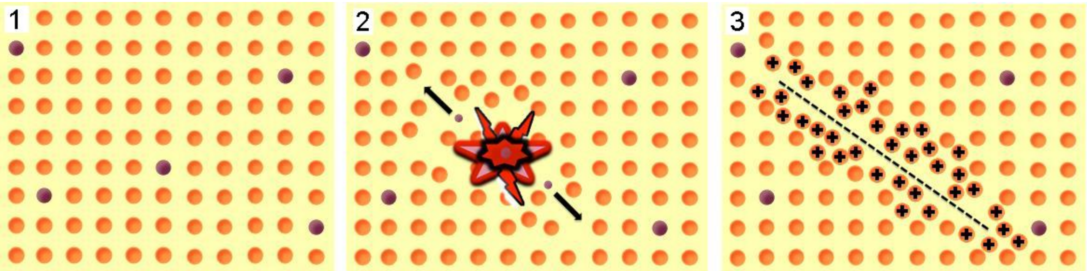

Figure 1.1: Schematic presentation of the formation of fission tracks in minerals [4]. (1) Small amounts of an unstable radioactive content e.g. ^{238}U are presented in different color. (2) Spontaneous fission of ^{238}U produces two highly-charged heavy particles which result in further deformation of the lattice. (3) As the fission particles slow down they leave a damage trail or fission track.

In many crystals when a track is exposed to elevated temperatures, atomic motion in the solid can lead to a restoration of the original structure and cause the damage track to fade away [7]. Hence, at elevated temperatures tracks can shrink in size, and fragment into sections until they are completely annealed [6, 1]. Given the well-known decay laws, the number density of tracks correlated with the specific uranium content can be used as a measure of the age of archaeological and geological samples and the track-length distribution yields information on its thermal history [8, 9, 10, 4, 11]. Assuming that the temperature of a fission track at the time of formation was below the temperature at which fading begins, it will be stable over millions of years [7].

The first fission tracks were detected in mica by Silk and Barnes in 1959 [12] when they mounted sheets of mica against a thin layer of uranium, exposed the sandwich to thermal neutrons in a reactor, stripped thin layers from the mica, and examined them in an electron microscope [13]. It was a great discovery but there was the problem of track fading under the electron beam. A few years later Price and Walker [13, 14, 5] solved the annealing problem by immersing the mica in hydrofluoric acid and "fixing" the tracks by removing the cylindrical regions of radiation damage and enlarging them to micrometer sizes such that they can be imaged using conventional optical microscopy. This etching process forms the basis of the fission track dating technique developed in 1963 [5]. Taken together with other techniques, fission track dating is used to infer rates of tectonic uplift and landscape evolution [15]. The most commonly used materials for fission track dating are apatite, zircon, and sphene. Examples of etched fission tracks in apatite are shown in figure 1.2 [16]. The fission tracks in a crystal of apatite were etched for 20 s in nitric acid [16].

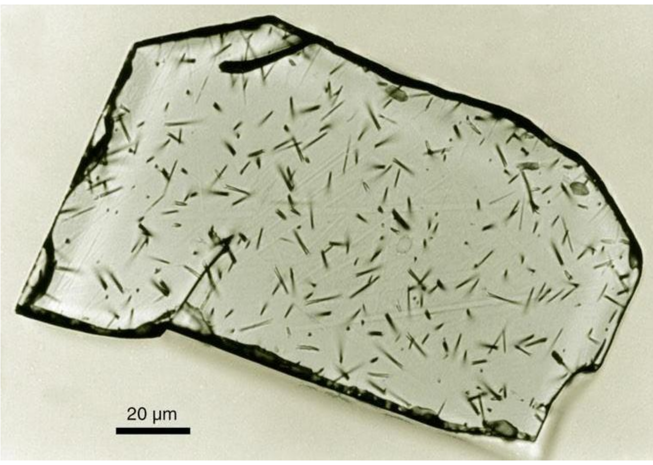

Figure 1.2: Optical microscopy image of etched fission tracks in apatite. The image is taken by Prof. Andrew Gleadow from the University of Melbourne [16].

The advent of large ion accelerator facilities in the 80's enabled the controlled formation of ion tracks in the laboratory and stimulated investigation of ion tracks in many materials. Despite the considerable efforts in ion track research, to date no consistent theory of track formation has been developed. As with minerals it was found that chemical etching preferentially attacks the radiation-damaged volume in the undamaged bulk [17]. However, chemical etching completely erases the initial damage structure to form hollow channels with high aspect ratios suitable for a variety of technological applications in different areas of science including (but not limited to) material modifications and fabrication, nuclear waste management, archeology, geochronology, and development of medicine, biochemical products and optical devices. For applications as well as for a comprehensive understanding of track formation, it is of major importance to understand the formation and stability of tracks at the actual scale of the underlying radiation damage.

The most important parameter for ion-track formation and the resulting track structure is the energy loss per unit path length (dE/dx) of the projectile ion as it travels through the material. For a given material, dE/dx depends on the energy, mass number, and charge state of the projectile. For a typical fission fragment for example in apatite, this parameter is about 16 keV/nm. Spontaneous fission produces fragments with a relatively broad mass and energy distribution that causes variation in the initial dE/dx value and thus may lead to different damage morphologies and sizes for individual fission tracks. The random decay direction induces tracks of different crystallographic orientations, which may also influence the resulting track damage. Other factors that can influence the track structure include pressure, temperature, and composition of the material. Only a consistent microstructural description of track properties at the atomic level (prior to chemical etching) can provide the fundamental understanding required for the application of etched fission tracks for dating purposes [1]. Therefore, detailed characterization of the track structure and size and its systematic dependence on a number of geologically relevant parameters is simplified and more accurate with well-controlled parallel "ion tracks" of identical size and damage morphology. Examples of induced ion tracks in apatite in cross-section and plan-view are shown in figure 1.3 [18].

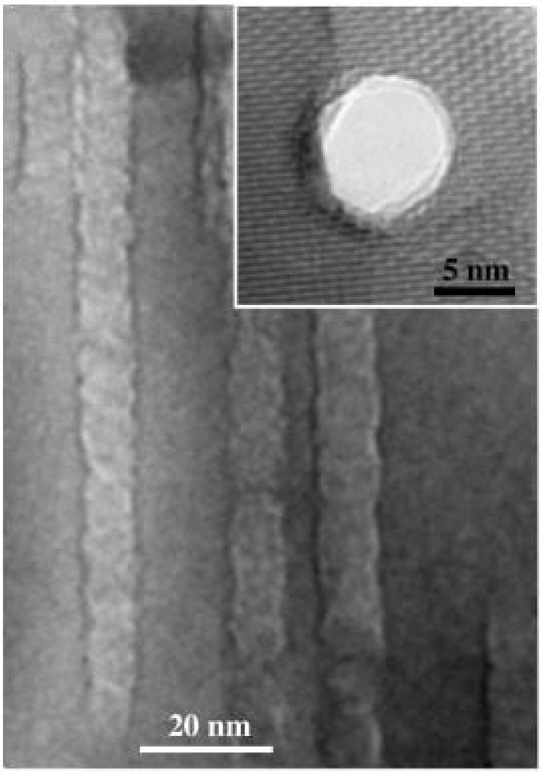

Figure 1.3: Cross-sectional transmission electron microscopy (TEM) image of latent tracks in apatite induced by 2.2 GeV Au ions. The inset shows a high-resolution TEM image of an ion track in plan-view. The image is taken from reference [18].

Similar to fission tracks, in many materials, ion tracks can change upon heat treatment ultimately leading to recovery of the ion-track damage. Therefore annealing experiments of ion tracks are important for various reasons such as identification of the origins of tracks in terrestrial materials [19], changing the threshold for track registration in solid state track detectors [20], understanding the stability of fission tracks to unravel erosion and transport patterns of sedimentary rocks [4] and many other applications. A detailed understanding of annealing behavior and recovery kinetics of ion tracks is therefore of great fundamental and technological interest.

1.2 Ion track applications

There are numerous applications of swift heavy ion tracks in different materials spanning many fields of research and technology. Here we focus on applications for fission track dating and some technological as well as space applications motivated by the relevance of the materials studied in this work.

1.2.1 Fission track dating

One of the important applications of ion tracks is their use for fission track dating which is used to determine the age of archaeological and geological samples as well as their thermal history. Like any radioactive decay process, by knowing the decay rate and the relative abundance of the parent and daughter product, the age of the material can be estimated. Spontaneous fission tracks are mostly generated by the fission of ^{238}U as the fission half-life of all other naturally-occurring isotopes such as ^{235}U and ^{232}Th are too long to produce significant number of tracks. Here the parent and daughter products are the number of ^{238}U atoms and the number of spontaneous fission tracks per unit volume [4].

One of the techniques for determining a fission track age is the external detector method [21] which is summarised and illustrated in figure 1.4 [4]. In this method the surface of a given mineral is polished and by etching, surface tracks are revealed and their content is estimated. The surface is then sealed with a uranium-free detector such as muscovite mica and is sent to a nuclear reactor. The sample is irradiated with low-energy thermal neutrons which induces fission of ^{235}U. Some heavy particles cross the interface between the mineral and the detector on the top as a result of fission of ^{235}U and produce a mirror image of the original grain. Induced tracks can be etched in the mica layer and by counting the number of induced tracks, the concentration of ^{235}U in the sample can be determined. As the ratio between ^{235}U and ^{238}U is constant in nature, we can estimate the abundance of ^{238}U or the parent product. The number of fission tracks together with the ^{238}U content then yield the age of the mineral.

Naturally-occurring tracks in different minerals progressively anneal at a rate which depends on the temperature [6, 22]. Since the discovery of fission tracks, a lot of work is dedicated to studying the effect of annealing and it has been shown that the track-length distribution under temperature yields information on the thermal history of the material [8, 9, 10, 4, 11]. In nature, younger fission tracks experience smaller portion of the time-temperature history of the mineral. Therefore, older fission tracks in a mineral have experienced a greater degree of partial annealing than younger tracks. The overall fission track length distribution is indicative of the thermal history of the mineral [23].

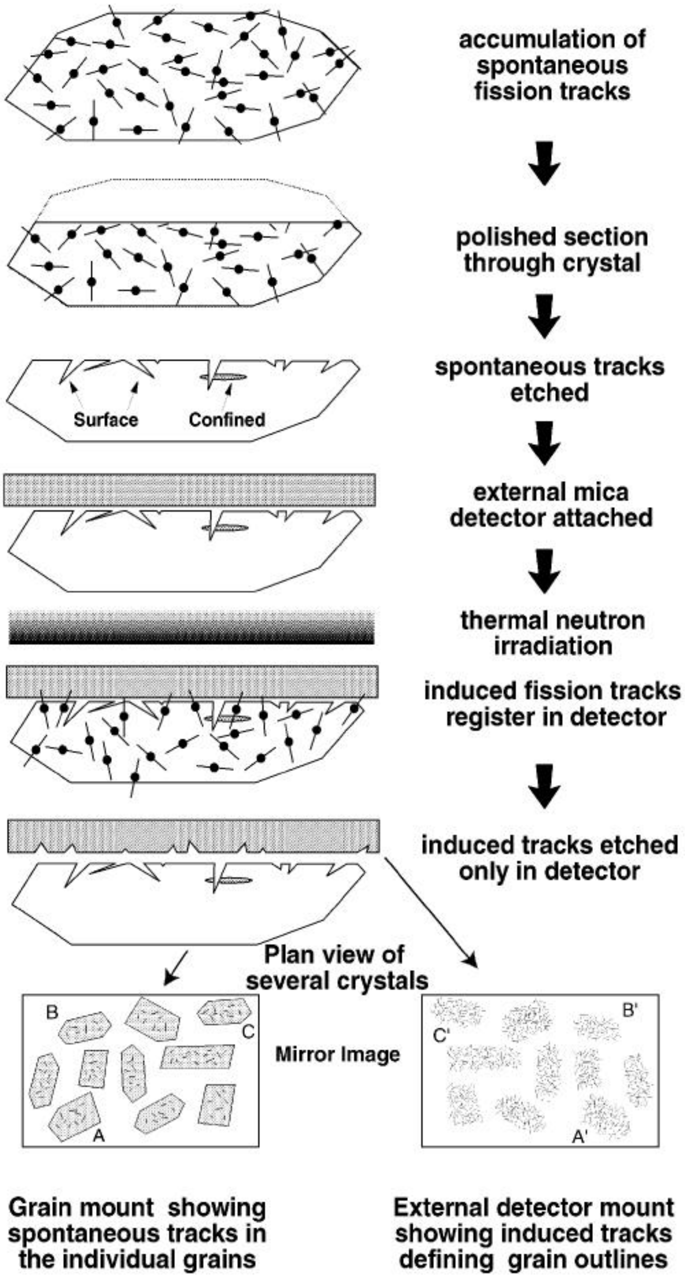

Figure 1.4: The external detector method for fission track dating [21, 4]. The picture is taken from reference [4].

1.2.2 Technological applications

One of the very first applications of ion tracks was in membrane technology where small particles suspended in a liquid or gas could be mechanically separated by passing through ion track filters [24]. Ion track filters are advantageous over the conventional filters due to their well-defined pore size. Micro- and ultra-filtration membranes produced in thin polymeric films using the SHI irradiation and chemical etching have found their place in the market since the seventies and their applications include filtration of beverages, separation and concentration of various suspensions and purification of deionized water in microelectronics processing [25]. Figure 1.5 shows an example of nanoporous membranes formed by etching of an ion irradiated polymer foil [26]. Nanofilters prepared using ion track pores can also be used as templates for the synthesis of micro and nanowires [25, 27, 28, 29]. The template method is shown schematically in figure 1.6.

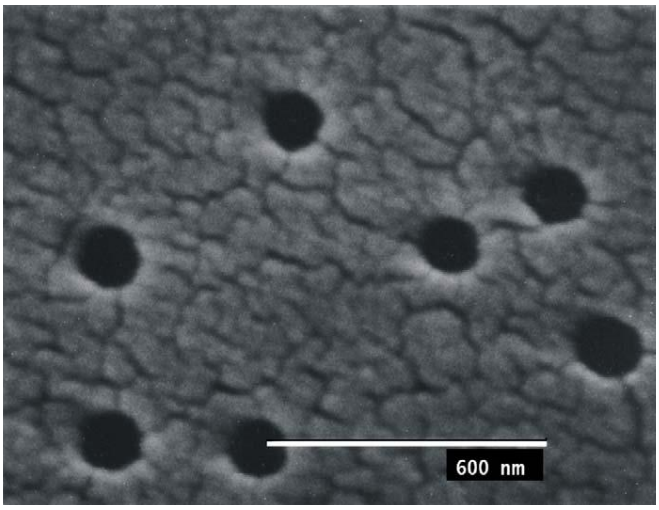

Figure 1.5: Image of polymide foil after irradiation and etching. The image is taken from reference [26].

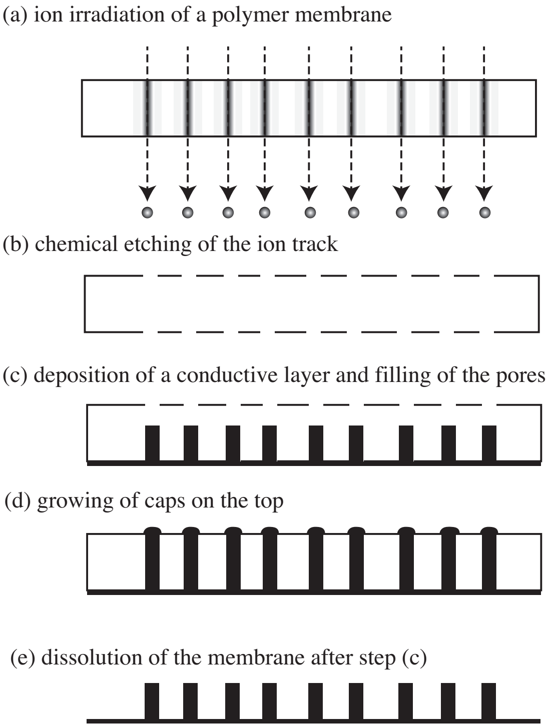

Figure 1.6: Schematic of the template method for nanowire fabrication [27].

Another use of ion tracks for technological applications is in lithography. Micromachining by ion track etching (MITE) enables new geometries and deep microstructures used for micromachining of crystals, glasses and polymers [30]. Swift heavy ion tracks in dielectric materials offer unique possibilities for generation of nanometer-sized structures at low cost and high throughputs. In combination with lithography they open up new ways for biofluidic, electric, magnetic and optic device fabrication. Comparison of conventional etching and the MITE technique is shown in figure 1.7 [30].

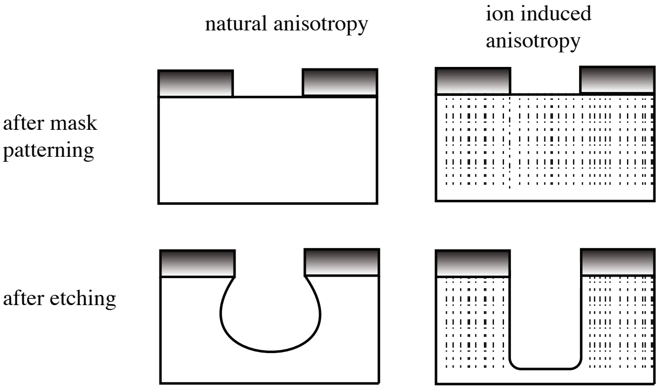

Figure 1.7: Comparison of conventional etching and micromachining by ion track etching.

One of the important materials which is used in micromachining and for fabrication of optical waveguides is quartz (crystalline SiO_2). Swift heavy ion irradiation of quartz leads to a change in the refractive index and offers a means to impose an etch anisotropy in the material [31, 32]. An example of some geometries in quartz that are only possible by MITE is shown in figure 1.8 which shows deep structures with close to vertical walls [33].

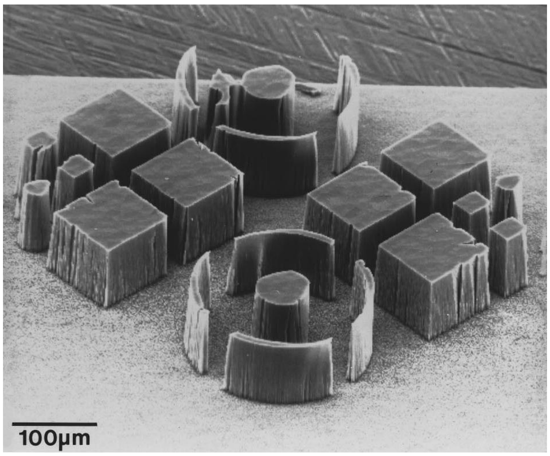

Figure 1.8: Examples of geometries created using micromachining by ion track etching in quartz [33]. The image is taken from reference [33].

1.2.3 Space applications

Figure 1.9 shows the helmet that was worn by astronaut James Lovell in the Apollo 8 mission and images of cosmic-ray particle track replicas [34, 35]. The tracks were caused by heavy cosmic rays that penetrated the Apollo helmets and provide a measure of the dose and variations of the cosmic radiation that the astronauts are exposed to [34, 35, 36]. The helmets are made of Lexan plastic and this material is particularly important since the ionization rate necessary to produce a track in Lexan is close to that for which a nuclear particle crossing certain cells will kill the cell with the probability of almost one [35, 34]. Therefore from such track measurements, the total brain cell damage in an extended space mission can be estimated [36].

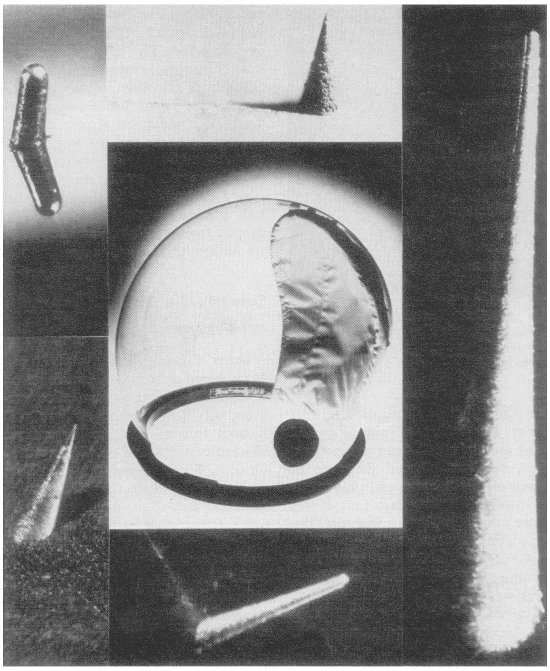

Figure 1.9: Apollo helmet and cosmic-ray particle track replicas. The image is taken from reference [35].

Ion tracks are also used for identification of cosmic rays in meteorites, objects that originate in outer space and survive impact with the Earth's surface. Meteorites may contain olivine which is a crystalline mineral susceptible to ion-track damage. Studying the tracks inside the olivine from meteorites provides information about the chemical composition of ultraheavy cosmic rays [37].

1.3 Measurement techniques

First observations of ion tracks were by means of microscopy [38, 12]. Visual images from microscopic observations have the advantage of corresponding directly to human intuition. Depending on the contrast, ion tracks can be imaged using different microscopy techniques. The conventional method for observing individual tracks uses chemical etching which is based on the higher chemical reactivity of the track material. By etching in a suitable agent, tracks are enlarged to pores of micrometer sizes accessible to optical microscopy. Figure 1.10 shows a micrograph of etched tracks in Lexan polycarbonate that was taken by an optical microscope [39]. Optical microscopy requires very little sample preparation, however, it has a small depth of focus and the nanometer size of un-etched "latent" tracks is beyond its resolution.

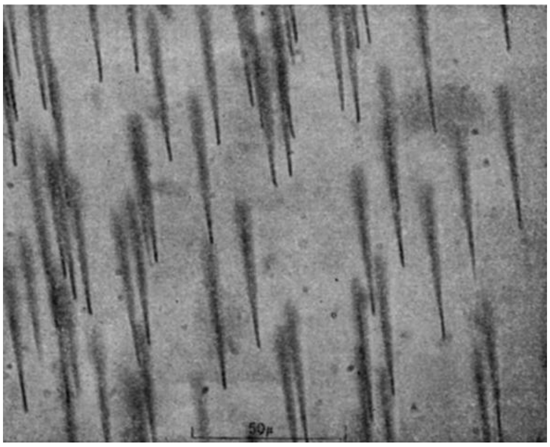

Figure 1.10: Etched tracks in Lexan polycarbonate, an example of optical microscopy for imaging ion tracks. The image is taken from reference [39].

Etched tracks can also be imaged using scanning electron microscope (SEM) which has a resolution about two orders of magnitudes higher than optical microscopy [40]. SEM can image the surface of a sample by scanning it with a beam of electrons in a raster scan pattern and recording the secondary electrons excited at each point. An image of the surface topology can be reconstructed with a resolution of down to few nanometers depending on the beam energy and the material. Figure 1.11 shows an SEM image of etched tracks in $a - SiO_2$ [41].

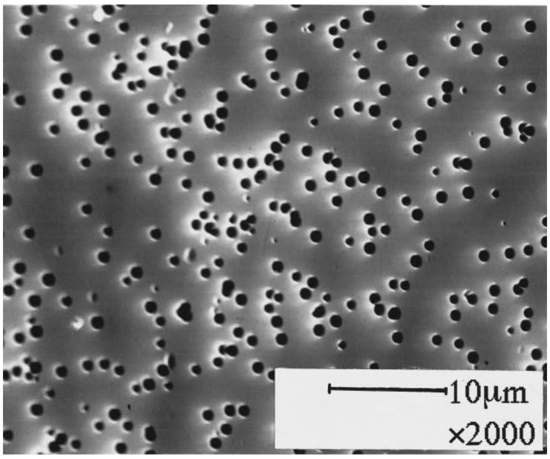

Figure 1.11: SEM image showing the etched surface of amorphous SiO_2 irradiated with 76.4 MeV I ions. The image is taken from reference [41].

High-resolution visualization of latent ion tracks and very fine etched tracks can be performed using transmission electron microscopy (TEM) [42, 43], where a beam of electrons is transmitted through a very thin sample and forms an image as a result of the interaction of the electrons with the material. Using TEM, tracks can be imaged in both plan-view and cross-section. Examples of plan-view and cross-sectional TEM images of latent ion tracks are shown in figure 1.12 [44, 45].

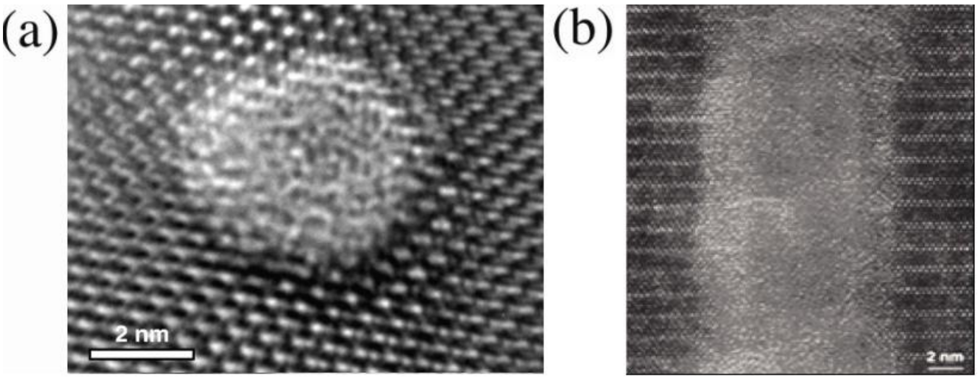

Figure 1.12: (a) Plan-view high-resolution TEM image of zircon irradiated with 10 GeV Pb ions. The image is taken from reference [44]. (b) Cross-section TEM image of thin film of $Bi_2Sr_2CaCu_2O_8$ irradiated with 200 MeV Ca ions. The image is taken from reference [45].

The powerful magnification of advanced TEMs allow for detailed study of ion tracks in a variety of materials and provide information about the total track dimensions, shape, and crystal structure. However, in some materials such as apatite and quartz, the measurement can be very difficult as tracks are susceptible to the electron beam [46, 47] and they might be modified during imaging. Sample preparation for TEM should also be done with great care as the complex processes required for thinning down the samples can potentially induce artifacts. Furthermore, only small areas can be imaged which contain few tracks such that statistical information is limited.

Ion-track damage can also be measured on a macroscopic scale by using for example X-ray diffraction (XRD) or channeling Rutherford backscattering spectrometry (RBS/C). In such techniques measurements of for example the amorphous or disordered fractions is performed as a function of irradiation fluence and by assuming cylindrical track cross-sections, track radii can be deduced [48, 49, 50]. In this way, only average track properties are assessable. Furthermore, these techniques cannot be used to derive the track morphology when ion tracks become discontinuous or deviate from cylindrical shapes. In RBS, the depth of the probing beam in the sample is typically limited to <1 μm from the surface, and to yield the damaged fraction of the material, samples which are irradiated in a range of medium to high fluences are needed.

To investigate track formation by RBS, XRD and TEM, generally crystalline materials are required. Tracks in amorphous materials (e.g. amorphous SiO_2 or metallic glasses) are inherently difficult to measure due to the lack of crystallinty that yield diffraction (in XRD and TEM) and contrast for channelling experiments (RBS/C).

In some solids such as quartz, swift heavy ion irradiation can induce damage in the bulk as well as modifications on the surface. For example under suitable conditions, each ion impact produces a nanometric hillock on the quartz surface [51]. Atomic force microscopy (AFM) allows direct observation of solid surfaces at the nanometric scale. In some studies, the radii of the cross section of the surface hillocks are correlated with ion track radii [52]. Figure 1.13 shows an AFM image of quartz irradiated with high-energy Pb ions [52]. Even though AFM images can clearly show the conical damage on top of ion tracks, it is difficult to deconvolute the size of the surface hillocks from the measurements because of the AFM tip sizes and reproducibility problems when using different types of tips [53]. Furthermore, the hillock structure may not necessarily represent properties of the track in the bulk.

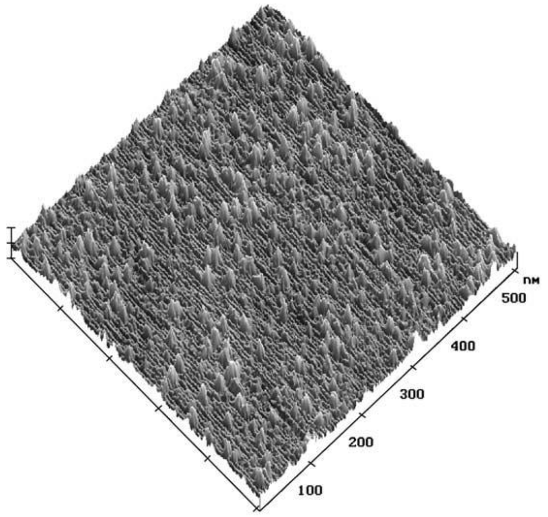

Figure 1.13: AFM image of a quartz surface irradiated with 1.3 GeV Pb ions. The image is taken from reference [52].

More recently, tracks have been measured with beams of X-rays and neutrons using small-angle scattering techniques (SAXS and SANS). SAXS and SANS are very similar in a sense that in both techniques elastic scattering of the incoming beam at small scattering angles is analysed to provide information about the size, shape and orientation of nano-sized objects in the sample. An important feature of the SAXS and SANS is their potential for analysing bulk materials with little sample preparation. They can be used for both amorphous and crystalline materials and the large sample volume probed (compared to microscopy techniques) yields very good statistics. The conceptual experiment and theory is the same for X-rays and neutrons, the differences are the physics of the X-ray (electro-magnetic radiation) versus neutron (neutral particle) interactions with matter. While X-ray scattering is sensitive to the electron density distribution of the target material, neutron scattering measures the scattering density distribution of the target nuclei. As there is not much absorption of hard X-rays by air at the typical energies used (e.g. 11-20 keV), SAXS does not require the sample to be in an evacuated chamber. However, X-rays do not interact strongly with the lighter elements. SANS gives a superior contrast for light elements than SAXS, but has the disadvantage of low flux of neutron sources compared to the orders of magnitude higher fluxes for X-ray sources. This requires relatively large amounts of sample material for SANS measurement.

In general, information that can be determined using SAXS include measurements of the size and shape of nanoparticles, polymers, proteins or micelles in solution; measurements of pore size and interpore spacing in mesoporous materials; characteristic length scales in partially ordered systems, e.g. block-copolymer composites; and interparticle interactions in colloidal dispersions. For example small-angle X-ray scattering (SAXS) is a widely used method to probe the micro- and nano-scale morphology of biological and soft materials [54, 55, 56]. Detailed imaging of many soft samples such as tissues can provide insight into the correlation between micro- and nano-level. Using high-resolution SAXS, a 3D tomography of soft tissue samples can be obtained providing insights into the structural organization at the nano-level [57, 58]. Another very important property of SAXS is its ability to measure solutions, something which cannot be done in vacuum environments required by some techniques (e.g. SEM). For this reason, SAXS is a highly-useful tool in the biological sciences because of its ability to resolve wet gels [59] and complex proteins [60]. Furthermore, SAXS can be used to investigate the nanostructure of inorganic materials such as nanohybrid polyimide (PI) [61] that is widely applied in electrical and electronic devices.

In the case of ion tracks, the damage in the material properties generally involves subtle changes in the atomic density and concomitantly electron density. These changes can be assessed by SAXS that measures the scattering of X-rays due to density fluctuations on length scales comparable to the lateral track dimensions in both crystalline and amorphous materials [62, 63, 46].

In this thesis, synchrotron-based SAXS is used as the main technique for studying swift heavy ion tracks as it is a non-destructive technique which can measure ion tracks in bulk samples, provides good statistics about ensembles of tracks, does not require complex sample preparation and gains precise information about size, shape, density change and size distribution of tracks. It is well suited for studying tracks in amorphous materials, where most conventional techniques fail. Furthermore, SAXS is well suited for *in situ* measurements of ion tracks. Tracks can be annealed during SAXS measurements and the short acquisition times enable studying of the recovery and annealing kinetics of ion tracks.

1.4 Motivation for this study

As outlined above, the study of swift heavy-ion tracks has resulted in many applications including fission track geo- and thermo-chronology [64, 65], radiation damage in nuclear materials [66, 67, 68], particle damage in microelectronics [69], and nanoengineering e.g., creation of nanopore arrays [70, 71, 72]. Fission-track analysis in minerals such as apatite and zircon provides detailed information on the low-temperature thermal histories of rocks and has been applied to a variety of geological problems, including sedimentary provenance, thermal history modeling of sedimentary basins, structural evolution of orogenic belts, and long-term continental denudation. The use of fission track dating as the main method for studying archaeological specimens, such as obsidian artifacts [73] and man-made glasses [74], reconstruction of the low-temperature thermal history of rocks and investigating the thermal history of sedimentary basins for petroleum exploration [75] is of great importance for geological communities as well as the fuel industry. More recently, the importance of thermochronology for energy and climate related issues and interest in earth-surface processes and interactions between tectonics, erosion, and climate has drawn heavily on the use of this technique as it can address the timing and rates of processes operating at low temperatures. Fission track dating is an empirical method that exclusively uses statistical methods applied to etched-track distributions. A fundamental understanding of the underlying un-etched damage and its dependence on geologically relevant parameters has potential to significantly improve the current dating techniques.

In addition to fission tracks, induced tracks of swift heavy ions in different materials have interesting applications in various fields. Swift heavy ion irradiation is very useful for modification of the properties of thin films, foils and surfaces of bulk solids. Ion tracks in various semiconductors and insulator materials are created to facilitate fabrication and provide desired material properties. One of the materials important for electronic devices is quartz. Synthetic quartz possesses unique properties such as wide optical transparency range, wide frequency stability, and good endurance against wear and fatigue, which makes it a suitable material for optical devices. For this reason, ion tracks in quartz have attracted a lot of attention in the last decade. As for fission tracks, a detailed understanding of the ion-track morphology and annealing behavior in quartz can pave the way for their effective utilisation in such applications.

A major emphasis of this thesis is the exploitation of synchrotron-based SAXS for investigating the morphology and annealing behavior of ion tracks [63, 46]. Due to the short acquisition times, time resolved measurements to determine the annealing kinetics and the stability of ion tracks in high temperature environments using *in situ* experiments are possible. We focus on synthetic quartz and two minerals, apatite and olivine as target materials. Using high-energy accelerators, well-controlled parallel ion tracks of identical size and damage morphology are generated and characterisation of the samples and their systematic dependence on temperature is performed.

This thesis has the following structure. Chapter 2 covers the details of ion-track formation and the experimental set up used for the swift heavy ion irradiation. Chapter 3 explains the small-angle X-ray scattering technique, its theory, data modeling as well as the specifications for the SAXS measurements conducted in this project. Results are presenting on the morphology of ion tracks in quartz, apatite and olivine in chapter 4 which includes SAXS measurement of ion tracks as well as comparison of SAXS with TEM results, molecular dynamic simulations and previously reported measurements. The annealing behavior of ion tracks is discussed in chapter 5 and chapter 6 presents the conclusions, final remarks and suggestions for future work.

Chapter 2

Formation of ion tracks

2.1 Ion-solid interaction

When an ion penetrates a solid, two main mechanisms operate to slow down the ion and dissipate the energy. The ion can lose its energy via elastic and inelastic interactions with the target nuclei (nuclear energy loss) and electrons (electronic energy loss), respectively. The elastic interactions can result in the displacement of the target atoms and the formation of collision cascades when recoiled atoms displace additional target atoms. The inelastic interactions produce electronic excitation and ionization of the target atoms. The ion eventually comes to rest at a certain depth inside the solid which is called the projected range or penetration depth. The projected range R is determined by the rate of energy loss along the ion path [76]:

$$R = \int_{E_0}^{0} \frac{1}{dE/dx} dE$$

where E_0 is the incident energy of the projectile ion. In the discussion of ion solid interactions, the average energy loss of the particle per unit path length (dE/dx) is an important factor and is often given in units of keV/nm. The term “energy loss” is used interchangeably with “stopping power” of the material, S(E), and the numerical values and units are identical for both quantities:

$$S(E) = -\frac{dE}{dx}$$

E denotes energy, and x is the path length. The sign of dE/dx is negative as it represents the energy *loss*, although tabulated values are usually given as positive quantities. The ion energy loss depends mainly on the mass and energy of the particle and the composition and density of the target material.

Figure 2.1 shows the relative contributions of the two processes of nuclear and electronic energy loss of Au ions in quartz (crystalline SiO_2). Both energy loss mechanism are energy dependent with nuclear and electronic stopping dominant at low and high incident ion energies, respectively. The electronic energy loss reaches a maximum value whereafter it decreases with increasing energy. This peak which has a magnitude about one order of magnitude higher than that for the nuclear component is called a Bragg peak, named after William Henry Bragg who discovered it in 1903. The total energy loss of an ion in matter can be expressed as:

$$\frac{dE}{dx} = (\frac{dE}{dx})_n + (\frac{dE}{dx})_e \tag{2.1}$$

where the subscripts n and e denote nuclear and electronic energy losses, respectively.

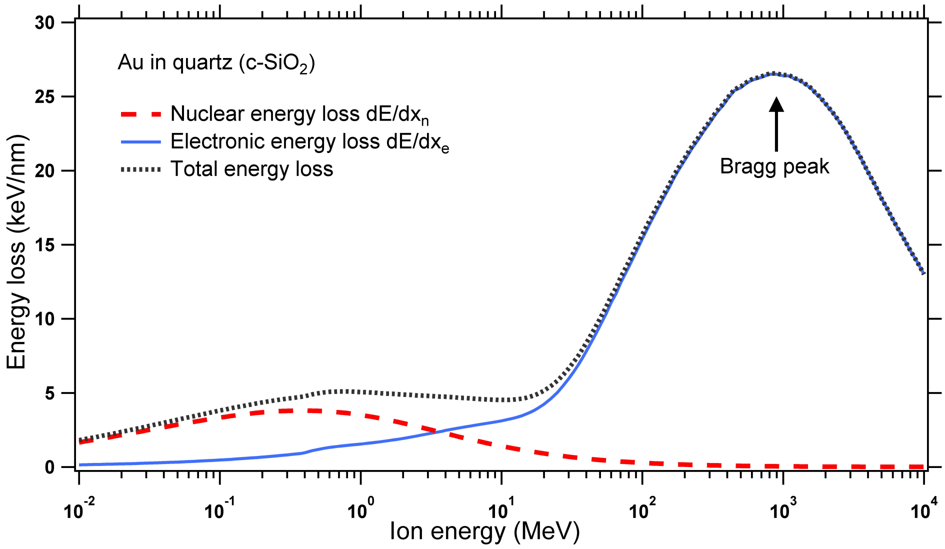

Figure 2.1: Energy loss of Au ions in quartz as a function of ion energy. The peak of the electronic energy loss is called Bragg peak.

The effect of ion penetration in matter can be very different based on the dominant energy loss mechanism. Hence, it is important to understand what happens to ions of different energies when they pass through different materials. For the electronic energy loss, since the number of collisions an ion experiences with electrons is large, and the charge state of the ion traversing in the medium may change, it is very difficult to describe all possible interactions for all possible ion charge states. Instead, the electronic energy loss is given as a simple function of energy which is an average taken over all energy loss processes for different charge states. It can be theoretically determined to an accuracy of a few % in the energy range above several hundred keV from theoretical approaches such as the Bethe-Bloch formula [77]. At ion energies lower than about 100 keV it becomes very difficult to determine the electronic energy loss theoretically. Hence several semi-empirical formulas have been devised including the model given by Ziegler, Biersack and Littmark [78] which is by far the most used. For the nuclear energy loss, if the repulsive potential between two atoms is known, the calculation is possible. Nowadays, the repulsive potential between two atoms can be obtained with great accuracy from ab initio quantum mechanical calculations [79]. In the past few decades computer simulations have been used to calculate the motion of ions in matter and now they are the dominant way of treating energy loss processes. The best known simulation program is SRIM, the stopping and range of ions in matter [80, 79]. In this thesis, SRIM-2008 is used for the calculations of the electronic energy loss and length of the trajectory of different ions in the samples.

2.2 Energy loss mechanisms

Nuclear energy loss

When bombarding a solid with ions in the energy region of keV to low MeV, the penetrating ions mainly undergo elastic collisions with the target atoms. If the target atoms displaced by the projectile ion receive energy above the threshold displacement energy, they will interact with other target atoms and create further displacements. This process which is called a collision cascade can generate vacancies and interstitials inside the material. The threshold for the displacement energy depends on the composition and structure of the matrix. The size and density of the collision cascades vary based on the mass and energy of the penetrating ion. As atoms are bound in solids with energies of approximately 5 eV, it is expected that more energy is needed to displace an atom from a lattice site of a solid [81]. For instance in quartz, the threshold for the displacement energy is around 25 eV [82].

When the mass of the projectile ion and the density of the target material are low, the collisions between the initial recoil and sample atoms happen less frequently and are in the form of a sequence of independent binary collisions between atoms. This process can be simulated using the binary collision approximation approach [83]. An example of this kind of cascade is irradiation with H and He ions with energies below 10 keV. In the collision cascade each generation of recoil atoms has less energy than the previous, and eventually the energy of the knock-on atom goes below the threshold displacement energy for damage production and no more damage will be produced. This process is shown schematically in figure 2.2 where primary, secondary and tertiary knock-on atoms are differentiated by color.

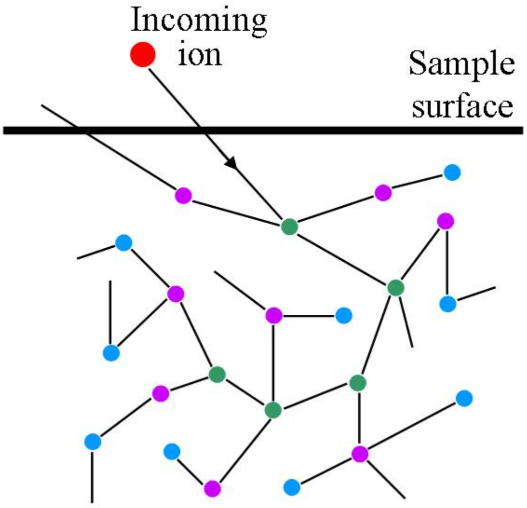

Figure 2.2: Schematic of a collision cascade when the projectile mass and energy, and density of the material are low. Green, purple, and blue circles illustrate primary, secondary, and tertiary recoils, respectively.

When the ion is heavy and energetic enough, and the density of the target material is high, multiple collisions occur simultaneously and the process becomes a complicated process of many-body interactions. In this case which is called a heat spike, the binary collision approximation is not valid and the process can be modeled using molecular dynamic simulations [84]. A heat spike is usually characterized by the formation of a transient underdense region in the center of the cascade, and an overdense region around it [84, 85]. Following the cascade, the overdense region becomes interstitial defects, and the underdense region typically becomes a region of vacancies. In quartz, it is shown that a heat spike does not occur for energies below ~45 keV [86].

Figure 2.3 shows a simulation of 100 keV Au ions implanted into quartz obtained from SRIM-2008 along with the plot of the depth profile of displacements from the sample surface. It is clear from the plot that with this energy, the collision cascade extends to only about 100 nm depths from the sample surface.

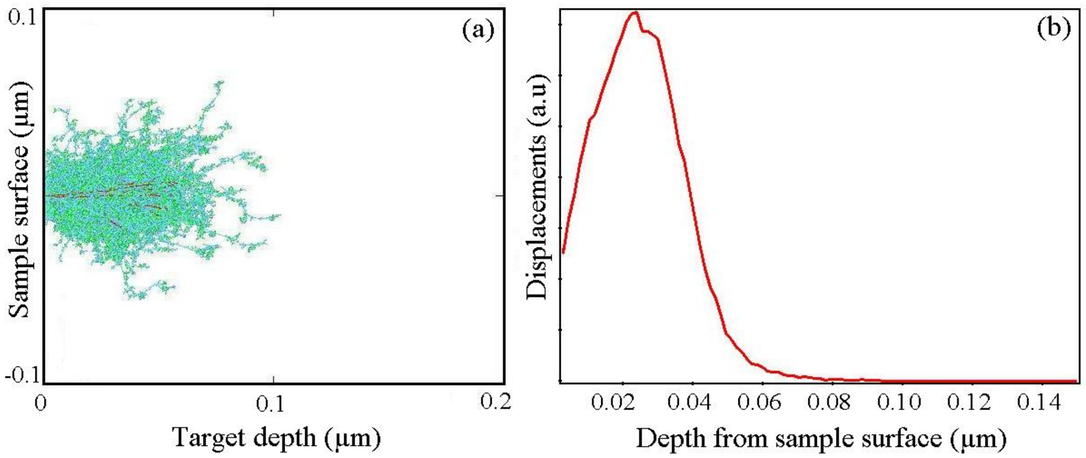

Figure 2.3: SRIM-2008 calculations for irradiation of quartz with 100 keV Au ions. (a) Schematics of ion trajectories with collision cascades. (b) Displacements as a function of depth.

Electronic energy loss

In the regime of swift heavy ion irradiation (SHII) where ions heavier than He are accelerated to energies in the MeV to GeV range, inelastic collisions transfer the energy of the projectile to the target electrons leading to excitation and ionization of the electronic system. As it is shown in figure 2.1, at these high energies the amount of nuclear energy loss is very small and the electronic energy loss (dE/dx_e) dominates. dE/dx_e depends on the charge state and the velocity of the projectile [87, 88] and the maximum dE/dx_e is obtained at the Bragg peak. When the ion passes through a solid, to acquire an equilibrium charge state, it strips off those orbital electrons which are slower than the projectile velocity [89]. Figure 2.4 shows the decrease of dE/dx_e for 1 GeV Pb ions passing through quartz calculated with SRIM-2008 with a dE/dx_e of ~28 keV/nm on the sample surface. The contribution of the dE/dx_n is also plotted which shows the domination of the electronic energy loss until close to the projected range of the ion in the material.

A simulation of the energy deposition of 1 GeV Au ions in quartz and the total number of displacement atoms as a function of penetration depth are calculated with

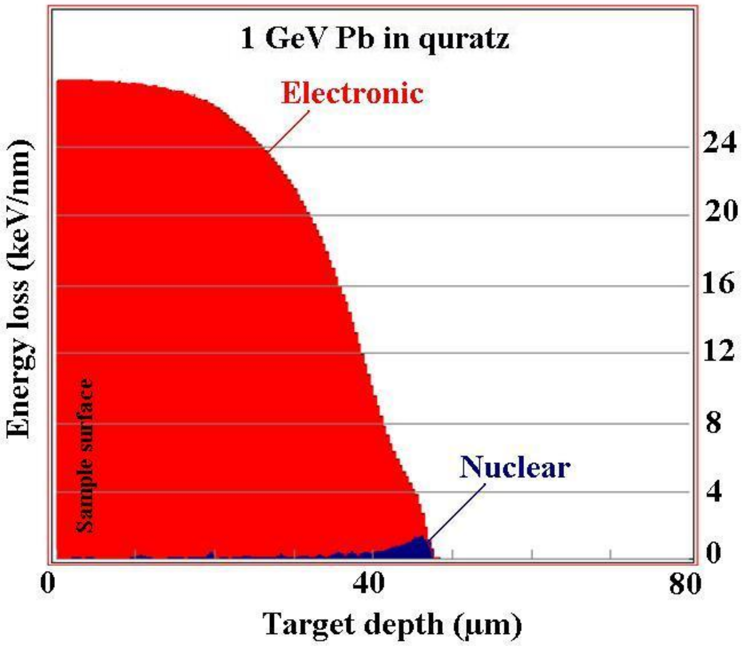

Figure 2.4: Electronic and nuclear energy losses of 1 GeV Pb ions in quartz as a function of target depth calculated with SRIM-2008.

SRIM-2008 and shown in figure 2.5. Due to the absence of nuclear collisions in SHII, the ion trajectory is almost a straight line in the direction of irradiation until the ion energy is reduced to the point where nuclear stopping becomes significant. Comparing with figure 2.3, the thickness of the layer modified by ion bombardment, and the total number and depth of the atomic displacements can be very different based on the ion energy.

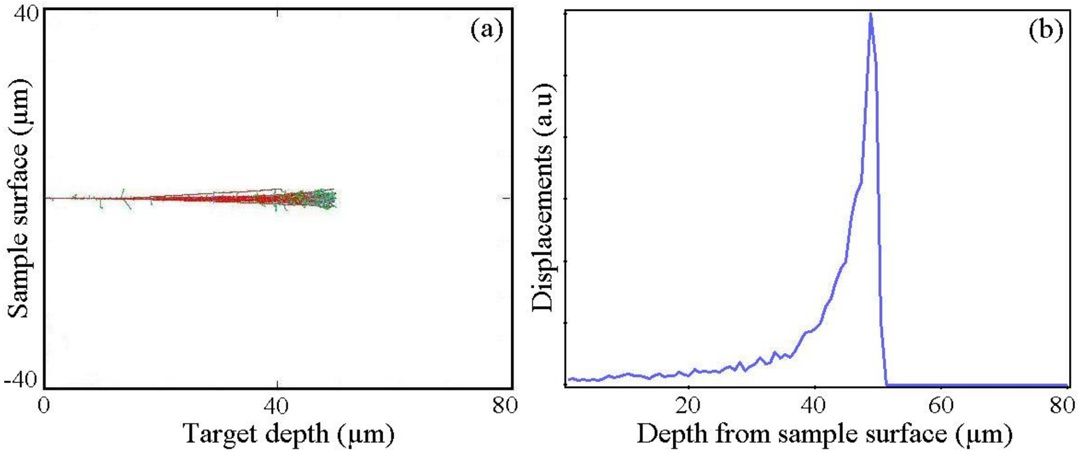

Figure 2.5: (a) Simulation of the trajectories and (b) displacements as a function of depth for irradiation of quartz with 1GeV Au ions calculated with SRIM-2008.

2.3 Ion-track formation

Ion tracks are long narrow regions of defects resulting from the electronic energy loss of swift heavy ions in matter. According to the Bethe formula [90], projectile ions with energies of a few MeV per nucleon deposit about 50% of the energy density into a radius of about 1 nm around their trajectory [91] during a timescale of approximately 10^{-17} to 10^{-13} s. In this highly-ionized region along the ion path the Coulomb repulsion of positively charged target ions may convert a significant amount of the stored energy into atomic motion [91, 6]. This mechanism which is described by the Coulomb explosion model [6, 92, 93] depends on the ionization density and charge neutralization time. Coulomb explosion will be significant only if the charge neutralization time exceeds 10^{-14} for light target atoms and 10^{-13} for heavy atoms [91]. For instance, for most metals charge neutralization times are too fast to allow Coulomb explosion to occur. However, with a rapid charge neutralization, electronic recombination might still be slow and convert the energy from electronic system to atomic system. The different models describing the resulting atomic motion in this case are the lattice relaxation model [94, 95] and the electronic thermal spike model [96, 97, 98]. In the lattice relaxation model, non-equilibrium interatomic potentials lead to a collective atomic rearrangement and therefore a fraction of the energy causes modification of the interatomic forces and subsequent atomic motion [91, 94, 95]. In the electronic thermal spike model it is assumed that electronic excitations form a hot plasma in the narrow region along the ion trajecory and increase the thermal atomic motion via electron phonon coupling [91, 96, 97]. Atomic motion finally may destroy or modify the lattice structure in the narrow region along the ion path. The long column of damage which remains in the material is called an ion track. The evolution of which is shown schematically in figure 2.6 [91].

These ion tracks are typically a few nanometer in diameter and can be up to tens of micrometer long. Tracks have been observed in crystalline and amorphous materials including many insulators [99, 53, 71, 48], various semiconductors [100, 101, 102], and some metals [96, 103, 104].

Track formation requires a material dependent critical electronic energy loss [105, 106]. When the energy of the penetrating ion exceeds the track formation threshold, a continuous track is formed while the energy of the ion decreases. At some point, when the electronic energy loss of the ion approaches the threshold, the track becomes discontinuous and spherical defects are formed [71]. The higher the energy of the projectile, the continuous part of the track would be longer. Ultimately the ion loses all its energy and stops inside the material. Therefore the cylindrical track would end in a conical shaped damage which extends in point defects [107]. The depth of penetration of the ion up to the distance that the electronic energy loss is above the threshold is considered as the track length and is an important parameter. The penetration depth of an ion or the projected range can be calculated by SRIM, however, to estimate the length of a track or calculating the average dE/dx_e, we need to know the track formation threshold. For example, from SRIM-2008 calculations, the projected range of 1 GeV Pb ions in quartz is approximately 47 μm as shown in figure 2.4. Assuming a track formation threshold in quartz of 5 keV/nm, the depth of the ion from the surface to the point that dE/dx_e is greater than 5 keV/nm is about 43.5 μm, which is an estimation for the track length. Therefore, the average dE/dx_e along the track length is equal to the total dE/dx_e divided

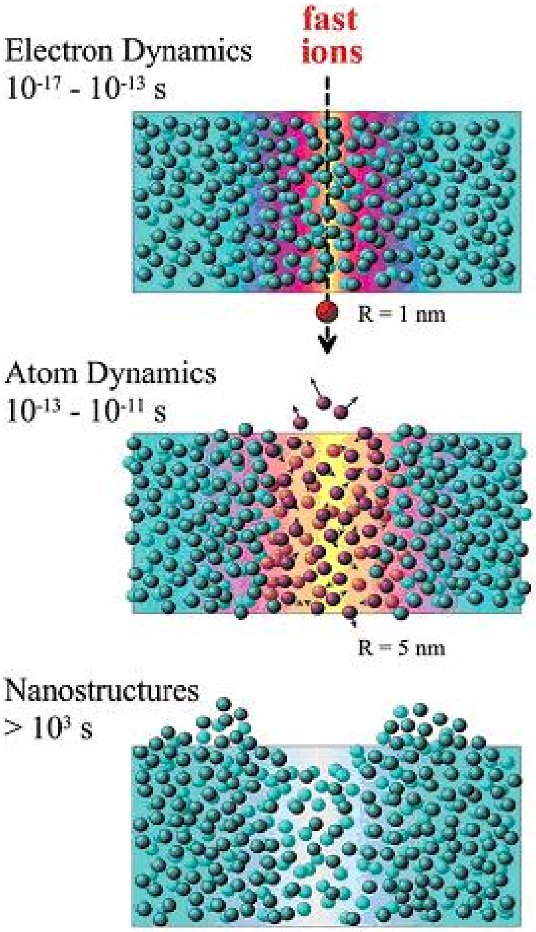

Figure 2.6: Schematic of time evolution of an ion track. The image is taken from reference [91].

by the track length. This is equivalent to the area under the plot of dE/dx_e vs. target depth up to 43.5 μm.

The experimental track formation threshold values depend somewhat on the applied track detection method, because of their different weight to details of the track structure [99]. For instance in quartz, continuous cylindrical tracks have been found for dE/dx_e larger than about 4 keV/nm from channeling Rutherford backscattering [48, 99], 4.6−7.2 keV/nm from chemical track etching [6, 108], and ∼1.8 keV/nm from swelling measurements [109].

In general, insulators are most sensitive to swift heavy ion irradiation and an energy loss of about 1 keV/nm can generate tracks in polymers, some oxide materials and ionic crystals. In semiconductors, track formation thresholds are of the order of 20 keV/nm and tracks can be induced e.g. in amorphous Si and InP. For generating tracks in metals, energy losses of about 50 keV/nm are required and ion tracks can be only generated in some amorphous alloys and few elemental metals.

Velocity effect

From figure 2.1, it can be seen that for a given ion, a certain dE/dx_e value is reached at two different ion energies; on either side of the Bragg peak. Although the energy loss of the ion is the same for both energies there is a significant difference in the energy density which is deposited in the target volume [89]. The deposited energy density depends on the maximum energy transferred to the electrons and changes with the ion velocity. The relative radial distribution of the deposited energy can be estimated using the Monte Carlo simulations [110] and it is shown that high velocity ions smear out their energy into a larger volume leading to a lower energy density along their trajectory [89]. As a result, for the same value of dE/dx_e, the ion with the higher energy often creates a track with a smaller radius than the ion with the lower energy. This is often referred to as the velocity effect.

2.3.1 Inelastic thermal spike model

According to the thermal-spike model, the energy deposited in the electronic system is quickly shared among the neighboring electrons via electron-electron interactions and then transferred to the atoms by electron-phonon coupling. This leads to a high temperature in a narrow region around the ion trajectory that can by far exceed the melting temperature of the material [111]. Generally the track radius is associated with the radius where the material exceeds the melting temperature. The rapid quenching of the temperature following the thermal spike can lead to "freezing in" of the molten or defect structure along the ion trajectory. In crystalline materials, for example the rapid re-solidification of the molten phase can lead to an amorphous track structure [71].

It is possible to theoretically evaluate the lattice temperature increment in thermal spikes by taking into account the electron-phonon coupling strength and electronic diffusivity. In the inelastic thermal spike model the electron and the lattice subsystem are considered as two coupled systems. This can be theoretically explained in the simplest form by writing the thermal-diffusion differential equations derived in two regimes of stationary and dynamic thermal diffusion.

Stationary thermal diffusion

When two thermal reservoirs at temperatures of T and T' are connected via a heat conductor of cross section σ, thermal conductivity K and length L, the stationary heat transfer rate, I, can be expressed as:

$$I = -K\frac{T - T'}{L}\sigma \tag{2.2}$$

In a three dimensional isotropic medium the three heat currents in x, y, and z direction through the volume element depend on the corresponding gradients (dT/dx), (dT/dy), and (dT/dz) and are independent of each other. Therefore the current density is given by

$$j = -K\nabla T \tag{2.3}$$

that is proportional but antiparallel to the thermal gradient ∇T. This stationary thermal diffusion equation is suited for time-independent problems.

Dynamic thermal diffusion

The thermal energy change dQ within the one dimensional element dx corresponds to the net flow of heat arriving in the element during the time dt and is given by:

$$dQ = C_v dx dT = (j(x) - j(x + dx))dt \tag{2.4}$$

where C_v is the specific heat of the volume element. The sum of the heat energies entering the volume element per unit time from left (x) and right $(x+dx)$, is given by the current densities at x and at $x + dx$, multiplied by the time interval dt. Therefore, we can rearrange the above equation to arrive at:

$$C_v dT = -\frac{dj(x)}{dx} dt \tag{2.5}$$

In a three-dimensional isotropic medium, the three thermal currents can therefore be linearly superposed and we can arrive at the thermal spike model typically described by two coupled differential heat equations in cylindrical geometry $(\frac{d}{dx} \rightarrow \frac{1}{r}\frac{\partial}{\partial r})$ [112, 113, 96, 114] as:

$$\begin{aligned} C_e(T_e)\frac{\partial T_e}{\partial t} &= \frac{1}{r}\frac{\partial}{\partial r}[rK_e(T_e)\frac{\partial T_e}{\partial r}] - g(T_e - T_a) + A(r,t), \\ C_a(T_a)\frac{\partial T_a}{\partial t} &= \frac{1}{r}\frac{\partial}{\partial r}[rK_a(T_a)\frac{\partial T_a}{\partial r}] + g(T_e - T_a) \end{aligned} \tag{2.6}$$

where T, C, and K are the temperatures, the specific heat coefficients (same as C_v in equation 2.5) and the thermal conductivities of the electronic (e) and lattice subsystem (a), respectively; t is the time and r is the radial distance from the ion trajectory. The coupling term $g(T_e - T_a)$ accounts for the energy exchange due to electron-phonon interaction where g is the electron-phonon coupling constant. Below we explain various physical parameters of the heat equations in more detail.

The energy density deposited into the electronic subsystem at a time t and a radial distance r from the center of the ion trajectory [110] is represented by $A(r,t)$ and is determined by integrating the deposited thermal energy that is an exponential decaying function of time. Most of the ion energy is transferred to the electrons near the ion trajectory within time of 10^{-15} s.

The electronic specific heat of a metal for low electronic temperature is given by [115]:

$$C_e = \frac{\pi^2 k_B^2 n_e}{2E_F} T_e, \tag{2.7}$$

where the Fermi energy is given by $E_F = \frac{\hbar^2}{2m_e}(3\pi^2 n_e)^{2/3}$ [115], m_e is the electron mass, n_e is the electron number density, and k_B and $\hbar$ are Boltzmann and Planck constants, respectively. For temperatures above the Fermi temperature, $T_F = E_F/k_B$, the specific heat becomes constant $C_e = 3/2k_B n_e$.

The electronic thermal conductivity $K_e(T_e)$ [116] can be evaluated from experimental scaling of the thermal diffusivity with respect to Au, a noble metal in which the electrons behave like a quasi-free electron gas [117].

The electron-phonon coupling g is the key parameter that defines the rate of the electron energy transport to the lattice [118]. If the lattice temperature is not much smaller than the Debye temperature T_D [119], the g factor may be analytically found.

In insulators the values of the thermal parameters such as C_e and K_e are problematic since there exist no free electrons. However, it has been shown that hot electrons in the conduction band of an insulator behave like hot free electrons in a metal [120]. The electron-phonon coupling constant g of insulators can be linked to the electron-phonon mean free path λ through $\lambda^2 = C_e D_e / g$, where D_e is the electron diffusivity. When the heat equations are solved numerically, λ is the only free parameter which can be deduced from fits to experimental track radii. A suitable λ value has to describe track data in a wide range of electronic energy losses and beam velocities.

Various other thermal spike models have been developed to describe ion-irradiation effects in grain growth [121] and surface structure of highly-oriented pyrolytic graphite [122].

2.3.2 Coulomb explosion model

In the Coulomb explosion model, ion tracks result from a repulsion of the positively charged target atoms close to the ion trajectory [123]. The energy of the ion which is transferred to the target electrons causes electron cascades which result in a trail of highly-ionized atoms. The positively charged target atoms attract the free electrons and if the time for charge neutralization is more than 10^{-14} s, atomic motion can set in as a result of the repulsion of the positive target atoms which can lead to the formation of defect structures [124]. In this model the coulomb repulsive forces in the ionized zone are required to exceed the lattice bonding forces in order for a track to be formed. For a continuous damage track to occur, there needs to be at least one ionization per atom plane crossed by the incident ion.

The Coulomb explosion model is still lacking clear experimental evidence and for solids with a high electron mobility, it is likely that the charge neutralization times are sufficient to inhibit this track formation process [124]. Even in insulating materials it is possible for the electrons from outside of the highly-ionized trajectory to neutralize the charge in a time shorter than 10^{-14} s.

2.4 Ion track simulation

Ion tracks can be modeled using molecular dynamic (MD) simulations [125] which uses semi-empirical models of classical dynamics to represent forces between atoms and allows them to move under such forces. Assuming that the models for the inter-atomic forces represent the true forces between atoms, the behavior of a system of atoms can be modeled with a reasonable accuracy.

In MD simulation, the electronic energy loss of the track producing ions can be implemented by continuously following the evolution of the atomic lattice temperature calculated with the inelastic thermal spike model [126]. That means the energy distribution provided by the thermal spike model serves as an input for MD calculations. Figure 2.7 shows the top-view of a computational image of an ion track in quartz for irradiation of 185 MeV Au ions [125].

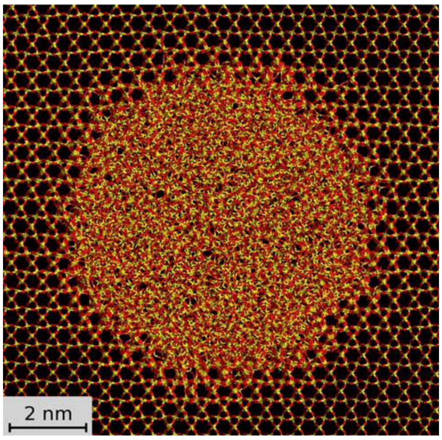

Figure 2.7: Top-view atomistic image of MD simulated track in crystalline SiO_2 generated with 185 MeV Au ions [125].

MD simulations can obtain real time evolution of different systems and study thermodynamic properties including temperature profiles that can be used in rate equations as well as mechanical properties such as elastic behavior. However, MD can simulate only small samples (L<1 μm, up to $\sim 10^9$ atoms) during a very short time intervals (t<1 μs) and it is computationally expensive [127]. Despite its limitations MD is a very powerful tool to study nanosystems.

2.5 Ion irradiation of samples

The ion tracks studied in this thesis were generated by swift heavy ion irradiation of the samples at the Australian National University (ANU) and by our collaborators at the GSI Helmholtz Center for Heavy Ion Research in Germany. One sample was irradiated at the Grand Accelerateur National d'Ions Lourds (GANIL) in France.

Figure 2.8 shows a schematic diagram of the ANU Heavy Ion Accelerator Facility, the 14UD Tandem Van de Graaff accelerator at the Department of Nuclear Physics. Negative ions produced from a Multi Cathode Source of Negative Ions by Caesium Sputtering (MC-SNICS) [128, 129] are pre-accelerated to an energy of 150 keV to match the entrance optics of the accelerator. The 90° injection magnet is tuned to select the ions based on their mass. The negative ions are then accelerated from ground potential towards the positively charged high voltage terminal in the center of the machine where they gain an energy of:

$$E = eU \tag{2.8}$$

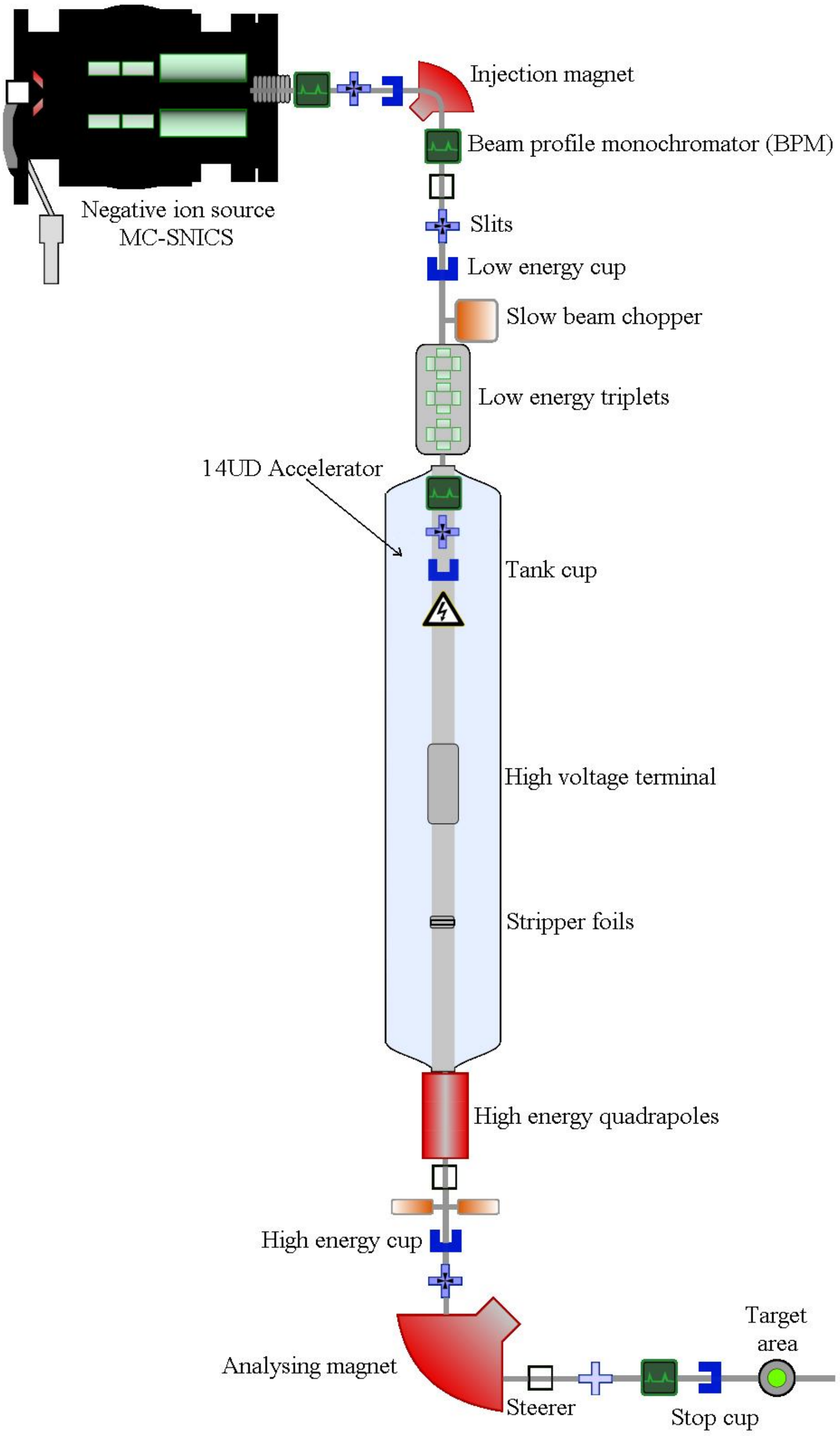

Figure 2.8: Schematic diagram of the 14UD ANU accelerator.

where U is the terminal potential in MV and e is the charge of the ion. The energetic ions go through a carbon foil where electrons are stripped off and result in a distribution of positively charged states of the ions [130]. The most intense charge state can be evaluated from the semi-empirical formula [130]:

$$q = Z(1 + [3.85.Z^{-0.45}.\sqrt{E/A}]^{-1.67})^{-0.6} \tag{2.9}$$

where E is in MeV and A is the atomic mass number of the ion. The now positively charged ions go through a second phase of acceleration at the bottom of the accelerator which is at ground potential. The final energy after the second acceleration phase for the ions with charge state q and terminal potential U is:

$$E_{Beam} = (1 + q)eU \tag{2.10}$$

When the beam leaves the accelerator, a specific charge state is selected for a desired energy from the charge state distribution using the 90° analysing magnet. The selected beam is then directed to the experimental set-up. The maximum terminal potential of 14 MV allows acceleration of the ions to energies of up to about 200 MeV (using for example a charge state $q = +13$).

To ensure homogeneously irradiated samples, the beam is scanned across the target in both X and Y directions irradiating an area of approximately $3{\times}6mm^2$ using magnetic deflections. At the ANU accelerator irradiation fluences of up to about 1×10^{15} ions/cm^2 are realistically achievable. However in this thesis, the applied fluences varied between 5×10^{10} and 4×10^{11} ions/cm^2 to avoid significant overlap of the ion tracks. Calculations of the track overlap are given in section 4.1.3.

All samples for this study were irradiated at normal incidence and ambient temperature. At the ANU 14UD accelerator, ^{197}Au ions were used at the energies of 27, 89, and 185 MeV and ^{127}I ions were used at the energies of 100 MeV. For irradiations at higher energies we used ^{207}Pb ions of 1 GeV at the GANIL accelerator and variety of ions (including ^{197}Au and ^{238}U) at the UNILAC accelerator at GSI. The UNILAC accelerator usually accelerates the ions to an energy of 11.1 MeV/u (energies ranging from hundreds of MeV to a few GeV). In order to reduce the energy of the ions, degrader foils of aluminum with thicknesses between 16 and 64 μm were placed in front of some of the samples.

A schematic of a sample with ion tracks generated normal to the surface using an ion accelerator is shown in figure 2.9. By keeping the energy constant during ion irradiation and controlling the incident angle, homogeneity and fluence, it is a valid assumption that the resulted tracks are well separated, identical, and parallel inside the samples. In section 3.4.6 we discuss how to account for the deviations from perfectly parallel and identical tracks for data modeling.

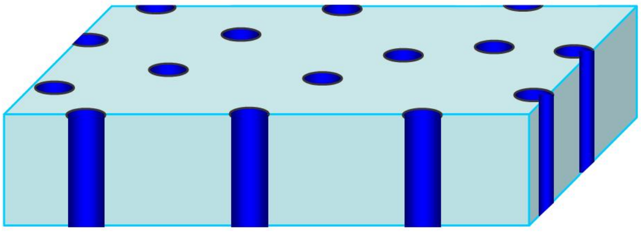

Figure 2.9: Schematic of a sample containing well controlled ion tracks. The schematic is not a full representative of real ion tracks as it does not show the deviation of tracks from a perfect cylinder.

Chapter 3

Small-angle X-ray scattering

This chapter introduces the principles of small-angle X-ray scattering (SAXS) as well as the theoretical models and experimental protocols used to study ion tracks in various materials.

3.1 Interaction of X-rays with matter

Electromagnetic radiation comes in discrete packets of photons. The energy of a photon is inversely proportional to the wavelength λ, $E = hc/\lambda$, where h is the Planck constant and c is the speed of light. X-rays are photons/electromagnetic waves with wavelengths in the range of 0.01 to 10 nm and energies between 100 eV and 100 keV located between ultraviolet and gamma rays in the electromagnetic spectrum shown in figure 3.1.

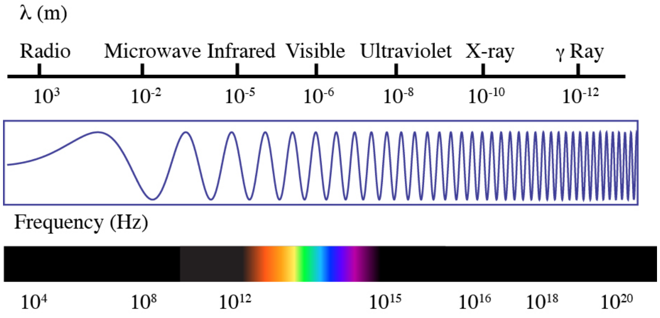

Figure 3.1: The electromagnetic spectrum showing the range of wavelengths, frequencies, and notation of electromagnetic radiation.

With their small wavelength and high-energy, X-rays provide an indispensable tool for studying the structure and electronic properties of matter. X-rays interact with matter mainly in two ways: absorption and scattering [131, 132]. When X-rays of a particular wavelength penetrate a material, depending on the thickness and properties of the sample such as its density, a fraction of the beam passes through undisturbed, a fraction will be absorbed and transformed into other forms of energy (heat, fluorescence, etc) and a fraction will be scattered.

3.2 X-ray sources

The ongoing development of X-ray sources paves the way to probe materials with increasing resolution and shorter acquisition times. This section gives an overview of different X-ray sources and explains the need for synchrotron radiation.

X-rays are used to study the detailed structures of matter on a scale sensitive to the placement of individual atoms. Different techniques based on X-rays are widely applied to provide valuable data including information on the chemical composition and electronic properties, on micro and nano structures, and on the properties of surfaces, interfaces and bulk materials. In addition to physics and materials science, X-ray radiation is currently contributing to a variety of disciplines such as medicine and health care, biological and life sciences, chemistry, environment, earth sciences, energy generation and many more.

3.2.1 Conventional X-ray sources

In 1895, Wilhelm Conrad Roentgen discovered X-rays by using a device called an X-ray tube. In an X-ray tube, electrons are generated at a cathode and then accelerated towards an anode. Collision of electrons with the anode results in generation of X-rays radiating in all directions from the collision spot. A schematic of an X-ray tube is shown in figure 3.2. The electrons are either generated in a gas tube from a "cold cathode" by ion bombardment or by thermionic emission from a "hot cathode" in a vacuum tube. High electronic fields are used to accelerate the electrons towards the anode which is typically made of Copper or Tungsten. If the electrons have sufficient energy, they can knock electrons out of an inner shell of the target metal atoms. Subsequently electrons from higher states drop down to fill the vacancies, emitting X-ray photons with the precise energies determined by the electron energy levels, known as characteristic radiation. Furthermore, electrons are decelerated in the anode material by deflection from the electrons or nuclei, leading to the emittance of a broad spectrum of X-rays called Bremsstrahlung radiation. Figure 3.3 shows a schematic of the relative intensity of Bremsstrahlung and characteristic radiation as a function of the X-ray energy. Characteristic radiation which has sharp peaks at specific energies unlike a continuous spectrum of Bremsstrahlung radiation, provides much higher intensity.

To produce X-rays in these ways, relatively large amounts of electrical energy must be transferred to the X-ray tube. Only a small fraction of the energy deposited in the X-ray tube is converted into X-rays, most appears in the form of heat. This places a limitation on the use of X-ray apparatus. Moreover, in early versions of an X-ray tube, light was emitted in all directions, with no possibility of focusing it or making the rays parallel. This light was also only intense at particular wavelengths, which restricted its use, particularly in the field of spectroscopy. However, high-vacuum tubes provide stable and reproducible operation with relatively high voltages. The intensity from an X-ray tube is sufficient for many applications including medical applications and analytical laboratory based techniques, such as X-ray diffraction techniques.

In addition to X-ray tubes, in-house or laboratory sources can also produce X-rays using a rotating anode. In a rotating anode, the anode rotates at high speed to distribute and dissipate heat more efficiently. Therefore it can generate X-rays with higher intensity

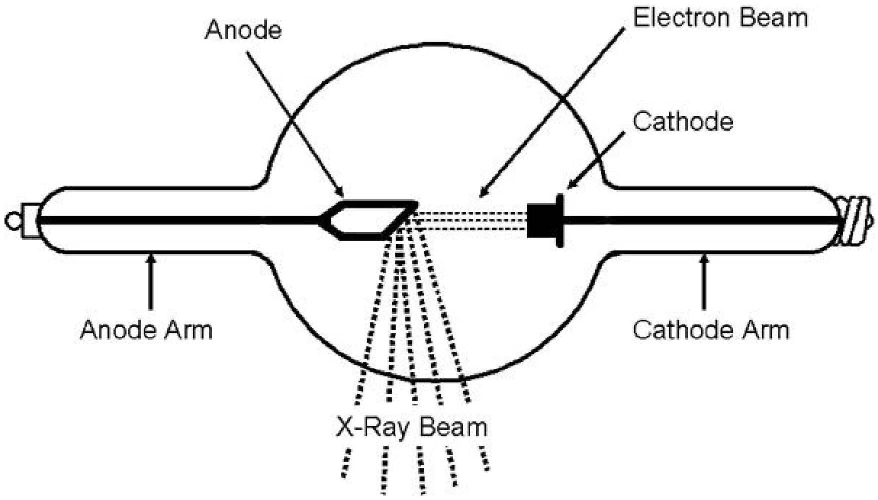

Figure 3.2: Schematic of an X-ray tube.

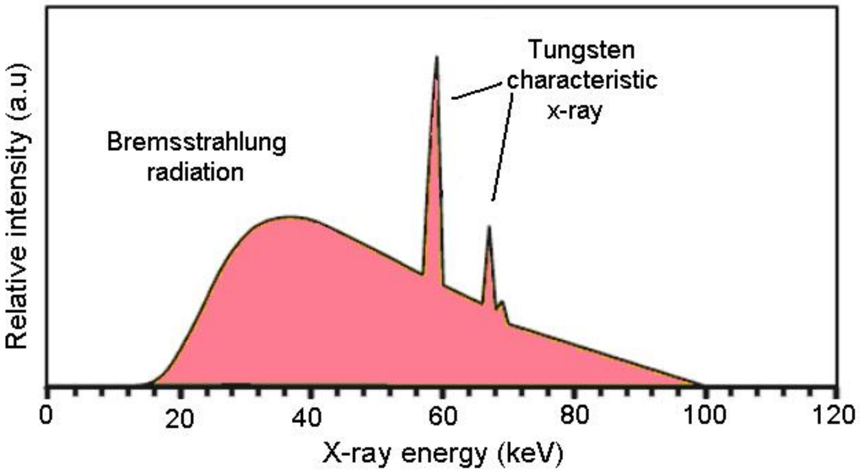

Figure 3.3: Relative intensity of the Bremsstrahlung and characteristic radiation as a function of X-ray energy.

than conventional X-ray tubes. Common target materials for the anode include Cu, Co, Ag and Al.

3.2.2 Synchrotron radiation

A different approach to the X-ray tube mechanism, is to deflect (accelerate) electrons by passing them through a magnetic field. A synchrotron is a type of particle accelerator that produces beams of electrons traveling close to the speed of light which are stored in a circular storage ring, where they undergo frequent magnetic deflections, thus producing high intensity X-rays [133].

The first generation of light sources emerged in the late 1960s by the development of electron storage rings, the basis for all of today's synchrotron sources. In a storage ring, the electron beam circulates at a fixed energy for periods up to many hours and undergoes a repeated sequence of injection and acceleration. Storage rings provide high beam currents and fluxes of radiation and great beam stability. The first generation of synchrotrons were not built specially to generate synchrotron radiation, but were intended for research in particle physics.

As the high-energy physics frontier advanced, first generation light sources gradually evolved toward second generation facilities by improving the spectral brightness or brilliance (the flux per unit area of the radiation source per unit solid angle of the radiation cone per unit spectral bandwidth) while still using bending magnets as the main source of synchrotron light. Second generation facilities were purpose-built machines specifically for synchrotron radiation but were not designed for low emittance (a measure of the size of the electron beam in position and momentum phase space) or with many straight sections for insertion devices.

The use of wigglers and undulators as insertion devices in the straight sections of the storage ring (explained in detail later), marks the third generation of synchrotrons. They provide much higher intensities and brightness for examining extremely small or dilute samples or investigating the structure and properties of objects with very fine spatial resolution. The experiments can be carried out much more quickly, enabling a high through-put of samples or the ability to follow chemical and biological reactions in real-time. An example of an advanced third generation synchrotron is the Australian Synchrotron.

Development of the next generation of synchrotron radiation is already under way in the form of free electron lasers based on a very long undulator in a high-energy linear accelerator which aims at having a peak brightness many orders of magnitude beyond that of the third generation sources, as well as pulse lengths of 100 fs or shorter.

In X-ray radiation, the figure of merit for many applications is brilliance which is a term that describes both the brightness and the angular spread of the beam. The most important advantage of synchrotron radiation over a laboratory X-ray source is its brilliance. For example, a synchrotron source like the Australian Synchrotron has a brilliance that is more than a billion times higher than a laboratory source. Figure 3.4 shows average brightness (proportional to brilliance) of different synchrotron radiation sources and free-electron lasers as a function of photon energy.

Basic principles

In a synchrotron, electrons are typically accelerated to high speeds (close to the speed of light) in several stages for example a linear accelerator and booster ring to achieve a final energy that is in the GeV range [133]. The electrons travel at these relativistic speeds through strong magnetic fields created by a series of magnets. For a particle of rest mass m, relativistic charge e, and the Lorentz factor of $\gamma = 1/\sqrt{1 - v^2/c^2}$, which moves with a velocity of v in a uniform magnetic field of strength B, the equation of motion can be written as:

$$\gamma m \frac{d\vec{v}}{dt} = e(\vec{v} \times \vec{B}) \tag{3.1}$$

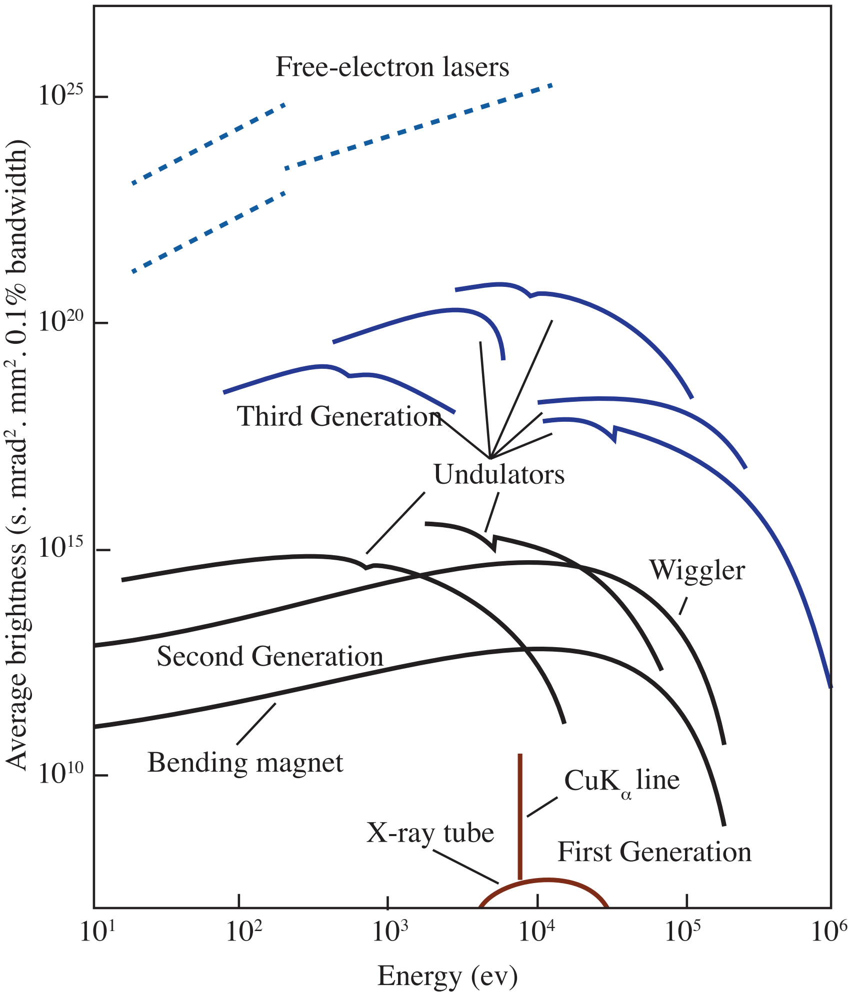

Figure 3.4: Average brightness of synchrotron radiation sources and free electron lasers as a function of photon energy.

As the force on the electron is perpendicular to the motion, the electric field does no work on the particle, and therefore there is no acceleration parallel to the magnetic field. The solution to the equation 3.1 is helical motion: a constant velocity parallel to the magnetic field (B), and uniform circular motion in a plane perpendicular to B. The trajectory of the particle makes an angle of θ (pitch angle) with the direction of the magnetic field. The particle's trajectory forms a spiral centered on the field line. This spiral has a radius of curvature of $a = v/(\omega_r \sin\theta)$, where $\omega_r = eB/m$. This narrow cone of radiation is extremely intense and extends over a broad continues energy spectrum with a critical energy of:

$$E_c = \frac{3e\hbar B\gamma^2}{2m} \tag{3.2}$$

beyond which the intensity of the beam decreases exponentially. The maximum photon energy achievable with a storage ring is few times its critical energy. In practical units the critical photon energy can be simplified to:

$$E_c = 0.665 E_e^2 B. \tag{3.3}$$

where E_e is the energy of the electron in the storage ring. E_c is in the order of keV, E_e is in GeV range and the magnetic field B is in Tesla.

An important property of a particle accelerator is transverse emittance, E_m:

$$E_m = \frac{6\pi(\sigma_b^2 - D^2(\frac{dp}{p}))}{\beta} \tag{3.4}$$

where σ_b is the width of the particle beam, dp/p is the momentum spread of the particle beam, D is the value of the dispersion function and β is the value of the beta function at the measurement point in the particle accelerator. The β and dispersion functions are defined in references [134, 135] as functions of magnetic dipole radius and length. In general, the emittance scales proportional to the square of the energy, proportional to the cube of the bending angle, proportional to the cube of the quadrupole focal length and inversely proportional to the cube of the dipole length.

To reach high luminosity or high brilliance accelerators need a low emittance. However, preserving a low emittance from the source to the end can be very challenging. Correcting emittance distortion is sometimes required to achieve better performances. Table 3.1 compares energy, circumference, current, emittance, and lifetime at maximum current of some synchrotrons in the UK, Canada, Australia and Japan.

Parameter	Australian Synchrotron	Diamond (Chilton, UK)	Canadian Light Source	Spring-8 (Japan)
Energy	3.0 GeV	3.0 GeV	2.9 GeV	8.0 GeV
Circumference	216.0 m	561.6 m	170.0 m	396.1 m
Current	200 mA	300 mA	200 mA	10 mA
Emittance	7.0 nmrad	2.7 nmrad	18.1 nmrad	230.0 nmrad
Lifetime at max. current	20 h	10-20 h	N/A	N/A

Table 3.1: Comparison of the Australian Synchrotron with other synchrotrons in the UK, Canada, and Japan.

Synchrotron radiation devices

Synchrotron radiation was initially generated using bending magnets. Bending magnets are one of the sources of synchrotron light, where a narrow searchlight-like cone of radiation with an angle of $\theta = 1/\gamma$, where $\gamma = (1 - v^2/c^2)^{-1/2}$, is emitted as the relativistic electrons pass the bend. The bending magnet covers a broad spectral range and is a low cost and accessible way to generate synchrotron radiation.

Modern synchrotron light sources use periodic magnetic structures called insertion devices that stimulate highly-brilliant, forward-directed synchrotron radiation emission by forcing a stored charged particle beam to perform wiggles, or undulations, as they pass through the device.

A wiggler is a special magnet with alternating directions of the magnetic field that steers the electron beam through a device in a trajectory resemblinge a sine wave. The photon flux and intensity of the radiation emitted by one magnet of a wiggler is the same as from a bending magnet. The total intensity is thus a factor of N_p higher, where N_p is the number of poles within the wiggler. The radiation cone angle in this case is $\gg 1/\gamma$. Figure 3.5 (b) shows schematic of a wiggler and a plot of its flux.

A wiggler magnet can be engineered such that the radiation from different periods interfere coherently, thus producing sharp interference peaks instead of a broad spectrum. This type of device is called an undulator that uses less powerful magnets to produce gentler undulations of the beam. The light cones from an undulator overlap and interfere with each other, so that certain wavelengths of light are enhanced. These wavelengths can be changed by altering the gap between the component magnets so that the light is tunable to specific wavelengths. The flux of the undulator radiation is proportional to the number of periods.

The types of radiation from a bending magnet, a wiggler and an undulator are shown schematically in figure 3.5 with the plots of the photon flux as a function of photon energy. Figure 3.6 shows schematics of a bending magnet and the two insertion devices.

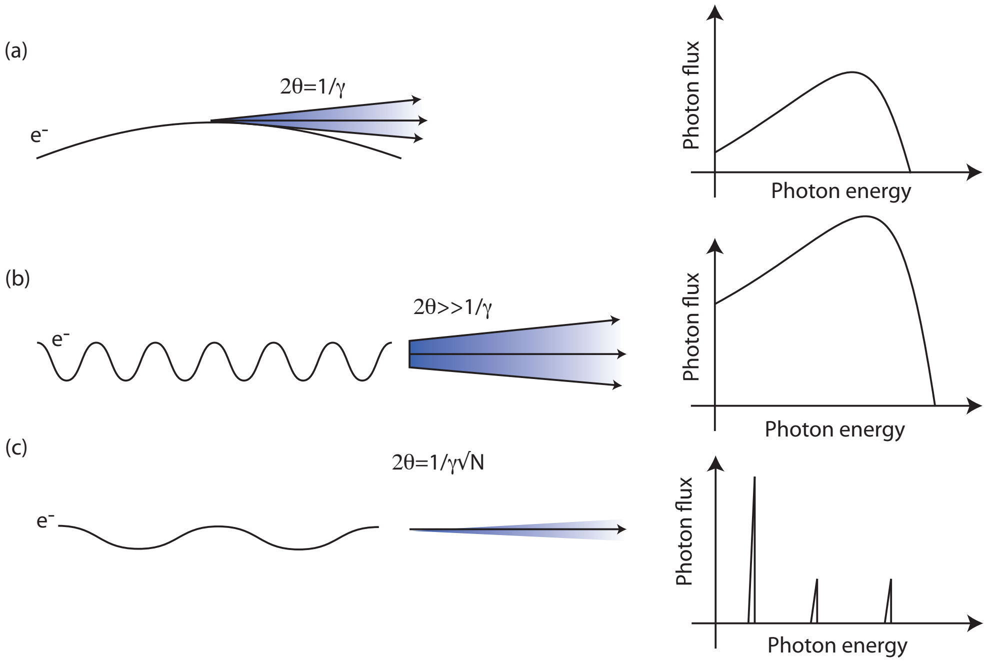

Figure 3.5: Three forms of synchrotron radiation, (a) bending magnet radiation, (b) wiggler radiation, (c) undulator radiation. Plots on the right show schematics of the photon flux as a function of photon energy for each type of radiation.

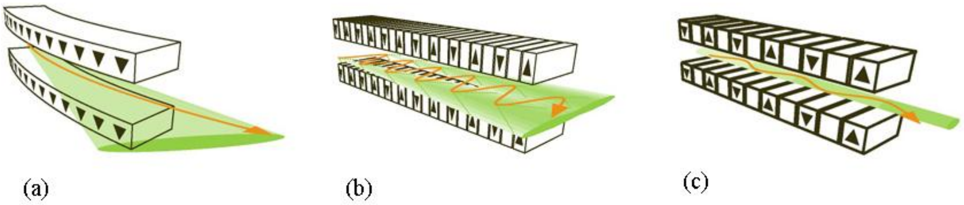

Figure 3.6: Illustrations of (a) bending magnet, (b) wiggler and (c) undulator. (Image courtesy: Australian Synchrotron)

3.2.3 Australian Synchrotron

The SAXS experiments in this thesis were performed at the Australian Synchrotron (AS) in Melbourne which started its operation in 2007. Currently the AS has nine operational beamlines: imaging and medical beamline, infrared micro spectroscopy, far-infrared and high-resolution FTIR, macromolecular crystallography (protein crystallography), powder diffraction, small and wide angle X-ray scattering, soft X-ray spectroscopy, X-ray absorption spectroscopy, and X-ray fluorescence microprobe (X-ray micro spectroscopy). Figure 3.7 shows a view of the AS.

Figure 3.7: Aerial view of the Australian synchrotron.

Figure 3.8 shows a schematic of the Australian Synchrotron. The electrons used to provide the synchrotron light are initially accelerated to an energy of 90 keV before being injected into the linear accelerator (linac). The linac operates at a frequency of 3 GHz and accelerates the electron beam to an energy of 100 MeV, over a distance of around 15 meters. The electron beam then enters the booster ring with a circumference of 130 meters where their energy is increased to 3 GeV. The storage ring is maintained under ultra high vacuum and consists of series of magnets separated by straight sections. The radio frequency (RF) system is responsible for constantly supplying energy to the electrons as they move around the storage ring. This is necessary since the generated radiation constantly loose the electrons energy. The final destination for the accelerated electrons is the storage ring. It is 216 meters in circumference and consists of bending magnets, insertion devices and maintains a steady current of ~200 mA in top up mode.

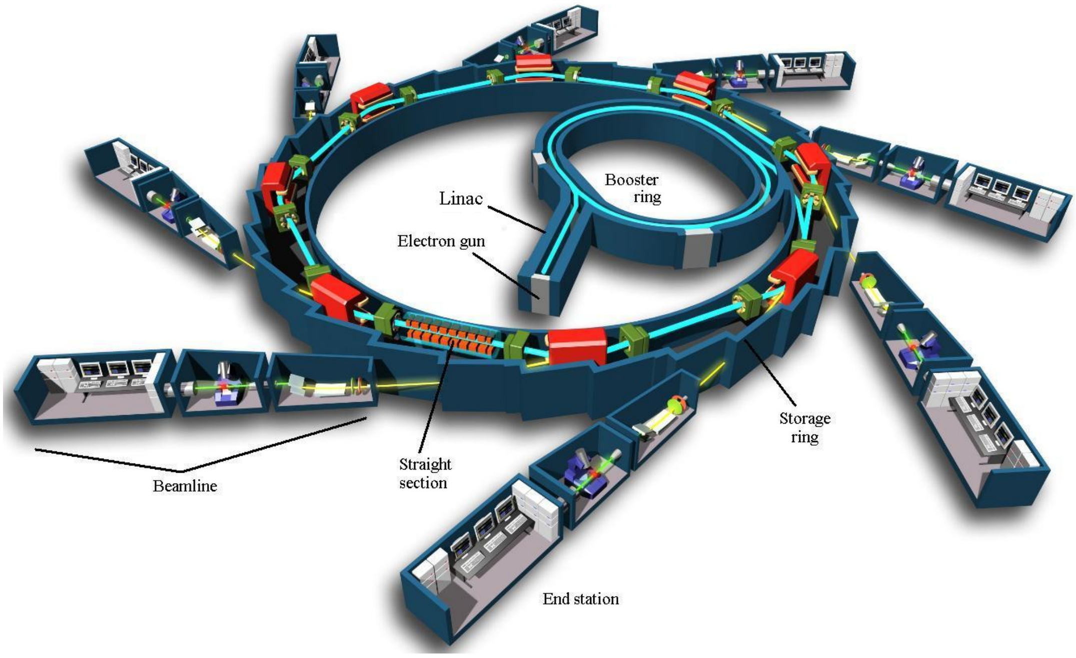

Figure 3.8: Schematic of a typical synchrotron (Image courtesy: Australian Synchrotron).

3.3 X-ray scattering

At high energies, scattering can dominate photoelectric absorption. The scattering of X-ray photons by matter proceeds predominantly through Compton scattering, Thomson scattering and Rayleigh scattering [132]. The strength of these interactions depends on the energy of the X-rays and the elemental composition of the material. Various interactions of an X-ray beam with matter are summarised in figure 3.9.

X-ray scattering can occur with or without energy loss and the scattered beam can thus have a different wavelength than the incident radiation (Compton scattering) [136] or it can have the same wavelength (Rayleigh scattering, Thompson scattering) [137].

Compton scattering is an inelastic interaction where a photon interacts with the outer shell electron of an atom and loses a fraction of its energy E_0 to the electron. The energy partially transferred to the electron ionises the atom. The remainder of the energy, E_s, is transferred to a scattered X-ray photon that has a longer wavelength compared to the incident photon. The scattered beam has a different wavelength and has no particular phase relation to the incident photon. It propagates along the incident direction with a higher probability than all other directions. Therefore Compton scattering can not generate interference and does not carry structural information. It can be considered

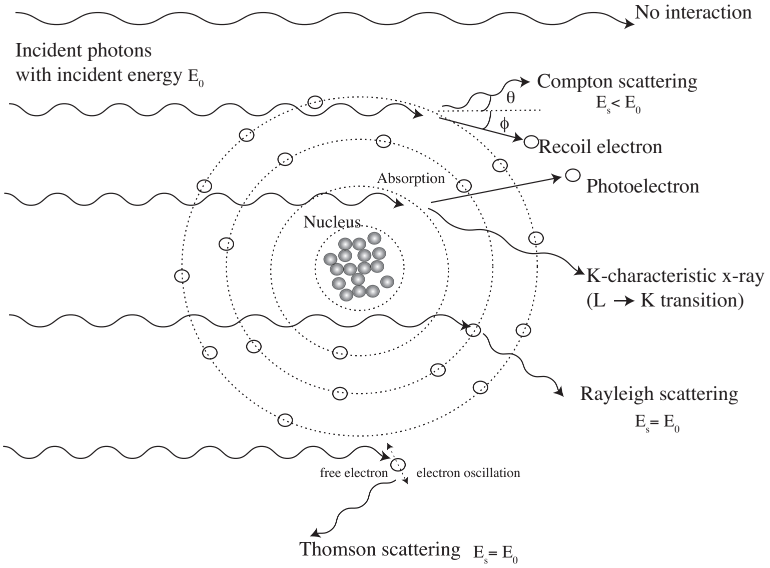

Figure 3.9: Illustrative summary of interaction of X-ray beam with matter.

as featureless background radiation. When the incident energy of the photon becomes comparable to the rest mass of the electron, quantum mechanics predict that the Compton scattering is the dominant form of scattering.

The elastic scattering of X-rays is known as Rayleigh scattering and Thompson scattering [138]. Rayleigh scattering is a type of elastic scattering that happens as a result of the collision of photons with strongly bound electrons. The incident beam interacts with an electron and is scattered (deflected) with no energy loss. It temporarily raises the energy of the electron without expelling it from the atom. The electron starts dipole oscillation with the same frequency as the incoming beam. Due to this oscillation, the electron emits an X-ray photon of equal energy but at a different direction. Thomson scattering is the elastic scattering of light field by a free non-relativistic charged particle. The electric component of the incident light field accelerates the particle. The particle then undergoes dipole radiation when it decelerates that results in scattering of light with same frequency as incident light.

As schematically shown in figure 3.10, when the angle θ of two scattered beams leads to a pathlength difference $\Delta x = n\lambda$, the scattered rays undergo constructive interference leading to peaks in the scattered intensity. The pathlength difference Δx can be explained by the angle θ between the incoming and scattered beam by $2d \sin\theta$. This leads to Bragg's law, which describes the condition for constructive interference from periodic arrangements of crystallographic planes of the crystalline lattice:

$$2d \sin\theta = n\lambda, \tag{3.5}$$

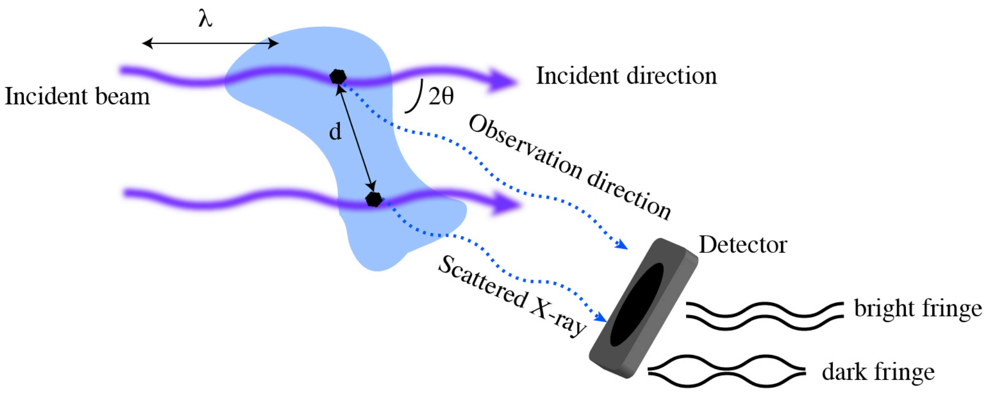

Figure 3.10: Interaction of X-rays with structure and interference of the emitted waves on the detector.

3.4 Small-angle X-ray scattering

Wave-diffraction phenomena are the basis of many techniques for investigating the structure of matter [139]. Diffraction methods are of great use for studying materials on all scales, from elementary particles to macro objects [139]. Diffraction of X-rays by a crystalline material is related to the Bragg equation: $n\lambda = 2d \sin\theta$ where θ is the angle of diffraction. The equation indicates θ that yields constructive interference, varies inversely with the characteristic length scale under investigation, e.g. the spacing of the diffracting lattice planes [54]. As in many circumstances it is desirable to detect large lattice spacings, e.g. of the order of tens or hundreds of interatomic distances, one might consider using a longer-wavelength radiation beam to obtain larger diffraction angles. However, longer-wavelength radiation is generally absorbed significantly upon interaction with matter, thus the intensity of the diffracted beam is considerably diminished [54] and only has limited use for studying dilute polymer solutions to obtain low q data. Therefore, the use of X-rays for studying nanometer sized materials remains essential and the diffraction pattern corresponding to the superatomic structures lies in the small-angle region [139].

small-angle X-ray scattering (SAXS) has a great potential for analysing the inner structure of disordered systems and very often the application of this technique is a unique way to obtain structural information on systems which contain inhomogeneities in nanometer range [140].

In SAXS, X-ray scattering from objects with sizes larger than the X-ray wavelength are recorded at very low angles (typically $\theta \sim 1/d$ e.g. $\theta = 0.1 - 10^o$). This angular range contains information about size, shape, and size distribution of nano or micro-structures. SAXS is applicable to solid and liquid materials that may contain solid, liquid or gaseous domains (particles) of the same or different material in any combination. The scattering results from the density difference of the domains (particles) and the matrix material they are embedded in, e.g. ion tracks in a solid, that have electron densities different from that of the matrix in order to become visible in SAXS. The contrast depends on the difference in the electron densities between the two materials (track and the matrix), as well as the volume of the scattering objects. In contrast to conventional X-ray diffraction, where the density differences (on the atomic scale) consist of highly-ordered periodic structures, the domains studied by SAXS are usually less ordered, can have complex shapes, and are often made up of an ensemble of randomly oriented polydisperse objects. Generally some prior knowledge is required to adequately interpret the scattering patterns.

Ion tracks are highly-monodisperse parallel and well separated objects when generated using an accelerator and low ion fluences. As such, SAXS can provide essential information about the morphology of "individual" track.

3.4.1 Basic principles

The scattering of one particle is the interference pattern produced by all emitted waves from the atoms/electrons of that particle. The square of the sum of all the wave amplitudes at the detector position results in the observed scattering pattern. This pattern is characteristic of the shape (form) of the particle manifested in the so called form factor, $F(\mathbf{q})$. When the scattering objects in a sample (e.g. ion tracks) are all identical in shape and size and far away from each other (negligible track overlap), the observed scattering pattern corresponds to the form factor of one shape only. The form factor of scattering objects used in this thesis is discussed in section 3.4.2.

$F(\mathbf{q})$ is a function of the scattering vector, $\mathbf{q} = \mathbf{K} - \mathbf{K_0}$, where $\mathbf{K_0}$ and $\mathbf{K}$ are the incident and the scattered beam. The magnitude of $\mathbf{q}$ is equal to $q = 4\pi \sin(\theta)/\lambda$ where λ is the wavelength of the X-ray beam. The unit of $\mathbf{q}$ is one over length (e.g. $1/\mathring{A}$).

The result of a SAXS experiment is essentially the intensity of the Fourier transform of the electron density that is interpreted in order to determine the morphology. The recorded scattering intensity is proportional to the the square of the sum of all the wave amplitudes. For a scattering object with volume V and constant electron density of ρ_1 which is embedded in a matrix of electron density ρ_2, the scattering intensity is:

$$I(\mathbf{q}) = \Delta\rho^2 V^2 F(\mathbf{q})^2 \tag{3.6}$$

where $\Delta\rho = \rho_1 - \rho_2$. For an ensemble of n identical scattering objects, the equation becomes:

$$I(\mathbf{q}) = n\Delta\rho^2 V^2 F(\mathbf{q})^2 S(\mathbf{q}) \tag{3.7}$$

where the additional term, $S(\mathbf{q})$ is the structure factor and n is the number density of the identical scattering objects. $S(\mathbf{q})$ contains information about the spatial arrangement between the scattering objects. If the distances between the particles (scattering objects) inside a material is in the same order of magnitude as their sizes, the contribution from the neighboring particles affects the scattering intensity and gives rise to $S(\mathbf{q})$. The structure factor of highly-ordered or periodic arrangements can appear as a pronounced peak in the scattering signal.

In the case of diluted systems and/or randomly distributed scattering objects the structure factor is close to $S(\mathbf{q}) = 1$. This is the case in our system which comprises of monodisperse ion tracks in a material generated with relatively low fluences, yielding well separated randomly oriented tracks with no periodic arrangement, e.g. distances between neighboring tracks are much larger than the diameters of tracks.

Later, we discuss the form factor relevant to cylindrical ion tracks and explain how the scattering intensity from tracks is modeled based on assuming different electron density profiles for the tracks with respect to the matrix.

3.4.2 Polydispersity

With few exceptions of some protein solutions, often scattering objects in a sample have a range of different sizes which is called polydisperse. This leads to a damping of the characteristic oscillations in the overall spectra, as shown in figure 3.11. The figure shows simulated spectra of cylinders of different radii exampling the shift in the characteristic oscillations. Also shown is a spectrum of a cylinder with a Gaussian distribution in the radius with a width of about 10%. The damping of the oscillations is clearly apparent. Generally it is the aim to prepare samples with the highest possible degree of monodispersity.

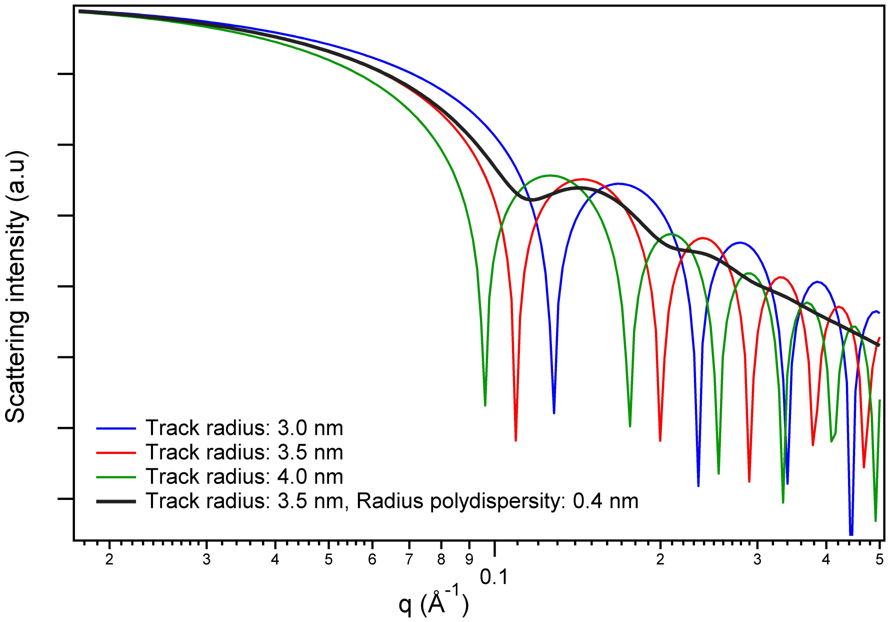

Figure 3.11: Scattering patterns from cylindrical objects with radii of 3.0, 3.5, and 4.0 nm without radius polydispersity are shown in blue, red, and green, respectively. The black spectrum is from a cylindrical object with radius of 3.5 nm and a normal radius distribution with a width of 0.4 nm.

Ion tracks are highly-monodisperse, oriented scattering objects as they are generated under controlled irradiation conditions. However, for SAXS data modeling, in order to account for deviations from exactly identical track models we consider polydispersity in the form of very narrow normal distributions with widths in the order of 9% to 12% of the track radius.

3.4.3 SAXS beamline at the Australian Synchrotron

Transmission SAXS experiments of ion tracks were performed at the SAXS/WAXS beamline of the Australian Synchrotron. The beamline facilitates small and wide angle X-ray scattering experiments. Figure 3.12 shows the end station of the beamline.

Figure 3.12: Photo of the SAXS/WAXS beamline of the Australian Synchrotron. (Image courtesy: Australian Synchrotron)

The beamline provides X-rays with the energy in the range of 5.2 to 21 keV. A detailed layout of the beamline is shown in fig 3.13. The raw "white-beam" is supplied by a 3 m long in-vacuum undulator on to a cryo-cooled Si(111) double crystal monochromator. A set of horizontal and vertical focusing mirrors are in place to provide the monochromatic beam with variable focus for different camera lengths. Three mirror stripes (Si, Rh, Pt) allow full coverage of the energy range rejecting higher energy harmonics and can be removed for specialty experiments. The maximum flux at the sample is 2×10^{13} photons per second with a beam size of 250 μm horizontal × 150 μm vertical (FWHM). A smaller beam size is achievable by constraining the beam using variable slits.

Two Pilatus detectors are used for SAXS (1M detector) and WAXS (200k detector) which may be run simultaneously with excellent dynamic range, low noise and short exposures times with up to ~30 frames per second. A MAR-165 CCD (165 mm diameter) is also available for SAXS data collection. Using multiple camera lengths, a q-range of 0.0015 - 1.1 $\mathring{A}^{-1}$ is achievable for SAXS.

3.4.4 Experimental setup

After irradiation of the samples with a variety of high-energy ions, samples were thinned down mechanically and without further preparation these samples were investigated using

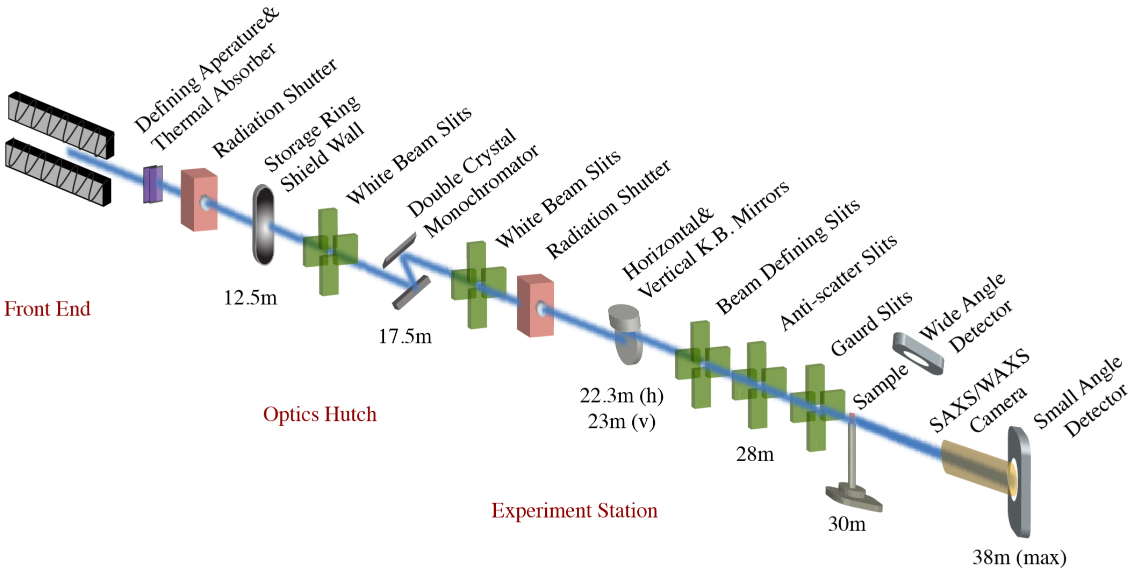

Figure 3.13: Schematic layout of the SAXS/WAXS beamline of the Australian Synchrotron.

transmission SAXS.

Figure 3.14 shows the experimental setup. The sample is mounted on a 3-axis goniometer between the high vacuum outlet of the X-ray beam and the evacuated camera tubes leading to the detector that records the scattered beam from the ion tracks. The goniometer allows precise alignment of the ion tracks with respect to the X-ray beam. Measurements are generally taken with the ion tracks aligned and tilted by 2° to 10° with respect to the incoming beam. Additionally, scattering is measured from an unirradiated sample for background removal and from a glassy carbon standard for absolute calibration of the scattering intensities. Spectra are collected with the Pilatus 1M detector with exposure times between 2 s and 30 s.

The scattering intensity scales with the square of the particle volume which means small particles are less visible in the presence of large particles. The sample detector distance can be adjusted between about 50 cm and 700 cm. When the detector is closer to the object, it can record larger scattering angles and therefore resolve smaller details. The farther the object is from the detector, the smaller scattering angle and larger objects can be resolved. All the measurements in this work were performed with an X-ray energy of 12 keV and a camera length of approximately 1600 mm.

Experimental calibration

In order to determine the optimum setup for each SAXS experiment, a specific camera length (sample-to-detector distance) and X-ray wavelength is chosen to access the required q-range [141]. Accurate determination of the camera length needs to be performed to calibrate the scattering angle θ (and thus q). At the Australian Synchrotron, a Silver behenate sample is usually measured as a standard. Silver behenate with d = 3.838 nm is a commonly used periodic calibrant for SAXS measurement [142]. Figure 3.15 shows

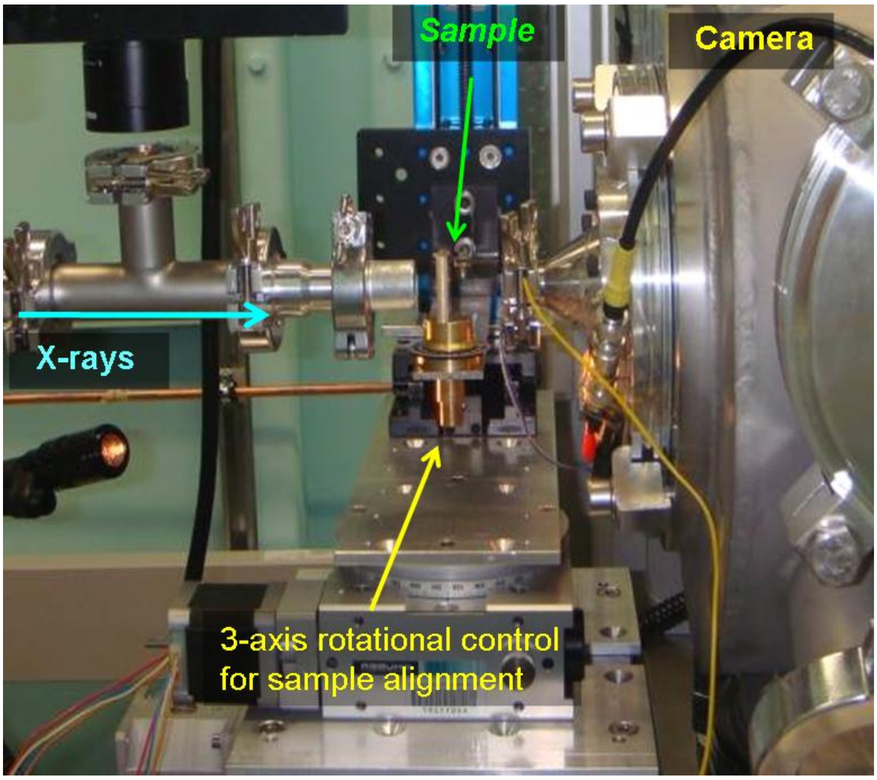

Figure 3.14: SAXS experimental setup at the Australian Synchrotron.

a SAXS image from a Silver behenate sample and the corresponding intensity spectrum. The spectrum from the standard sample has clear sharp peaks with known positions in q. By comparing the position of these peaks with that predicted from the Braggs law, the sample to detector distance can be calibrated. Also the center of the primary beam can be determined from the center of this circular peak. Based on this measurement, we can calculate the camera length and calibrate the scattering angles [143].

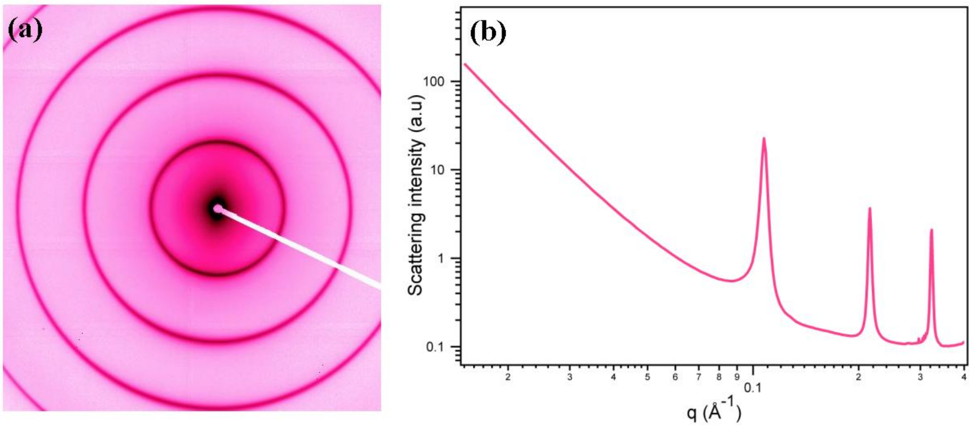

Figure 3.15: SAXS image (a) and scattering spectrum (b) from a Silver behenate sample for camera length calibration.

Absolute scattering intensities

In some cases e.g. for calculating the absolute electron density difference between the ion tracks and their matrix, scattering intensities are required in absolute units of cm^{-1}. By dividing the scattering intensity of a sample by the intensity of a reference material, one can one can obtain the intensities in units of the reference [144].

At the Australian Synchrotron, a Glassy carbon sample is usually measured as a reference. In addition to measuring the Glassy carbon sample, the scattering intensity without a sample, resulting from the scattering from the air path around the sample holder is also measured. By subtracting the intensities of the air shots from the intensities of the Glassy carbon with the same exposure times, the scattering intensity of the reference is calculated.

3.4.5 Annealing of ion tracks

To study the annealing kinetics of the ion tracks, isochronal annealing experiments as a function of temperature (*ex situ*) and isothermal annealing as a function of time (*in situ*) were performed on the irradiated samples.

For the *ex situ* annealing experiments, irradiated samples were annealed in a furnace at elevated temperatures and after each annealing step, the SAXS measurements were performed to study the fine changes in the track radii as a function of temperature. In contrast to etching experiments, the same sample can be used for a complete annealing series, thus reducing uncertainties associated with processing of multiple samples.

In situ annealing experiments were facilitated in two ways; either by using a hot-air heater that was positioned underneath the samples or by using a dedicated heating stage as shown in figure 3.16. When using the hot-air heater the sample was placed in front of the X-ray beam and its temperature was monitored with a thermocouple at the sample height. The commercial LINKAM TS1500 heating stage in figure 3.16 was used to anneal ion tracks in a temperature range of up to 1100 °C. The sample was placed inside the ceramic sample cup (2.5 mm deep sample cup) so that the sample is heated from underneath as well as from the sides. The temperature controller enabled the stage to heat samples up to 130 °C/min. The inset in figure 3.16 shows the heating element that holds the sample.

3.4.6 Data analysis and modeling

After the SAXS measurements are performed, the first step is to extract the scattering intensities from the ion tracks and then develope appropriate models based on the relevant electron density profile of the tracks to fit the SAXS spectra.

Data reduction

During SAXS measurements, aligning the ion tracks parallel/collinear to the X-ray beam (0°) results in isotropic scattering. Figure 3.17 (a) shows the isotropic scattering in collinear geometry for tracks in a quartz sample generated by 2 GeV ^{197}U ions to a fluence of 5×10^{10} ions/cm^2. Due to the parallel orientation of the ion tracks, the radial symmetry is consistent with a circular cross section of the track cylinders or random

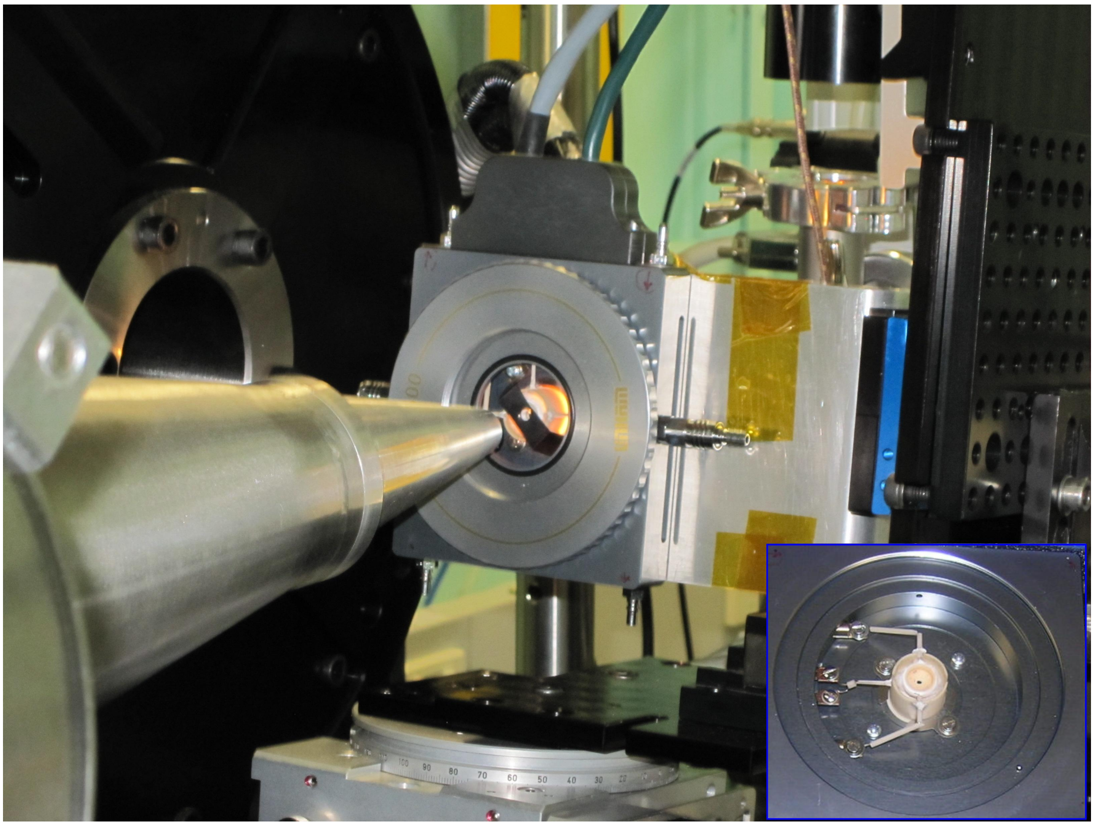

Figure 3.16: Picture of a heating stage in front of the beam. The inset shows the heating element.

orientation of tracks with a non-circular cross-section, e.g. faceted tracks. By tilting the sample from this position, the scattering changes to two slightly curved streaks as apparent from figure 3.17 (b), (c), and (d), which show the same sample tilted by 2°, 5°, 10°, respectively. This anisotropy results from the large aspect-ratio of the tracks that are only few nanometers wide, but tens of micrometers long.

For SAXS data analysis, the scattering intensities are extracted by masking and angularly integrating the intensity from the streaks of the anisotropic images of the irradiated samples as shown in the inset of figure 3.18. To remove the background intensity, we subtract the scattering signal of an unirradiated sample from the scattering signal of the streaks using the Irena computer program [145] which is a tool suited for analysis of both X-ray and neutron small-angle scattering data within the commercial Igor Pro application [146]. The X-ray scattering intensities of radial sectors perpendicular to the streaks (e.g. small arc sectors in the area between the two streaks which do not overlap with either of the streaks) are compared to those of unirradiated samples and found to be identical. This is consistent with the lack of significant density fluctuations on the nanometer length scale along the ion tracks, confirming their cylindrical morphology. Thus we can also use the scattering intensity from the radial sectors perpendicular to the streaks as the background signal. This often provides a slightly better background signal as it for example contains sample specific shadowing effects.

Figure 3.18 shows the scattering signal from the streaks as well as the background and

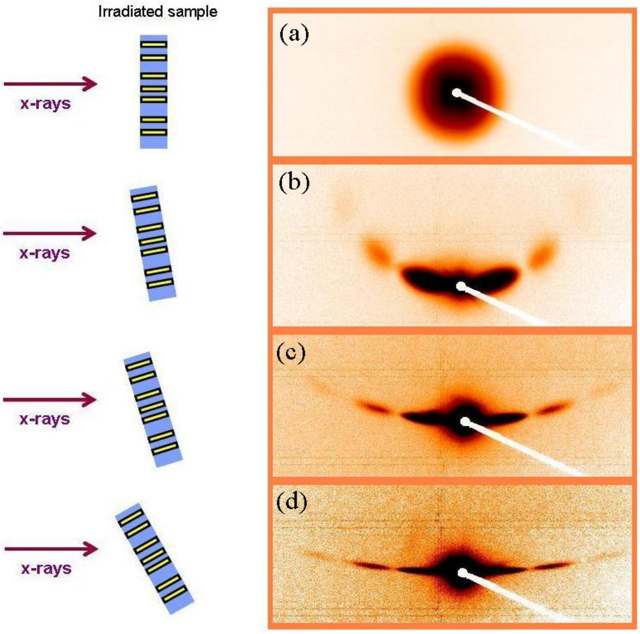

Figure 3.17: SAXS images of ion tracks in quartz irradiated by 2 GeV ^{197}U ions to a fluence of 5×10^{10} ions/cm^2. From top to bottom, tracks are tilted in front of the X-ray beam by 0°, 2°, 5°, and 10°.

the background-subtracted signals. The inset demonstrates how different scattering signals are masked and extracted from an anisotropic SAXS image (note the color coordination of the mask and the extracted data).

Data modeling

In order to analyse the SAXS data, we need to define appropriate models for the ion tracks that fit the measured data. The theoretical models are then used to fit the SAXS spectra using non-linear least-squares fitting. The models are defined by assuming that the ion tracks are parallel, and almost identical cylindrical scattering objects. This assumption is justified as the energy losses of the ions for the conducted experiments are well above the threshold for continuous track formation. Using relatively low fluences and because the tracks are randomly distributed, ion tracks in the matrix represent a dilute system, therefore we assume the structure factor to be equal to 1.

Figure 3.19 shows a basic schematic of the scattering geometry with a cylindrical scattering object. The general expression for the scattering intensity was shown in equation 3.7 as a function of the scattering vector, $\mathbf{q}$:

$$I(\mathbf{q}) = n(\Delta\rho)^2 V^2 F(\mathbf{q})^2 S(\mathbf{q}) \tag{3.8}$$

This equation is strictly valid only if $\Delta\rho$ is constant. Our considered track models include a possible radial variation in the electron density. The scattering intensity can then be written as:

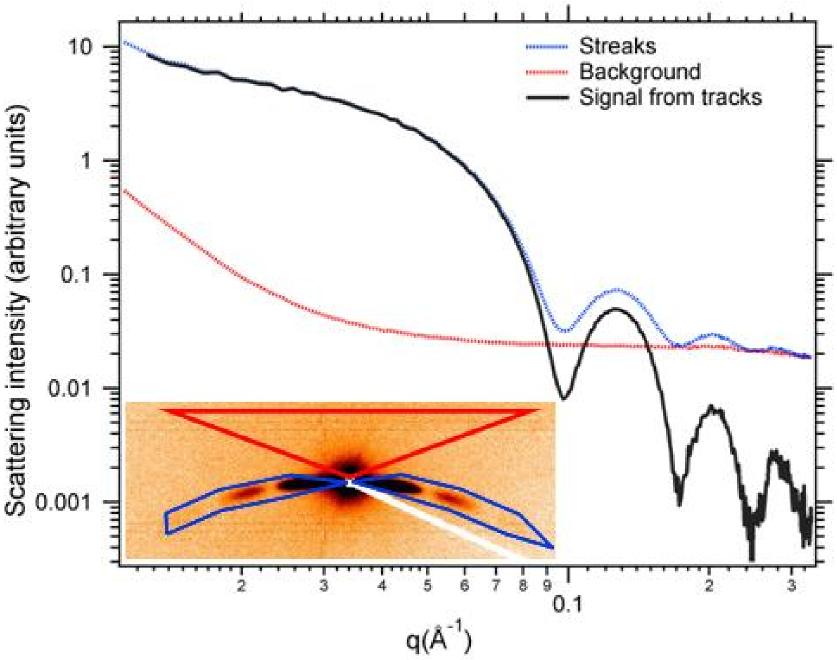

Figure 3.18: Scattering intensity from masking the streaks and the area perpendicular to the streaks which is taken as the background. By subtracting the background intensity, the scattering intensity from ion tracks is obtained. The inset shows a typical SAXS image of ion tracks tilted in front of X-ray beam.

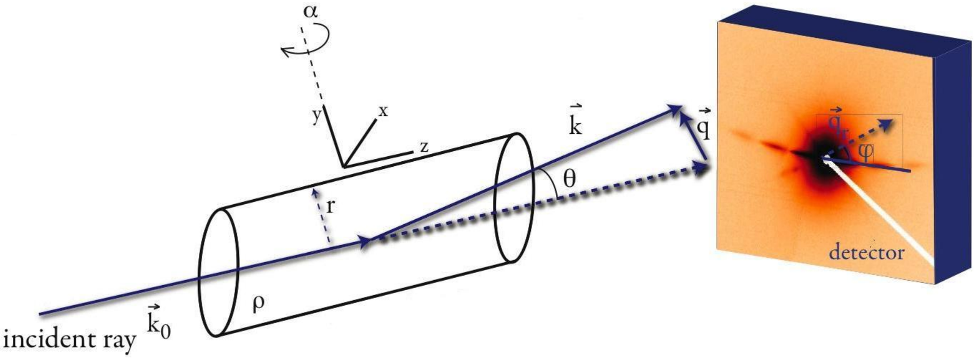

Figure 3.19: Schematic of the transmission SAXS geometry.

$$I(\mathbf{q}) = nV^2 f(\mathbf{q})^2 S(\mathbf{q}) \tag{3.9}$$

where the scattering amplitude, $f(\mathbf{q})$, includes the form factor and the electron density:

$$f(\mathbf{q}) = \int_{-\infty}^{\infty} \Delta\rho(\mathbf{r}) \exp(i\mathbf{q}\mathbf{r}) d\mathbf{r} \tag{3.10}$$

As the cylindrical tracks have a radial symmetry, it is convenient to write the equations in cylindrical coordinates (figure 3.19). Furthermore we assume rotational symmetry of $\Delta\rho$ around the track centre as well as translational symmetry along the ion track, therefore $\Delta\rho(\mathbf{r}) = \Delta\rho(r)$. $\mathbf{q}$ can be written as $\mathbf{q} = q_x, q_y, q_z = q_r \cos\varphi, q_r \sin\varphi, q_z$. The volume element is $d\mathbf{r} = r dr d\phi dz$ and by taking the centre of the track as the coordinates origin, we get:

$$f(\mathbf{q}) = \int_{-L/2}^{L/2} \int_0^{\infty} \int_0^{2\pi} \Delta\rho(r) r \exp(i\mathbf{qr}) dz dr d\theta \tag{3.11}$$

By replacing $\mathbf{q}.\mathbf{r}$ with $r.q_r.\cos\varphi.\cos\theta + r.q_r.\sin\varphi\sin\theta + z.q_z$, we have

$$f(\mathbf{q}) = \int_{-L/2}^{L/2} \exp(izq_z)dz \int_0^{\infty} \Delta\rho(r).r \int_0^{2\pi} \exp(irq_r\cos(\varphi-\theta))drd\theta \tag{3.12}$$

We can substitute $\psi = \theta - \varphi$ and solve the last integration and arrive at:

$$f(\mathbf{q}) = \int_{-L/2}^{L/2} \exp(izq_z)dz \int_0^{\infty} \Delta\rho(r) r 2\pi J_0(rq_r) dr \tag{3.13}$$

Where J_0 is the first order Bessel function. The integration over z can also be done yielding:

$$f(\mathbf{q}) = 4\pi L \frac{\sin(q_z L/2)}{q_z} \int_0^{\infty} \Delta\rho(r) r J_0(rq_r) dr \tag{3.14}$$

$\mathbf{q}$ is no more dependent on φ and by applying the small-angle approximation, (e.g. $q_z \to 0$) the scattering amplitude for a track with a length of L and radial density profile of $\Delta\rho(r)$ is:

$$f(q_r) = 2\pi L \int_0^{\infty} \Delta\rho(r) r J_0(rq_r) dr \tag{3.15}$$

To model the scattering intensity of tracks, we assume a number of plausible density profiles $\Delta\rho(r)$. In the simplest case $\Delta\rho(r)$ can be a “hard cylinder” [46, 147, 148] where there is a sharp transition between the electron density inside and outside of the ion track. In this the case track is assumed to have a constant electron density different from that of the matrix as shown in figure 3.20 (a). Another model assumes that $\Delta\rho(r)$ has a smooth transition from the center of the track to the matrix material, like a Gaussian function which is called “soft-cylinder” model and is shown is figure 3.20 (b). A further example of a density profile is the core-shell cylinder [63] in figure 3.20 (c) where track has a constant $\Delta\rho(r)$ and is surrounded by a shell of a different but also constant $\Delta\rho(r)$ compared to the matrix material.

Assuming the hard-cylinder model with the electron density difference of ρ_0 between the track and the matrix, and track radius R, the scattering amplitude can be simplified to:

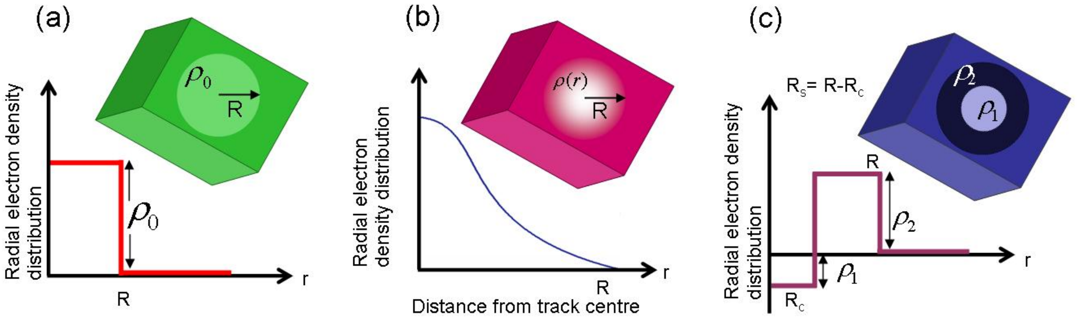

Figure 3.20: Electron density profiles of an ion track with respect to that of the matrix material in a) hard-cylinder b) soft-cylinder and c) core-shell models.

$$f(q_r) = 2\pi L \int_0^R \rho_0 r J_0(rq_r) dr \tag{3.16}$$

and yields:

$$f(q_r) = \frac{2\pi L R \rho_0}{q_r} J_1(Rq_r) \tag{3.17}$$

where J_1 is the first order Bessel function.

For the soft cylinder model, the electron density profile has the form of:

$$\Delta\rho(r) = \rho_0 \exp(-(\frac{r}{R})^n) \tag{3.18}$$

where n parameterises the smoothness of the transition of the electron density from the track to the matrix material. Soft-cylinder relative density profiles are compared with the hard-cylinder model in figure 3.21 for different values of n. In the limit of $n > 7$, soft cylinder model is very close to the hard-cylinder density profile.

When n equals 2, the density function is a Gaussian distribution and equation 3.15 has an analytical solution:

$$f(q_r) = 2\pi L \int_0^\infty \rho_0 \exp(-(\frac{r^2}{R^2}) r J_0(rq_r) dr \tag{3.19}$$

that yields:

$$f(q_r) = \pi R^2 \rho_0 \exp(-\frac{q_r^2 R^2}{4}) \tag{3.20}$$

For $n \neq 2$, equation 3.19 needs to be numerically solved.

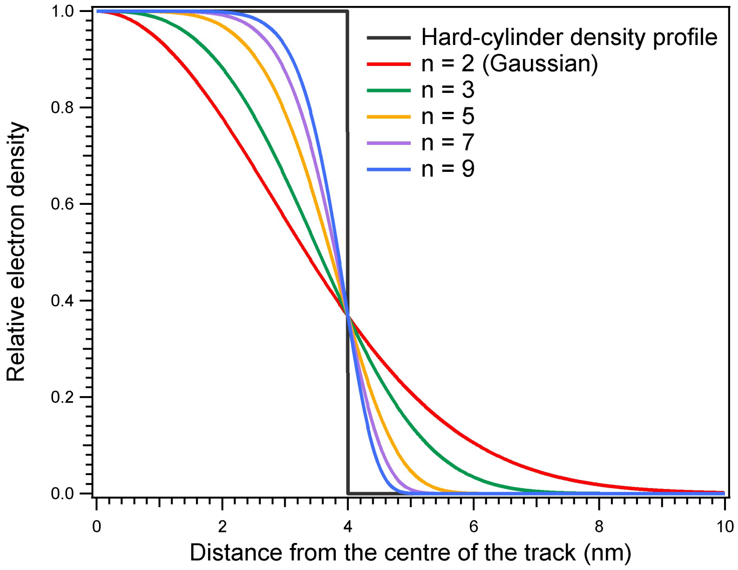

Figure 3.21: Comparison of the relative density profile of an ion track with soft-cylinder and hard-cylinder models. Parameter n denotes the smoothness of the transition between track and the matrix.

In case of the core-shell cylinder model, where there are two step functions, equation 3.15 yields:

$$f(q_r) = 2\pi L\left[\int_0^{R_c} \rho_1 r J_0(rq_r)dr + \int_{R_c}^{R} \rho_2 r J_0(rq_r)dr\right] \tag{3.21}$$

where R_c and R_s are the core radius and the shell thickness, respectively ($R = R_c + R_s$) and ρ_1 is the electron density difference between the core and the matrix and ρ_2 is the electron density difference between the shell region and the matrix material. By simplifying 3.21, we have:

$$f(q_r) = 2\pi L\left[(\rho_1 - \rho_2)\frac{R_c}{q_r}J_1(R_c q_r) + \rho_2\frac{(R_c + R_s)}{q_r}J_1((R_c + R_s)q_r)\right] \tag{3.22}$$

To account for a variation of the track radius over the depth of the tracks due to changes in the stopping powers and deviations from perfectly identical tracks, a narrow Gaussian distribution of the track radii is assumed [63, 46, 147]:

$$r = 1/\sigma_r.e^{-(r-R)^2/(2\sigma_r)^2} \tag{3.23}$$

In some cases a narrow angular distribution of tracks was assumed to account for deviations from perfectly parallel tracks:

$$\alpha = 1/\sigma_\alpha.e^{-(\alpha-\pi/2)^2/(2\sigma_\alpha)^2} \tag{3.24}$$

that result from beam divergence during irradiation or bending of the thin samples. Another modification considered is a phenomenological damping factor: $e^{-\sigma_D^2 q}$ which accounts for roughness between the track and the surrounding matrix [140] where σ_D is the width of a normal distribution. This was used to simulate roughening of the track boundaries during annealing experiments. Fitting of the distribution in radii, the angular spread, and the roughness parameter had no considerable influence on the fitted track radii.

In order to find the best density profile of the ion tracks in different materials, several models were fitted to the SAXS spectra and generally the simplest model that could generate the best fit to the data was chosen.

Applying the theoretical models to SAXS data by non-linear least-squares fitting normally results in uncertainties in the order of angstrom or less for the extracted track radius. However, this value does not include the uncertainties associated with the masking of the ion track signal from the SAXS images (that can only be estimated). Therefore, in order to report the uncertainties of the extracted track properties from SAXS measurements (reported results in chapters 4 and 5), for each sample, we have analysed several SAXS images with different tilted angle or exposure time and reported the standard deviation of the averaged track property (e.g. radius) as the error for the measurement. These error values which are in the order of a fraction of a nanometer are thus representative of the overall uncertainty of the SAXS measurement and not just the error of the fitting of a given model. We note that possible uncertainties related to the experimental setup e.g. accuracy of the camera length were estimated to be well within these errors.

SAXS simulation

Analysis of the SAXS scattering intensities in this thesis are performed by extracting the track intensity as a function of the scattering vector and developing one dimensional models to fit the data and extarct a radial density profile of the cylindrical tracks. However, SAXS images from the detector are two dimensional and developing models that can fit the 2D SAXS data can ultimately eliminate the need for masking the track signal from the images and therefore reduce the uncertainties associated with extracting the 1D spectra as well as obtaining information about more complex 3D track morphology, e.g. track fragmentation during annealing . Here, we present preliminary simulation results of SAXS images from samples with cylindrical ion tracks. Even though at this stage the 2D models do not have capability to fit the experimental data, they provide a possibility to predict the signal from tracks with different sizes.

The simulation of ion track scattering images are based on the formulation in reference [149]. The three components of the scattering vector, $\mathbf{q}$, are q_x, q_y, and q_z. To find the scattering intensity from tracks one can use the transformation for the scattering vector components in cylindrical coordinates as [149]:

$$\begin{aligned}
q_x &= (2\pi/\lambda)[\cos(\alpha)\sin(\theta)\sin(\phi) + \sin(\alpha)(\cos(\theta) - 1)], \\
q_y &= (2\pi/\lambda)[\cos(\beta)\sin(\theta)\cos(\phi) - \sin(\beta)(\sin(\alpha)\sin(\theta)\sin(\phi) - \cos(\alpha)(\cos(\theta) - 1))], \\
q_z &= (2\pi/\lambda)[-\sin(\beta)\sin(\theta)\cos(\phi) - \cos(\beta)(\sin(\alpha)\sin(\theta)\sin(\phi) - \cos(\alpha)(\cos(\theta) - 1))]
\end{aligned} \tag{3.25}$$

where θ and ϕ are the polar and azimuthal scattering angles, respectively, α and β are the horizontal and vertical tilting angles of the track axis with respect to the incident beam, respectively. Using these transformations, we modeled the scattering intensity for different track sizes and different angles with respect to the incident X-ray beam, results of which are shown in figure 3.22. When tracks are parallel to the incoming beam, the observed scattering is symmetrical in the $q_x - q_y$ plane (figure 3.22 (a)). A slight tilt (as small as $1\circ$) from this position results in extremely asymmetric feature that can be understood by considering the intersection of a disk (cylinder in inverse space) with the Ewald sphere [140, 149]. In limits of large tilting angles, as shown in figure 3.22 (d), the scattering intensity approaches a straight line. For tilted samples, apart from the low frequency main oscillations, fine oscillations are observed in normal direction to the main oscillations, yet their existence is not experimentally confirmed.

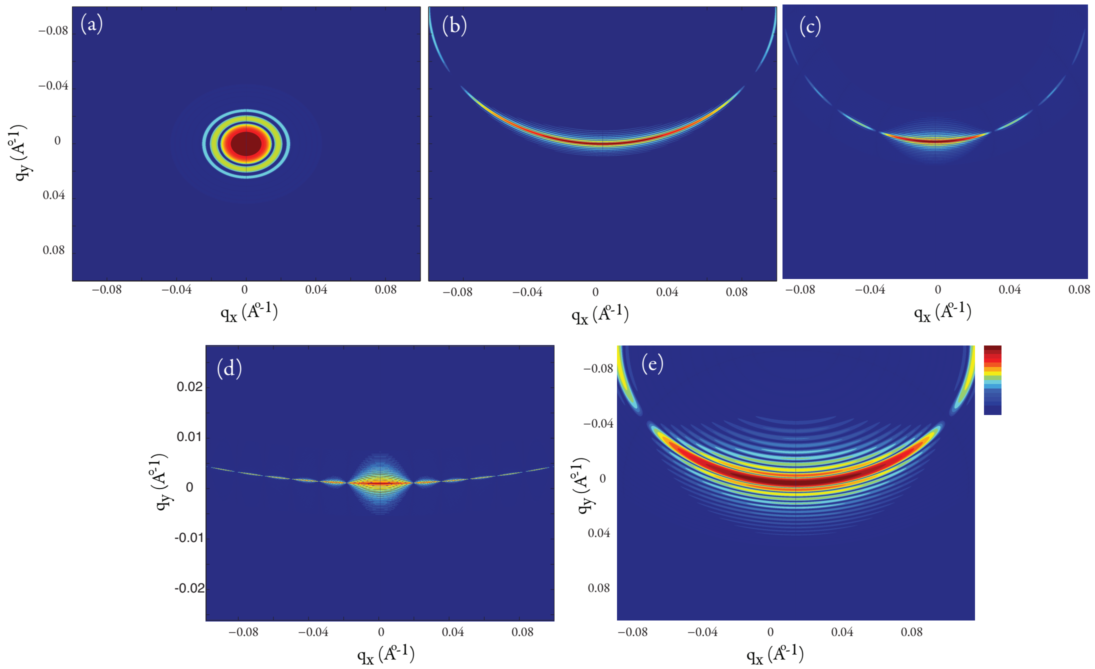

Figure 3.22: Simulation results of scattering intensities from ion tracks with, (a) $R = 4$ nm, $L = 30$ μm and $\alpha = 0$, (b) $R = 4$ nm, $L = 30$ μm and $\alpha = 1°$, (c) $R = 10$ nm, $L = 30$ μm and $\alpha = 1°$, (d) $R = 4$ nm, $L = 30$ μm, and $\alpha = 10°$, (e) $R = 4$ nm, $L = 10$ μm and $\alpha = 1°$. For all cases $\beta = 0$.

Chapter 4

Morphology of ion tracks in quartz, apatite and olivine

In this chapter results of the morphology of ion tracks in synthetic quartz and two minerals, Durango apatite and San Carlos olivine, are presented. Ion tracks are generated by swift heavy ion irradiation of the samples with a variety of ions and energies. Track radii are measured using SAXS and studied as a function of the irradiation parameters.

4.1 Quartz

Silicon dioxide (SiO_2) or silica is one of the most abundant minerals of the earth's crust with a wide variety of crystal structures. Figure 4.1 shows the phases of SiO_2 as a function of temperature and pressure. More information on the properties of the different phases of SiO_2 can be found in reference [150].

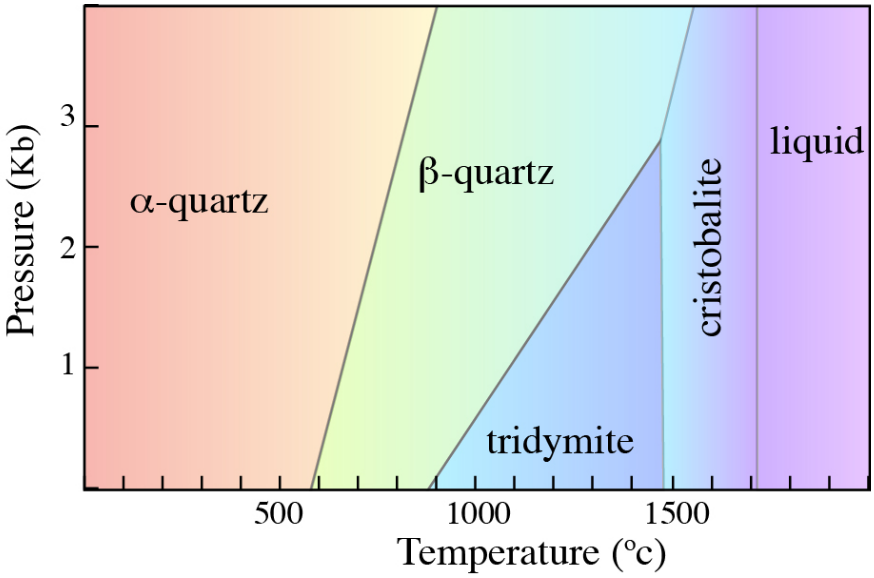

Figure 4.1: The phases of SiO_2 in different temperature and pressure range.

The most common and stable phase of all known crystalline forms of SiO_2 is α-quartz. The α-quartz structure is hexagonal in cross-section and has two pyramidal ends. The crystal can be thought of as a trigonal system with a six-sided prism terminating by six-sided pyramids. It consists of SiO_4 tetrahedral units connected by common oxygen vertices, forming a helix around the c-axis which provides a three-fold symmetry [151, 152]. A schematic of the crystalline structure of α-quartz is shown in figure 4.2. In this thesis, α-quartz is referred to as quartz.

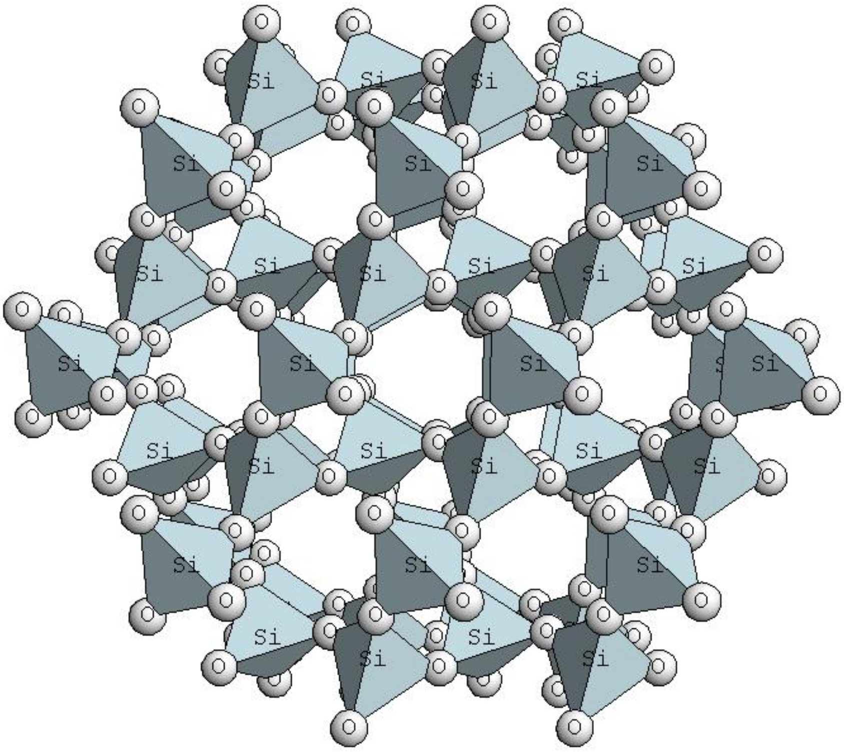

Figure 4.2: Crystal structure of α-quartz showing the SiO_4 tetrahedral units. The c-axis of the crystal is normal to the picture plane.

α-quartz is hard, brittle, and has a density of 2.65 g/cm^3 with a high melting point of 1710 °C [153]. As it has a wide band gap of about 9 eV [154], it is optically transparent and shows low electrical conductivity. It is also resistant to chemical weathering and corrosion because of the high Si-O bond energy [153]. Annealing of quartz above 573 °C causes the crystal to change phase from the stable form of α to β quartz.

The piezoelectric properties of quartz have led to its wide use in electronic circuits for accurate frequency control, timing, and filtration. Its optical properties on the other hand are advantageous for windows and lenses in specialized devices including some lasers. The use of natural quartz in electronic and optical applications diminished in early seventies when the synthetic quartz took the lead. Nowadays, applications of natural quartz are limited to carvings and other gemstone applications as well as geological studies using fission tracks [155, 156].

4.1.1 Ion tracks in quartz

Ion tracks in quartz (crystalline SiO_2) are of interest due to the unique optical properties of the crystal. Quartz is transparent over a wide spectral range, with a low coefficient of thermal expansion and good endurance against wear and fatigue that make it a suitable material for optical devices [157, 31, 33]. Crystalline quartz is also used as an essential electronic component for various devices due to its great frequency stability over a wide temperature range [158, 159]. Swift heavy ion irradiation of quartz leads to a change in the refractive index and offers a means to impose an etch anisotropy in the material which paves the way for nano-fabrication and micromachining of optical devices [31, 33].

Damage in quartz induced by swift heavy ions was previously studied using transmission electron microscopy (TEM) [48, 42], Rutherford backscattering spectrometry in channeling geometry (RBS/C) [48, 160, 161], atomic force microscopy (AFM) [52], surface profilometry [52, 109], and chemical etching [162, 163, 164, 108]. RBS/C measurements [48] show a steady increase of the damage cross section with increasing electronic energy loss (dE/dx_e). The track interior is completely disordered and presumably amorphous, consistent with electron diffraction analysis of the damaged areas [48]. TEM measurements of ion tracks in thin quartz samples reveal a radial strain field around the amorphous core that extends up to a distance of three times the core radius from the track center into the crystalline matrix [42]. Swelling measurements by surface profilometry indicate significant density changes. The reported values for out-of-plane swelling vary between 4% [161] and 16% [109], the latter of which coincides with the density difference between crystalline and amorphous SiO_2. AFM investigations report conical hillocks with circular bases at the sample surface for each individual track above an energy loss of 7 keV/nm [52].

The threshold values for the electronic energy loss are subject to the so-called velocity effect, which considers the increase of the initial electron cascade for projectiles of higher velocity [48, 165]. Reported values for the track formation threshold in quartz include 4 keV/nm from RBS/C [48, 99], 4.6-7.2 keV/nm from chemical etching [6, 108], 1.8±0.5 keV/nm from Swelling measurements [109] and 4.5-5.1 keV/nm from a simple thermal spike model [165, 166] and are depending on the measurement technique and ion irradiation conditions. A more recent study on quartz indicated two amorphization values of 2.1 and 4.1 keV/nm and attributed the two-threshold effect to the appearance of discontinuous tracks in the region between the two threshold values [167]. In this RBS/C study, it is assumed that every swift heavy ion impact generates a cylindrical track of an inner amorphous core surrounded by a homogeneous defective halo [167]. According to reference [168], the threshold for damage creation varies by about 20% when comparing high and low velocity ions.

4.1.2 Sample preparation

Single crystalline wafer pieces of α-quartz were irradiated with a variety of high-energy heavy ions. Irradiations with 27, 89, and 185 MeV ^{197}Au ions were performed at the ANU Heavy Ion Accelerator Facility. For irradiations at higher energies, ^{207}Pb ions of 1 GeV at the GANIL accelerator and ^{197}Au ions (2.2 and 1.6 GeV) as well as ^{238}U ions (2 and 1.3 GeV) at the UNILAC accelerator at GSI were used. In order to vary the energy loss of the ions, degrader foils of aluminum with thicknesses between 16 and 64 μm were placed in front of some of the samples. All irradiations were performed at normal incidence and room temperature (RT). Details of the irradiation parameters are summarized in table 4.1 in the order of increasing surface electronic energy loss. The ion energies and surface energy losses were calculated with the SRIM-2008 code assuming a mass density of 2.65

g/cm^3 for quartz [169].

The average dE/dx_e for a particular irradiation energy is estimated by integrating dE/dx_e calculated by SRIM-2008 over the depth of the penetrating ion, from the sample surface to the depth where it reaches its threshold for track formation (2 keV/nm), the latter of which provides an estimate of the track length. For more information on average dE/dx_e calculation, refer to section 2.3.

Samples were irradiated with fluences between 3×10^{10} and 4×10^{11} ions/cm^2. Most samples irradiated to a fluence of 4×10^{11} ions/cm^2 fractured during the irradiation as a result of high stresses generated in the ion track regions.

All quartz samples had the same thickness of 360 μm before irradiation. After irradiation, samples were mechanically polished from the backside to thicknesses between 10 and 130 μm using a tripod method. For the high-energy irradiations (>600 MeV), the ion tracks are up to tens of micrometers long. In most cases, the thickness of the polished sample was smaller than the projected ion range, and the variation of the energy loss along the ion track less than 10%. For irradiations with ions of lower energies, the sample thicknesses exceed the track lengths. Here, thinning was performed predominantly in order to reduce absorption and inelastic X-ray scattering from the un-irradiated crystal matrix in the SAXS data.

On few selected quartz samples plan-view transmission electron microscopy (TEM) was performed using a Philips CM300 microscope operating at 300 kV at the Centre for Advanced Microscopy (CAM) at the ANU. Samples were prepared using standard polishing and ion milling processes. A 3 mm disk was cut out of the irradiated sample and mechanically polished to about 90 μm and then thinned from the un-irradiated side to a thickness of $\sim$7 μm using a dimple polisher. Finally, a Gatan Model 691 ion mill was used to thin the specimen from the unirradiated side until perforation. Ion tracks were imaged in the thin area of the sample around the hole.

As ion tracks in quartz are very susceptible to electron beam irradiation effects, the beam was focused on one spot and the image was taken after quick movement to an adjacent spot in order to record images before the tracks started to shrink in size.

4.1.3 SAXS measurements of ion tracks in quartz

Figure 4.3 (a) shows the isotropic scattering in collinear geometry for tracks in a quartz sample produced by 1.6 GeV Au ions to a fluence of 5×10^{10} ions/cm^2. Due to the parallel orientation of the ion tracks, the radial symmetry is consistent with a circular cross section of the track cylinders or a random rotation of tracks with a non-circular cross section along the track axis, the former consistent with previous studies [48]. By tilting the sample from this position, the scattering changes to two slightly curved streaks as apparent from figure 4.3 (b), which shows the same sample as in figure 4.3 (a) tilted by 5°. This anisotropy results from the large aspect-ratio of the tracks that are only a few nanometres wide, but tens of micrometers long. The presence of strong oscillations is consistent with monodisperse track radii and a sharp density change between the track and the matrix material.

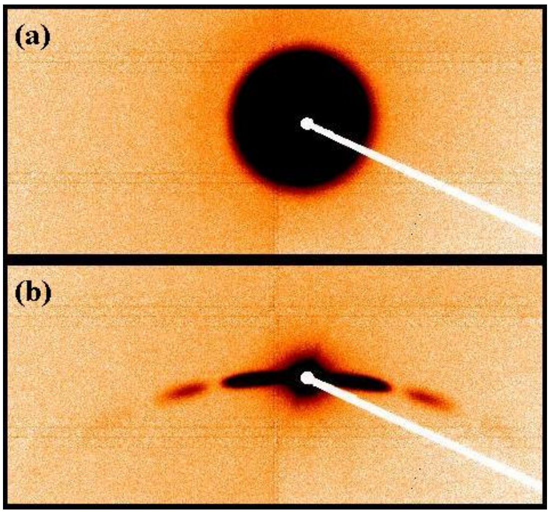

Figure 4.3: SAXS images of a quartz sample irradiated with 1.6 GeV Au ions to a fluence of 5×10^{10} ions/cm^2, (a) with the X-ray beam parallel to the ion tracks, (b) with the ion tracks tilted by 5° with respect to the X-ray beam.

For analysis of the SAXS data, the scattering intensities were extracted from the streaks in the images and scattering from an unirradiated sample was subtracted. Figure 4.4 shows the SAXS spectra from tracks for all studied irradiation conditions after background removal. While these spectra can only give information on the radial morphology of the ion tracks, the large degree of anisotropy in the tilted images and the absence of scattering perpendicular to the streaks, confirm continuous tracks with large aspect-ratio.

The most appropriate model that fits the data is a cylinder with constant density (different from that of the matrix material). This is consistent with the formation of amorphous tracks inside the crystalline quartz matrix. Other models such as the soft-cylinder model have been applied but the hard-cylinder model provides a superior fit for all the irradiation conditions as well as the annealing data presented in chapter 5. Applying the soft-cylinder model indicates a steep gradient of the density between the track and the matrix confirming the notion of a hard-cylinder.

To analyze the size of the tracks, we modeled them by parallel aligned cylinders of length L and radius R. The intensity of the scattered X-rays as a function of scattering vector $q = 4\pi \sin(\theta)/\lambda$, where 2θ is the scattering angle and λ is the wavelength of the X-ray beam, is given by:

$$I(q) \quad = \quad nV^2 \Delta\rho^2 \langle F(q) \rangle^2 \tag{4.1}$$

F(q) is the form factor of the hard-cylinder model, n is number density of the ion tracks, V is the track volume and $\Delta\rho$ is the electron density change between the track and the matrix material. To account for a variation of the track radius over the depth of the tracks due to changes in the stopping powers, and deviations of perfectly sharp boundaries

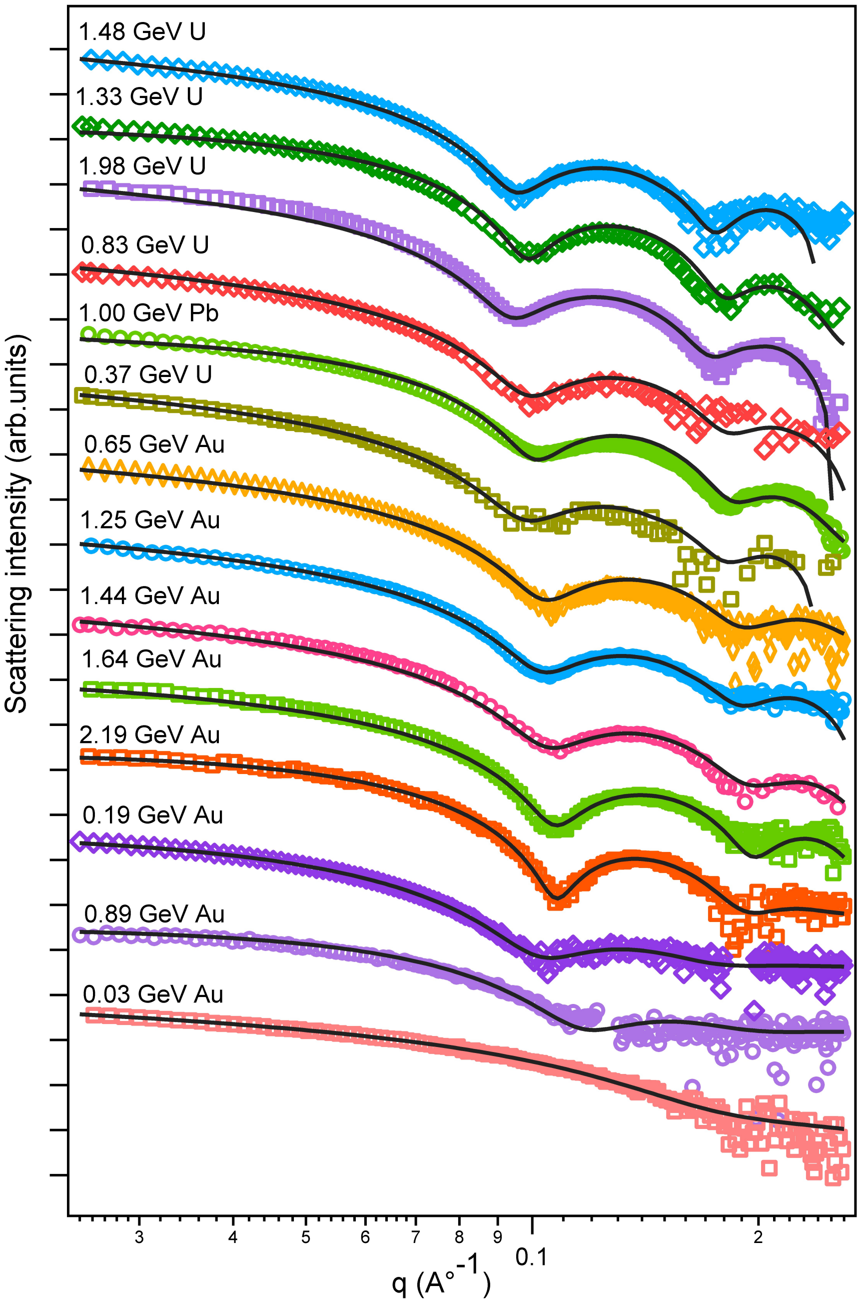

Figure 4.4: SAXS spectra of ion tracks in quartz as a function of the scattering vector q for a variety of ion/energy combinations. The scattering intensities have been offset for clarity. The solid lines are the corresponding fits to the hard cylinder model. Spectra are plotted in the order of increasing surface dE/dx_e from bottom to the top.

between track and matrix, a narrow Gaussian distribution of the radius is assumed. Furthermore, a narrow angular distribution was fitted to model deviations from perfectly parallel tracks that result from beam divergence during irradiation or bending of the thin samples. For all samples the angular spread was small and best described by a fit below 0.2°. Fitting of both the distribution in radii and the angular spread had no influence on the fitted track radii. Fits to the simple cylinder model are shown in figure 4.4 as solid lines.

By plotting the SAXS spectra on absolute intensity scale and using equation 4.1, we can estimate the absolute density change in the ion tracks given the absolute calibration of the scattering intensities for our measurements. The number density n corresponds to the irradiation fluence and the volume V of an ion track is estimated using the fitted values for the track radii and the estimated track length. In cases when the sample was thinned to a thickness smaller than the maximum track length, the sample thickness was used as the track length. Our measurements indicate an electron density change within the amorphous tracks of approximately 2±1% as compared with the crystalline matrix, independent of the irradiation conditions. Swelling measurements of quartz indicated values around 4% [161] and 15% [109] for the density change at high fluence irradiation. In these experiments, the step height at the border between an irradiated and unirradiated sample surface is recorded by profilometry. The volume expansion is due to amorphization of the irradiated material which can expand relatively freely at the surface. In contrast, SAXS measures the density change of tracks confined in the bulk matrix. At low fluences, the curvature measurements by profilometry also identified the build up of high stresses of these samples [109]. Their density change has a similar magnitude as the value observed by our SAXS experiments.

In order to investigate the effect of the ion fluence on the track radii, tracks were generated in three quartz samples using 1.4 GeV Au ions to fluences of 0.5, 1, and 3×10^{11} ions/cm^2. After extracting the scattering signal from the tracks and removing the background scattering, data were fitted using the hard-cylinder model. The scattering signals from the tracks are shown in figure 4.5 (a) along with the fits (solid lines). For the fluences of 0.5, 1, and 3×10^{11} ions/cm^2, the fits yield the track radii of 3.8±0.1, 3.7±0.1, and 3.8±0.1 nm respectively. This demonstrates that at low fluences there is no effect of the fluence on the track radius. An overlap model confirms the absence of significant track overlap at these fluences [170, 171]:

$$d = 1 - exp(-\pi R^2 n) \tag{4.2}$$

where d is the area of the modified material, R is the track radius and n is the ion fluence. The area of track overlap is then estimated as $\pi R^2 n - d$. For track radius of 3.8 nm the overlap is less than 0.1% at a fluence of 5×10^{10} ions/cm^2. At a higher fluence of 3×10^{11} ions/cm^2, the track overlap is still below 1%. Considering the amount of overlap in the irradiated area of the sample, $(\pi R^2 n - d)/(\pi R^2 n)$, there is less than 7% overlap at a fluence of 3×10^{11} ions/cm^2. The scaling of the scattering intensities with fluence in figure 4.5 (a) also further confirms that structure factor is unity.

As mentioned in section 4.1.2, ion tracks in this study sometimes exceeded the thickness of the sample and in some cases the track length was smaller than the sample thickness. To estimate the effect of sample thickness on the track radii measured from SAXS, three quartz samples of different thicknesses ($\sim$ 10, 65 and 86 μm) irradiated with 1 GeV Pb ions at a fluence of 5×10^{10} ions/cm^2 were measured. Figure 4.5 (b) shows the scattering intensity of the tracks with their corresponding fits. At this beam energy, the tracks have a length of about 44 μm and the average energy loss is 22.3

keV/nm. The scattering intensities are very similar even though the lengths of the track and the lengths of the un-irradiated part in these samples are different. The track radii for samples with the thicknesses of 10, 65 and 86 μm are 3.9±0.1, 3.8±0.1, and 3.9±0.1 nm, respectively. The thickness of the material in which the tracks are embedded has obviously no significant influence on the background-subtracted SAXS spectra and the deduced track radius.

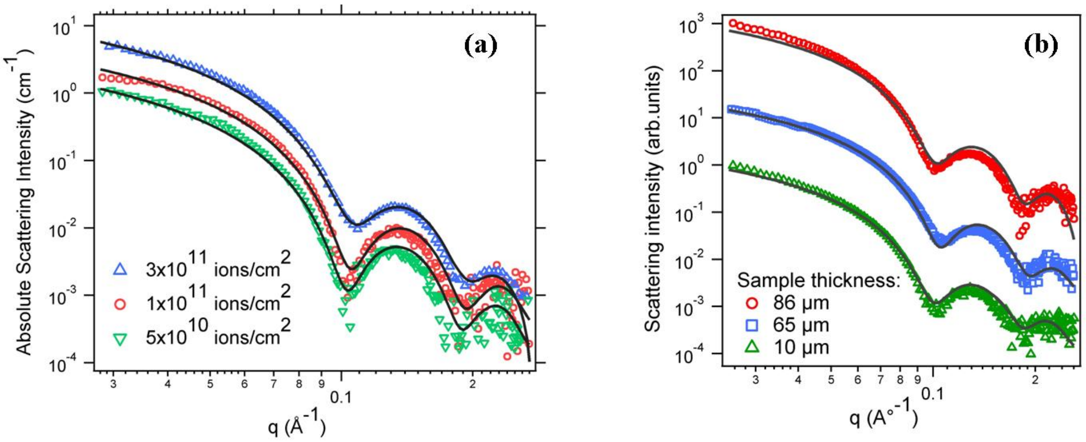

Figure 4.5: SAXS spectra from ion tracks in quartz after background removal as a function of scattering vector q. (a) Samples are irradiated with 1.4 GeV Au ions at fluences of 0.5, 1, and 3×10^{11} ions/cm^2. (b) Samples with thicknesses of 10, 65 and 86 μm are irradiated with 1 GeV Pb ions at fluences of 5×10^{10} ions/cm^2. The solid lines are the corresponding fits to the hard cylinder model.

A complete set of all SAXS radii measured and their size distributions obtained from the fits to the different measurements are listed in table 4.1.

4.1.4 TEM measurements

Figure 4.6 (a) shows a TEM image of ion tracks in quartz irradiated with 1 GeV Pb ions to a fluence of 5×10^{10} ions/cm^2 tilted with respect to the electron beam. The susceptibility of the ion tracks to the electron beam rendered acquisition of an image with clear contrast between track and matrix difficult.

For measuring track radii from the acquired images, we have analysed the intensity cross sections of tracks using their full width half maximum (FWHM) and full width full maximum (FWFM). Figure 4.7 shows an example of such measurement for one of the ion tracks. Figure 4.7 (a) shows a magnified TEM image where a selected track is marked by a circle and figure 4.7 (b) shows the intensity cross section of the track extracted from the image using the Digital Micrograph Image Acquisition and Processing Software [172]. For the selected track, the difference between the FWHM and FWFM measurements is about 4.5 nm which would result in more than 2 nm difference in the measured track radii.

The FWHM of the intensity cross sections of all tracks in the TEM images yielded a radius of 4.2±0.3 nm while the FWFM values indicated a radius of 5.5±0.6nm. As the

Ion	Initial energy (MeV/u)	Projected range (μm)	Thickness of Al degrader foil (μm)	Energy (MeV)	Average dE/dx_e (keV/nm)	Surface dE/dx_e (keV/nm)	Radius (nm)	Polydispersity of track radius (nm)
^{197}Au	0.14	5	-	27	3.6	5.4	2.3 ± 0.2	0.5 ± 0.1
^{197}Au	0.45	11	-	89	7.0	14.4	3.3 ± 0.2	0.5 ± 0.1
^{197}Au	0.94	17	-	185	10.5	20.1	3.7 ± 0.1	0.4 ± 0.1
^{197}Au	11.1	95	-	2186	23.8	24.1	3.6 ± 0.1	0.3 ± 0.1
^{197}Au	8.3	73	-	1635	23.2	25.4	3.6 ± 0.1	0.3 ± 0.1
^{197}Au	11.1	66	32	1438	23.1	25.8	3.8 ± 0.1	0.3 ± 0.1
^{197}Au	8.3	59	16	1250	22.5	26.1	3.8 ± 0.1	0.4 ± 0.1
^{197}Au	11.1	36	64	652	20.1	26.2	3.8 ± 0.1	0.4 ± 0.1
^{238}U	5.6	23	32	369	16.9	27.1	4.0 ± 0.1	0.5 ± 0.1
^{207}Pb	4.83	47	-	1000	22.3	27.6	3.9 ± 0.1	0.4 ± 0.1
^{238}U	5.6	38	16	826	22.7	32.5	4.0 ± 0.1	0.4 ± 0.1
^{238}U	8.3	72	-	1975	27.9	33.2	4.1 ± 0.1	0.3 ± 0.1
^{238}U	5.6	53	-	1333	25.8	33.8	4.1 ± 0.2	0.4 ± 0.1
^{238}U	8.3	57	16	1475	26.5	33.8	4.2 ± 0.2	0.4 ± 0.1

Table 4.1: Irradiation parameters including the initial beam energy and the energy after the ions passed through the Al degrader foil e.g. when entering the sample surface. The track radius and its polydispersity are deduced from fits to the SAXS data. The average dE/dx_e gives the mean energy loss over the length of the tracks.

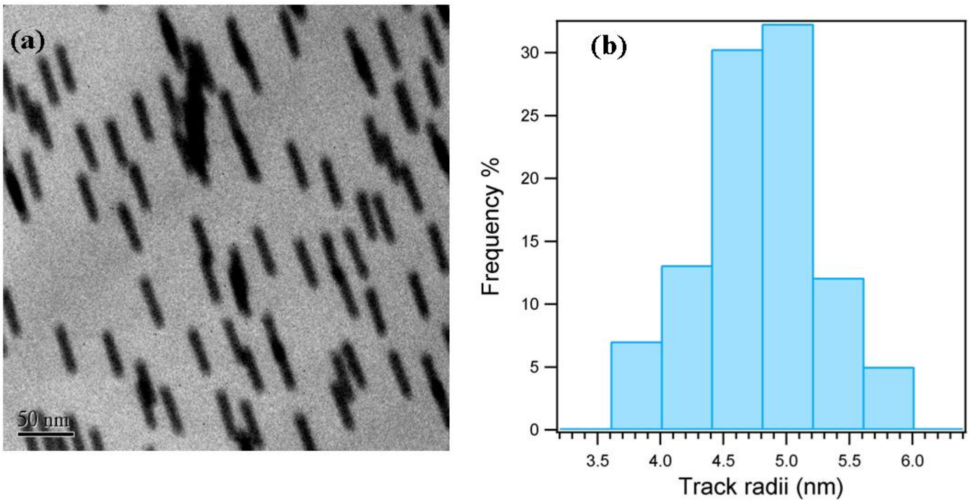

Figure 4.6: (a): plan-view TEM image of ion tracks in quartz generated with 1 GeV Pb ions at a fluence of 5×10^{10} ions/cm^2. The ion tracks were tilted with respect to the electron beam. (b) Histogram of the track size distribution from analyzing approximately one hundred tracks from TEM images. The measurement is based on the average value of track radii from FWHM and FWFM of the intensity cross sections.

choice of the appropriate measure is somewhat arbitrary, we chose the average between the FWHM and FWFM values. The mean value of track radii from these measurements is 4.8±0.5nm. It should be noted that high-resolution TEM images of track cross sections could improve the TEM measurement but the instability of quartz in the electron beam is problematic and tracks may change during observation.

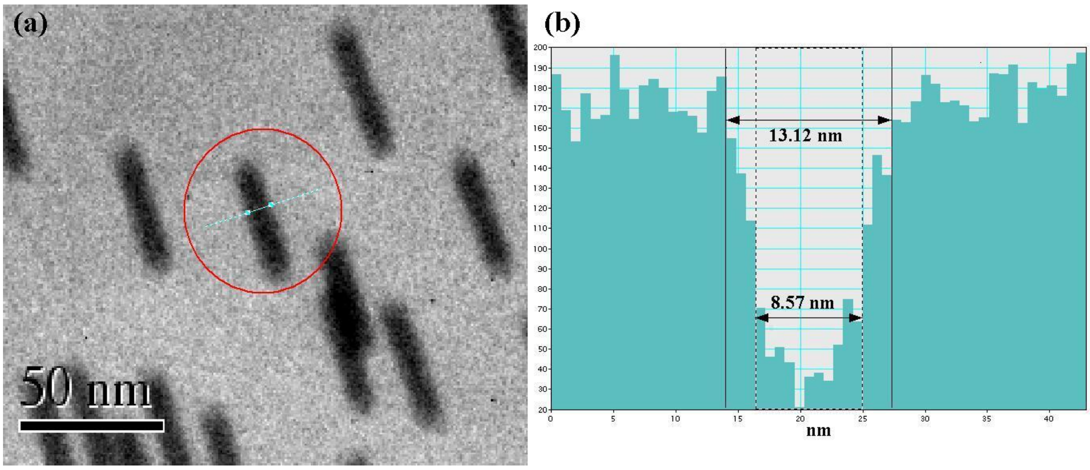

Figure 4.7: (a) A magnified in TEM image from ion tracks in quartz. The track in the circle is chosen for the demonstration of FWHM and FWFM measurements of the intensity cross section. (b) Plot of the intensity cross section showing the difference between the FWHM and FWFM of the ion track.

4.1.5 Molecular dynamic simulations

The formation of swift heavy ion tracks was simulated by our collaborators at the University of Helsinki using the classical molecular dynamics (MD) code PARCAS [173]. The atomic interactions were calculated with the Watanabe-Samela Si-O mixed system many-body potential [174, 175]. The electronic energy loss of the track producing ions is implemented by continuously following the evolution of the atomic lattice temperature as calculated with the inelastic Thermal Spike model (i-TS) [126] parameterized based on the RBS/C results from reference [48]. The energy transfer is applied between the electronic and the lattice subsystems of the i-TS by deposition of kinetic energy in a random direction to all of the atoms in the MD simulation cell. At each time step, the energy decreases radially with increasing distance from the track center until the two subsystems are in thermal equilibrium [47].

The formation of tracks was calculated for Au projectiles of three different stopping powers, viz. 9.9, 12.5, and 28.3 keV/nm, which are close to the average dE/dx_e for irradiation energies of 89, 185, and 2200 MeV. We emphasize that the kinetic energy is deposited to all atoms in the computation cell, even though the resulting damage is limited to few nanometres around the ion trajectory. The cell of the MD simulation consists of a 25 nm cube with periodic boundary conditions resulting in a system size of about 1.3 million atoms. The cell is created as a perfect crystalline α-quartz structure and is initially relaxed. The track area is surrounded by several nanometres of pristine material in the x- and y- directions, whereas in the z direction the track penetrates through the periodic cell, modeling an infinitely long, homogeneous track. The last 0.5 nm at the borders of the computation cell in the x- and y-directions is cooled by Berendsen temperature control [176] to approximate heat conduction further into the material. The initial temperature in the calculation is 300 K, a time step of about 0.4 fs is used, and simulations are continued for 200 ps until the cell density converges to the stable profiles.

Top-view images of the MD simulation cells are shown in figure 4.8 along with the relative radial density profiles originating in the center of the track [47]. For better visualisation of the MD density profiles obtained, smoothed profiles using a five point running average are also plotted. The track radii obtained by the MD simulations are shown on the density profiles as dashed lines and mark the boundary between disordered/amorphous and crystalline material.

(a) 89 MeV Au

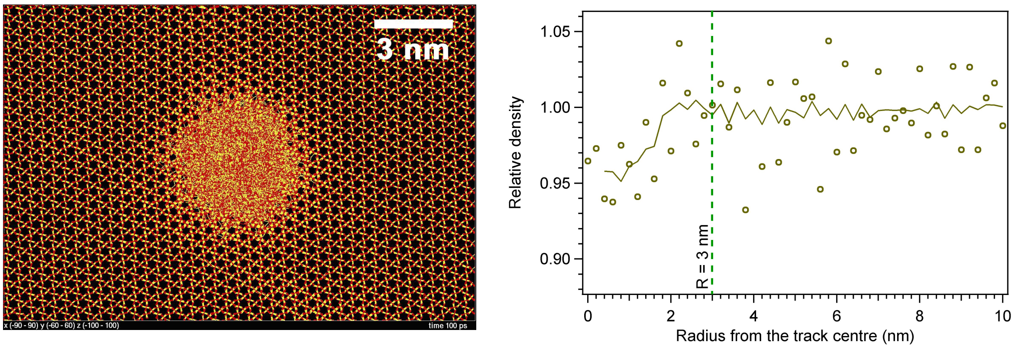

(b) 185 MeV Au

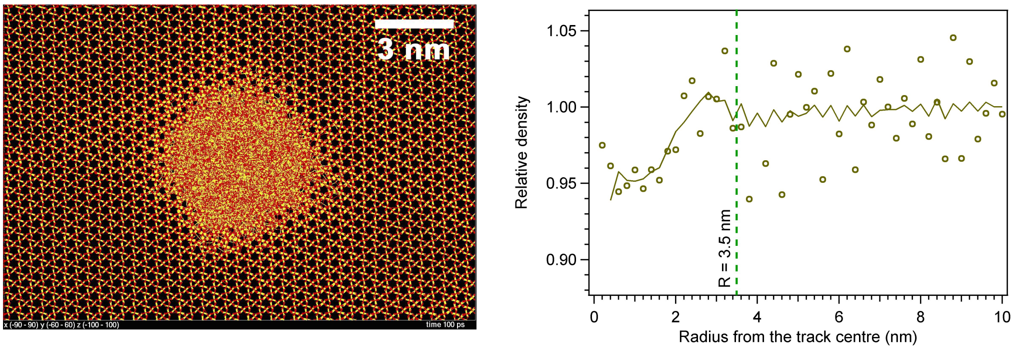

(c) 2.2 GeV Au

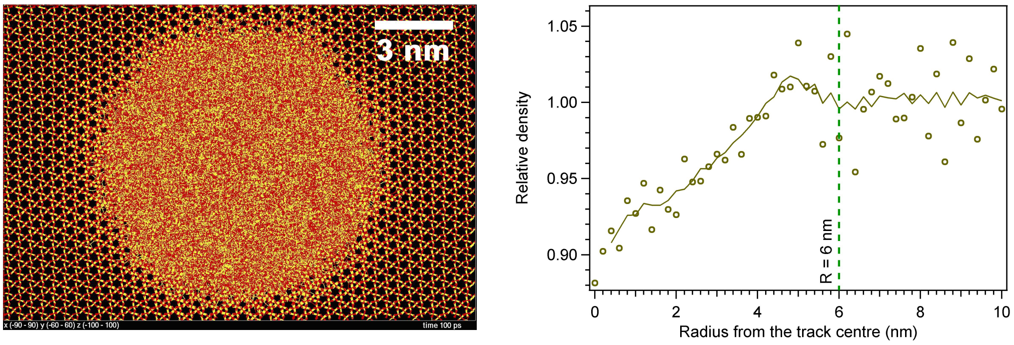

Figure 4.8: Left: atomistic images of MD simulated tracks in crystalline quartz (top view). Right: symbols give the corresponding atomic density as a function of the track radii. The solid lines are the smoothed density profiles using a five point running average. The dashed lines indicate the track radii deduced from the amorphous/crystalline interface.

As outlined above, the energy distribution that is taken as an input for the MD simulations was calculated using the i-TS model that is developed to describe how the energy deposited into the electronic system [80, 110, 89] is transferred to the lattice atoms via the electron-phonon coupling. This rapid heating can induce local melting or boiling. The track formation criteria is linked to the quenching of the molten phase leading to amorphization [48, 177]. Good agreement with the experimental track radii and sputtering rates are obtained using a fixed electron-phonon mean free path of 3.8 nm [89, 112].

MD simulation combined with the energy distribution predicted from the thermal spike model yield the atomistic structure of track embedded in crystalline quartz. It is evident that the MD simulations are also consistent with the formation of amorphous tracks.

4.1.6 Comparison of the SAXS measurements with previous results

Figure 4.9 compiles all SAXS and TEM track radii as a function of the electronic energy loss of the ions together with the data from the MD simulations [47], and experimental data from earlier studies using RBS/C [48, 160, 161] and TEM [48]. Track radii from the i-TS model as a function of the dE/dx_e are shown as solid and dashed lines for two different beam velocities corresponding to energies of 0.5 and 7.0 MeV/u. AFM data provided in the literature [52] measuring surface hillocks that occur due to relaxation and material expansion at the surface are not included as these cannot be compared with tracks surrounded by a matrix material measured by the other techniques.

In order to compare these results consistently, dE/dx_e was calculated for all data points using SRIM-2008 by taking into account the ion and energy of each irradiation condition. RBS/C measurements are based on the first 500 nm depth from the surface of the sample [48, 160, 161]. We calculated the corresponding mean dE/dx_e values which differ by up to 20% from the reported ones (calculated using the TRIM-91 [48, 161] and TRIM-95 [52] codes). Although the reported values for the track formation threshold in quartz vary based on the measurement technique, the effect of the different threshold values on the calculation of the average dE/dx_e is small (for example, for 1 GeV Pb ions the mean energy loss is 22.9 keV/nm using a threshold value of 6 keV/nm and 21.3 keV/nm using 1.8 keV/nm). Given an approximate 10% uncertainty of the SRIM calculations, the influence of the threshold value on the mean energy loss remains within the code precision. Due to its small effect [168], the velocity effect on the threshold was not considered when calculating the mean energy loss for our low energy beams (27, 89, and 185 MeV) experiments.

Results of SAXS and RBS measurements [48, 160] show reasonable agreement at energy losses below ~17 keV/nm. At higher energy losses, the radii measured by SAXS saturate at approximately 4 nm, while track radii determined from RBS measurements [48, 160] are consistently higher. While the uncertainties in the RBS/C data is significantly higher than those from the SAXS measurements, and modern Monte Carlo methods for RBS/C simulation may yield more accurate track radii, a clear trend of increasing track radii with the energy loss is apparent. It is worth noting that the RBS/C results in [161] show no obvious dependence on the energy loss, different to those in ref. [48, 160] however, only limited data with high uncertainties are presented in this study. The small dependence of the track radii measured by SAXS on the

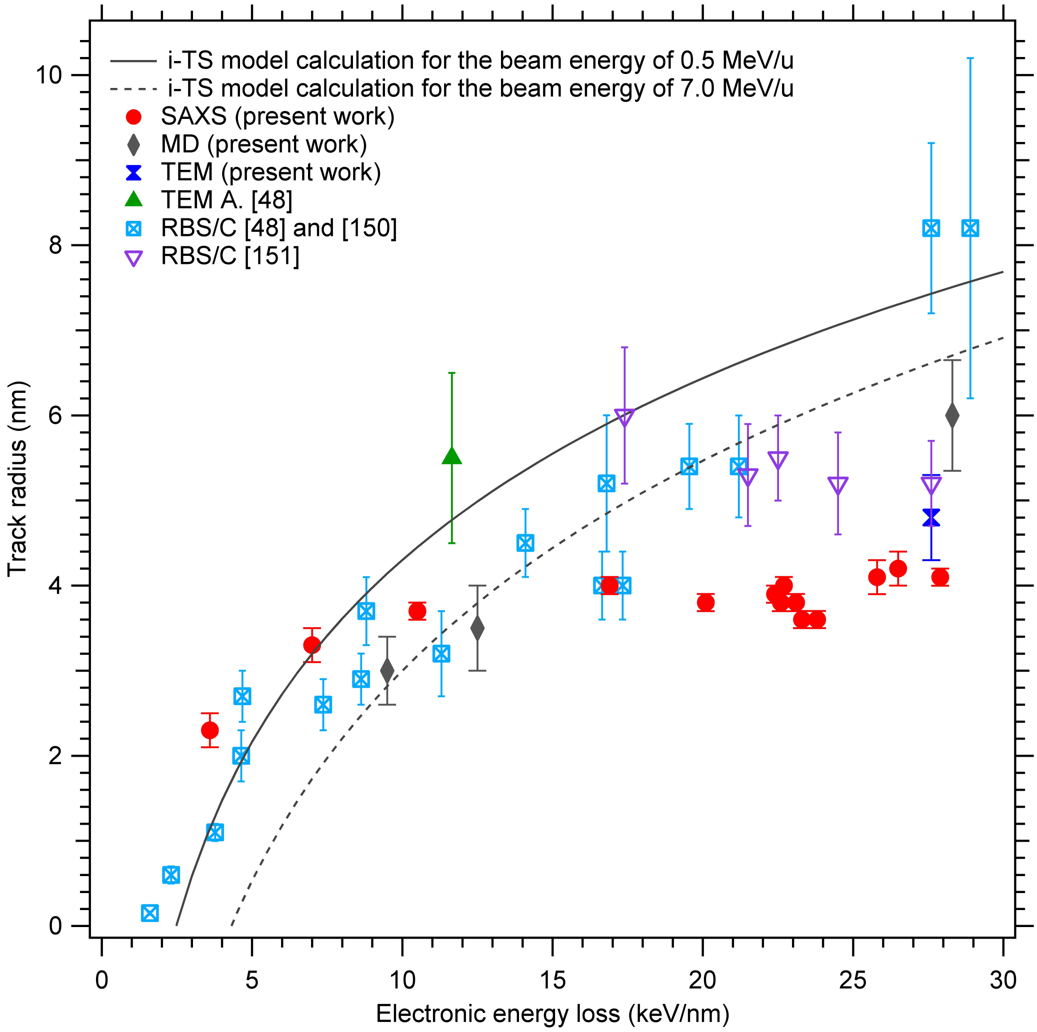

Figure 4.9: Track radii as a function of the electronic energy loss in α-quartz for different ion/energy combinations. The uncertainties of the SAXS data shown in the plot correspond to the fitted radius polydispersity.

electronic energy loss is somewhat surprising, as most insulators show a clear increase of the track radii with dE/dx_e [89]. An exception is mica, where a weak dependence of the track size on the electronic energy loss has been previously reported [178]. In this study [178] track radii measured with SAXS initially increases with the energy loss and at a certain value of the dE/dx_e, remains constant, similar to the change in the track radii in quartz. Calculations using the thermal spike model, which are based on the RBS/C results from reference [48], however, predict a steady increase in the track radius in quartz with increasing energy loss. At low energy losses, the radii extracted from MD simulations also agree well with the ones obtained from SAXS, however, at high dE/dx_e, MD results yield a larger value. This is not unexpected because MD simulations are based on the energy distribution predicted from the thermal spike model [47]. These observations indicate, that the simple model of melting and quenching, that underlies the thermal spike concept, may not be sufficient to explain track formation in quartz. High stresses and the role of point defect creation may have a significant influence on the resulting track morphology, which is not considered in the thermal spike calculation.

We now consider possible scenarios, why the radii in quartz deduced from SAXS observations are in agreement with RBS/C for electronic energy loss less than about 17 keV/nm and not for larger electronic energy losses.

A discrepancy between the RBS/C measurements and the SAXS results could originate from the existence of a defective halo around an amorphous track core. The defective halo will perturb channelling, leading to effectively larger track radii but may possess the density of crystalline quartz, thus inaccessible by the SAXS measurements. A defective halo has been previously studied in quartz [167] and $LiNbO_3$ [179, 180, 181] under high-energy ion irradiation. It is suggested that the radial morphology of tracks in insulators, produced with ions above the damage creation threshold [180], is typically characterized by a core, halo, and tail structure resulting from the concentration of defects above a certain threshold in the center of the track (amorphous core) surrounded by a damaged or preamorphised region (halo), followed by a less damaged tail region.

A defective halo could be the result of partial recrystallization of quartz during the quenching phase. The thermal spike model uses the radius of the molten cylinder as a criterion for the track size. During the rapid cooling, however, part of the molten material may recrystallise at the interface to the surrounding solid matrix, leading to a smaller radius of the residual amorphous phase. This has been observed experimentally and in MD simulations of ion tracks in complex oxides (pyrochlores) [182]. The recrystallization of the outer region of the molten track was shown to be imperfect, leaving a crystalline but defective halo around the amorphous core. In contrast to the MD simulations on complex oxides, our MD results on quartz do not indicate this recrystallization process is operative and thus we consider it unlikely.

A defective halo might also be an intrinsic feature of the ion track occurring during formation. It was suggested for the case of quartz [167] and $LiNbO_3$ [180, 181] that the amorphisation mechanism during track formation proceeds via point defect generation, similar to the case of ballistic collisions. In the area where the defect concentration exceeds a threshold value, the material collapses into an amorphous state, leaving a halo of defects around it where the threshold value is not exceeded. We note that for the ion tracks in quartz, it is predicted the halo area reduces by increasing the electronic energy loss above 4 keV/nm [167], however, the study only investigates energy losses of up to 10 keV/nm. The discrepancies between RBS/C and SAXS which are apparent at large energy losses and correspond to high ion velocities may result from the fact that at these energies the electron cascades rapidly dissipate energy through the crystal and result in a higher cooling rate of the material [183]. This process will leave behind more residual defects in the halo region, which would be observed in RBS/C. The existence of a halo may thus explain the differences of the RBS/C and SAXS data.

MD simulations also predict amorphisation of the ion track with good agreement of the track size at low energy loss ranges. The disagreement at high-energy losses could be an indication that the energy distribution provided by the thermal spike model and serving as an input for the MD calculations overestimates the temperature.

Alternatively, the typical melting criteria established for track formation within the thermal spike scenario can be discussed. A boiling phase during ion-track formation also offers a plausible explanation for the discrepancy of SAXS and RBS/C measurements, and i-TS calculations. According to i-TS model calculations, the melting is reached for Au ions of energy below 1 MeV/u ($dE/dx_e < 13.5$ keV/nm), and track radii observed by SAXS coincide well with the one deduced from RBS/C [48]. From reference [184], the appearance of the boiling phase can be associated with the appearance of a sputtering rate which is significant above 11 keV/ nm. Using this criterion it is suggested that the boiling phase is reached in the center of the tracks and may induce a pressure wave propagating radially from the center of the track. If this wave creates a shell of compact amorphous SiO_2 [63] with nearly the same electron density as crystalline SiO_2, SAXS would not identify this outer shell. Such a scenario is supported by the MD calculations which show an under dense area smaller than the amorphous track radius (see figure 4.8). For example, tracks induced by GeV Au projectiles have an under dense core of 4 nm radius with a denser but still amorphous shell of about 2 nm thickness. While the compacted amorphous shell cannot be identified by SAXS, RBS/C is sensitive to its structural disorder. An accurate TEM measurement that shows the possible amorphous core and amorphous shell zones could resolve the ambiguity of the explanation and rule out the structure of an amorphous core with a partially re-crystallized halo, but the uncertainty of TEM measurement in quartz is usually beyond the difference between the core and shell sizes. The large uncertainty may be due to artifacts, relaxation of the tracks in quartz or susceptibility of the damaged zone to the electron beam.

4.2 Apatite

Apatite refers to a group of mineral with the general chemical formula of $Ca_5(PO_4)_3X$ where X can be F (fluorapatite), OH (hydroxyapatite) or Cl (chlorapatite). The crystalline structure of apatite, shown schematically in figure 4.10, is composed of PO_4 tetrahedra surrounded by Ca atoms with ions located along the c axis. Fluorapatite has a hexagonal lattice structure of space group $P6_3/m$ while hydroxyapatite and chlorapatite can have either hexagonal or monoclinic structure depending on the nature of the order/disorder of $(OH)^-$ and $(Cl)^-$ ions along the c axis. Fluorapatite has a density of $\sim 3.15gr/cm^3$.

Apatites are widely distributed in igneous, sedimentary, and metamorphic rocks. They are also abundant in bones and teeth [185]. Fluorapatite and hydroxyapatite are two very important bioceramic crystals which are ceramics used for the repair and reconstruction of diseased or damaged parts of the musculo-skeletal system [186, 187]. For instance, hydroxyapatite is known to be an idealization of the primary constituent of the mineral portion of bones and teeth and it can be used for coating of porous implants to speed up the rate of bone formation in the pores [186]. In recent years there has been a great interest in using fluorapatite for environmental applications [188, 189, 190] and in nuclear waste disposal [191]. As mentioned in section 1.2 apatite is an important candidate for studying fission tracks due to its natural uranium content. Durango apatite from the Cerra de Mercado mine in Durango, Mexico is a widely accepted standard for fission-track dating [192] and represents ~70% of all the fission track age determinations [10].

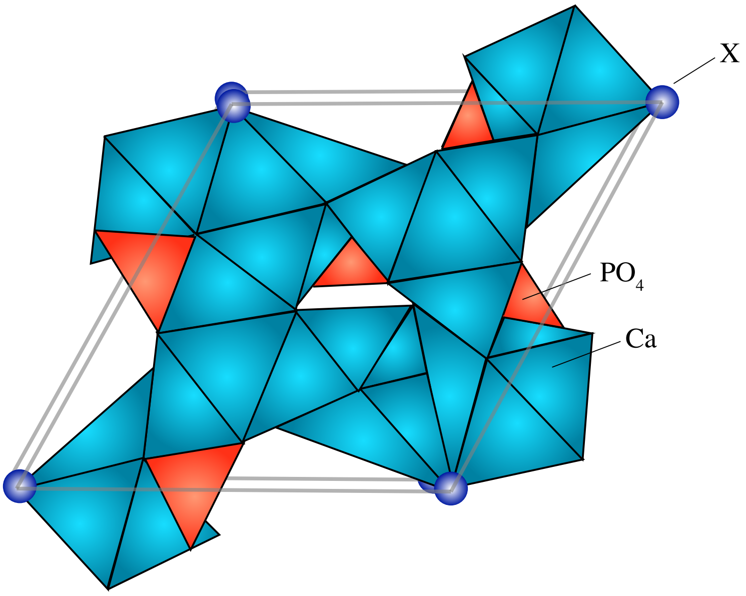

Figure 4.10: Crystal structure of apatite. Red represents the PO_4 tetrahedra and blue the Ca polyhedra. X can be F, OH, or Cl.

4.2.1 Ion tracks in apatite

Similar to ion tracks in quartz, in apatite the damage along the trajectory of a fission fragment has been considered to be cylindrical and amorphous [193, 11, 194]. Despite the important applications of fission tracks for thermochronology, systematic studies of the internal (un-etched) structure of tracks and their annealing behavior are rare. The present knowledge of the fission track dating process is largely based on empirical analysis of etched track-length-distributions as a function of temperature, time and composition. The understanding of the structure of un-etched fission tracks as a function of geologically relevant parameters may lead to better and more accurate interpretation of etched track distributions.

In recent years advanced high-resolution analytical techniques (e.g. HRTEM) were applied to study the internal structure of latent tracks in apatite [107, 43]. It was reported that the fission tracks in apatite are porous channels of very low atomic density in contrast to a previously assumed amorphous track [43]. The formation of the porous tracks were attributed to the irreversible decomposition of fluorapatite, and the sublimation of volatile elements along the fission track during the highly-ionizing energy deposition. In another study the entire length of an ion track in apatite is imaged using a novel sample preparation technique, together with advanced transmission electron microscopy [107]. The 8.1 μm long track generated with 80 MeV Xe ions in apatite was shown to have four zones of 1) a uniform track, e.g. little change in the track diameter with depth, 2) significant change of diameter with depth, 3) discontinuous track, and 4) no observable track along the ion trajectory (from the sample surface). Therefore, it was suggested that the tracks are initially continuous and parallel but at greater depths, besides the decrease in track diameter, the tracks gradually deviate from their trajectories as the ratio of nuclear to electronic stopping power increases, and the nuclear collision-induced track deflection gradually accumulates along the ion paths [107].

In this work, we have utilized SAXS to study ion tracks in Durango apatite including the same set of samples used for TEM investigations of reference [43] and performed both isochronal *ex situ* and isothermal *in situ* annealing experiments (the annealing studies are presented in the next chapter). It is demonstrated that SAXS is well suited for studying the damage morphology and annealing behavior of ion tracks in apatite and provides track radii with an accuracy of fractions of a nanometer [46]. However, we note that SAXS does not enable direct observation of individual tracks, it measures an average over a large ensemble of tracks generated under identical conditions.

4.2.2 Sample preparation

Crystalline samples of Durango apatite were first annealed in order to remove pre-existing fission tracks inside the mineral. Subsequently samples were mechanically polished to thicknesses of 30-50 μm and irradiated at the UNILAC accelerator at GSI using 2.2 GeV ^{197}Au ions, 2 GeV ^{238}U ions, 1.4 GeV ^{129}Xe ions, and 1.1 GeV ^{101}Ru ions to a fluence of 5×10^{10} ions/cm^2 and 0.64 GeV ^{58}Ni ions to a fluence of 2×10^{12} ions/cm^2. The range of all ions exceeds 60 μm as estimated by SRIM-2008, e.g., the ion tracks extend through the entire thickness of the samples with approximately uniform electronic energy loss. The applied ion fluences were sufficiently low to yield well separated aligned tracks. Irradiations with 100 MeV ^{127}I and 185 MeV ^{197}Au ions were performed at the ANU Heavy Ion Accelerator Facility on 110 μm and 40-50 μm thick Durango apatite, respectively. The irradiation fluence for the I ions was 5×10^{10} ions/cm^2 and for the Au ions ranged between 5×10^{10} and 1×10^{12} ions/cm^2. The projected ranges for both ions were smaller than the sample thickness. All irradiations were performed at room temperature under normal incidence. Details of the irradiation parameters are given in table 4.2, where the values for the surface electronic energy loss dE/dx, and the ion range were calculated using SRIM-2008.

Ion	Ion energy (MeV)	Sample thickness (μm)	Fluence (ions/cm^2)	Surface dE/dx_e (keV/nm)	Projected range (μm)	Track radius (nm)	Polydispersity of track radius (nm)
^{127}I	100	110	5×10^{10}	15.9	11	4.6±0.1	0.4±0.3
^{197}Au	185	40-50	5×10^{10}- 1×10^{12}	23.4	15	5.5±0.1	0.5±0.2
^{58}Ni	644	30	2×10^{12}	6.3	83	1.8±0.1	0.3±0.1
^{101}Ru	1121	30	5×10^{10}	13.5	76	2.9±0.1	0.2±0.1
^{129}Xe	1432	40	5×10^{10}	18.6	75	3.6±0.1	0.3±0.1
^{238}U	2047	50	5×10^{10}	37.5	66	5.5±0.1	0.3±0.1
^{197}Au	2187	30	5×10^{10}	27.3	85	4.8±0.1	0.2±0.1

Table 4.2: Irradiation parameters and track radii extracted from SAXS measurements of ion tracks in apatite.

4.2.3 SAXS measurement of ion tracks in Durango apatite

Similar to the SAXS measurements of ion tracks in quartz (section 4.1.3), in apatite, tracks were first aligned parallel to the X-ray beam and then tilted by angles of 2°, 5°, and 10°. Figures 4.11 (a) and (b) show an isotropic and anisotropic SAXS image of ion tracks in apatite, respectively. The sample was irradiated with 2.2 GeV Au ions to a fluence of 5×10^{10} ions/cm^2. The strong oscillations in the anisotropic image which indicate monodisperse track radii and a sharp transition of the density from tracks to the matrix material.

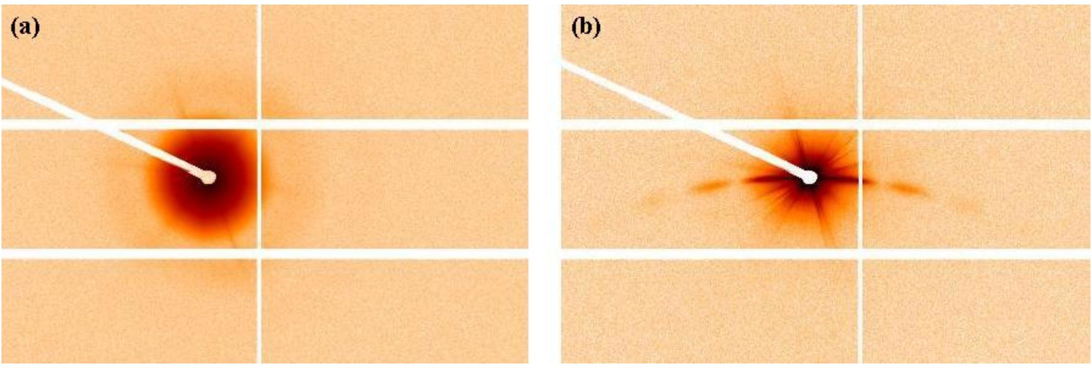

Figure 4.11: Scattering images of an apatite sample irradiated with 2.2 GeV Au ions (a) with the X-ray beam parallel to the ion tracks, (b) with the tracks tilted by ∼ 10°.

SAXS spectra were obtained by masking the streaks of the anisotropic images and subtracting the background scattering as outlined in chapter 3. The scattering intensities are plotted as a function of the scattering vector q in figure 4.12 (symbols) for different irradiation conditions. The model that best fits the SAXS spectra for all irradiation conditions is the hard cylinder model explained in sections 3.4.6 and 4.1.3. It is worth noting that alternative models were tested for fitting the scattering intensities such as the soft cylinder and the core-shell models (described in section 3.4.6); however, the hard cylinder model gives a superior fit in particular at both ends of the q range. When the core-shell model was applied for example, the extracted shell radii were smaller than the uncertainty of the core radii and therefore negligible (the core radii were in agreement with the radius obtained from the hard cylinder model). Using the soft cylinder model, the fitted parameter that indicates the smoothness of the transition between the core and the shell was close to a sharp transition. Fits to the hard cylinder model are shown as solid lines in figure 4.12.

The fitted track radii as a function of the surface electronic energy loss, dE/dx_e are plotted in figure 4.13 (a) for the different ion/energy combinations and listed in table 4.2. The plot also shows the track radius measured with TEM which will be discussed later. The track radii increase with increasing energy loss, in agreement with observations in other materials [89]. The increase of the track radii with dE/dx_e is almost linear up to ∼26 keV/nm whereafter the trend is flattened out. The track radius in apatite from irradiation with 100 MeV I and 185 MeV are approximately 1 nm larger than that expected from interpolation of the higher energy irradiation experiments. This effect reflects the so called “velocity effect” [89]. Figure 4.13 (b) shows the energy loss of Au ions in apatite as a function of the ion energy calculated

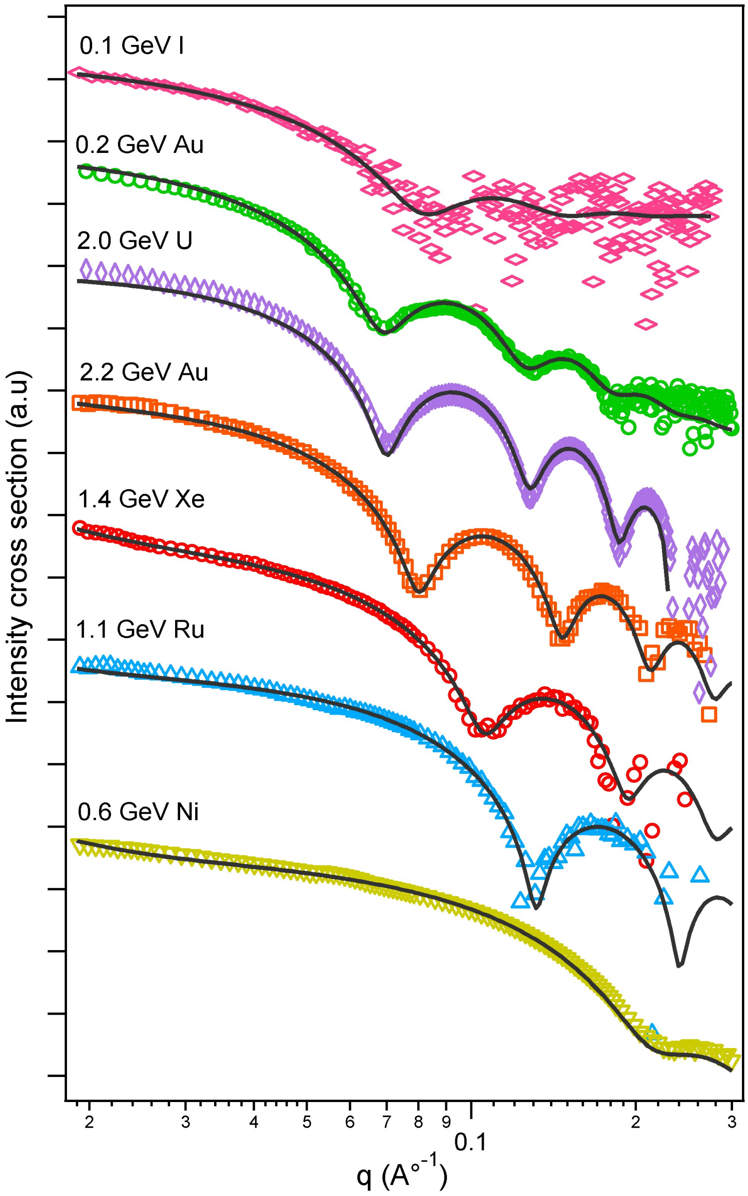

Figure 4.12: Scattering intensities of ion tracks as a function of the scattering vector q extracted from the anisotropic scattering images after background removal. The solid lines show the fits to the cylinder model with sharp boundaries.

by SRIM-2008. 185 MeV and 2.2 GeV Au ions yield a similar energy loss on either sides of the Bragg peak, the maximum of electronic energy loss, but the value is reached at a different projectile velocity. For higher velocities, the projectile-induced electron cascade has a larger extension and thus lower energy density. Tracks produced at lower ion velocities thus generally have larger radii. The larger track radius for 100 MeV I and 185 MeV Au ions are in agreement with the velocity effect. It also should be noted that the velocity of 100 MeV I and 185 MeV Au ions are closer to the typical velocity of fission fragments that cause track formation used for geo- and thermo-chronology.

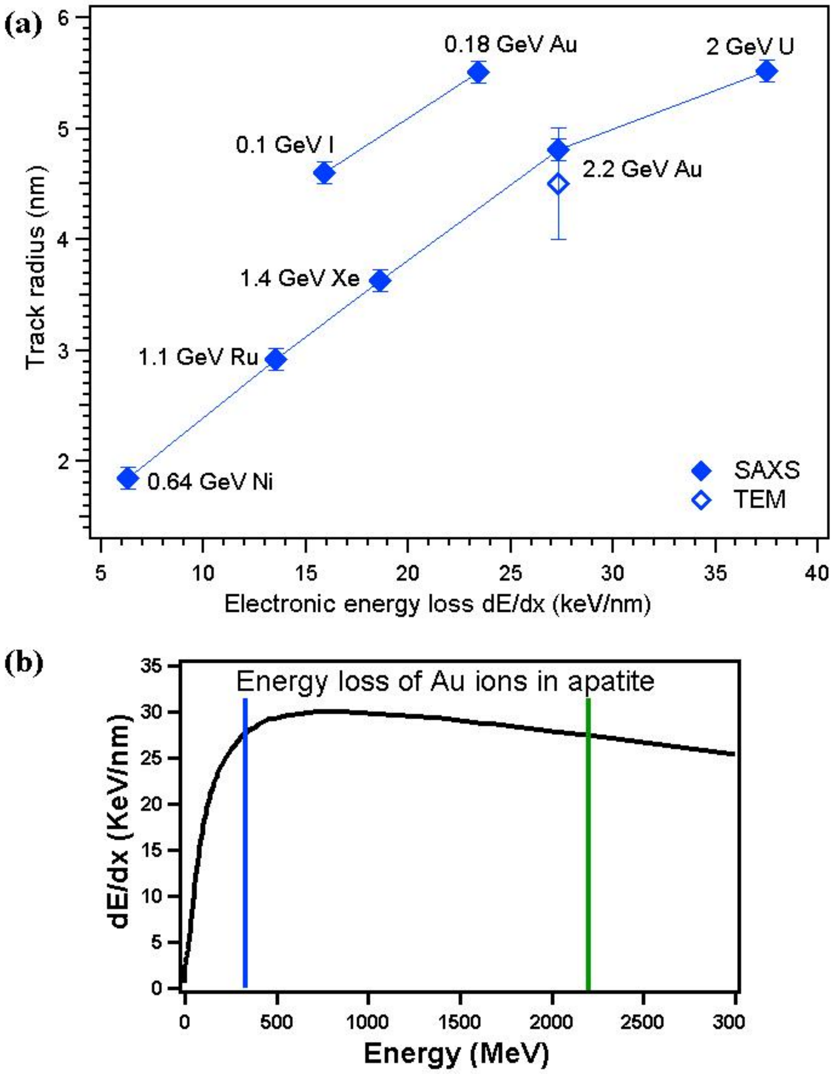

Figure 4.13: (a) Extracted track radii as a function of the electronic energy loss for different ion/energy combinations; the solid line is to guide the eye. (b) Electronic energy loss of Au ions as a function of ion energy in apatite calculated with SRIM-2008. The vertical lines indicate two different energies on either sides of the Bragg peak which result in the same amount of dE/dx_e.

The wide dE/dx_e range spanned by the utilized ion projectiles encompasses the range produced by the relevant fission fragments (typically between Xe and Kr of ~1 MeV per nucleon energy with an average dE/dx_e of about 16 keV/nm) thus allowing direct conclusions from artificial to natural track properties [1].

The utilized fitting model is consistent with the formation of amorphous tracks, which are likely to be characterized by rather abrupt, approximately cylindrical crystalline/amorphous interfaces. Indeed, macroscopic methods such as Rutherford backscattering spectroscopy in channeling configuration and X-ray diffraction have previously indicated amorphization of apatite materials by swift heavy ion irradiation above a threshold value dE/dx_e of approximately 5 keV/nm [195]. The formation of amorphous tracks is known for numerous insulators and selected semiconductors and can be explained by a rapid quench of the material from the molten phase. As explained earlier the thermal spike leads to highly-localized heating around the ion trajectory that may exceed the melting temperature of the material [89].

Figures 4.14 (a) and (b) show cross-sectional TEM image of an apatite sample irradiated with 2.2 GeV Au ions and a corresponding high-resolution plan-view TEM image of the cross section of a single track, respectively. The TEM analysis was performed by our collaborators at the University of Michigan. In figure 4.14 (a) the typical long columnar structure of the ion tracks embedded in the crystalline matrix is apparent. The track radius of 4.5±0.5 nm is in excellent agreement with that extracted from the SAXS measurements (plotted in figure 4.13 (a)), thereby confirming the validity of our model assumption as previously detailed. During TEM imaging, however, prolonged high-current density electron irradiation can lead to an enhanced recrystallization of amorphous apatite or even bubble formation [196, 197]. Furthermore, when using thin film samples as required for TEM, results can be influenced by the existing proximity of the two surfaces which can be sinks or sources for point defects. On the other hand, SAXS does not require elaborate sample preparation and yields superior statistics by measuring the bulk properties of a large ($\sim 10^6$) ensemble of ion tracks. To verify that the X-rays do not induce any measurable changes to the ion tracks we have continually exposed an apatite sample to X-rays for 2 h recording SAXS patterns at regular time intervals. No measurable changes were observed in the scattering intensities as shown in figure 4.15. We note that the usual exposure time to obtain a SAXS measurement is between 2 and 10 s.

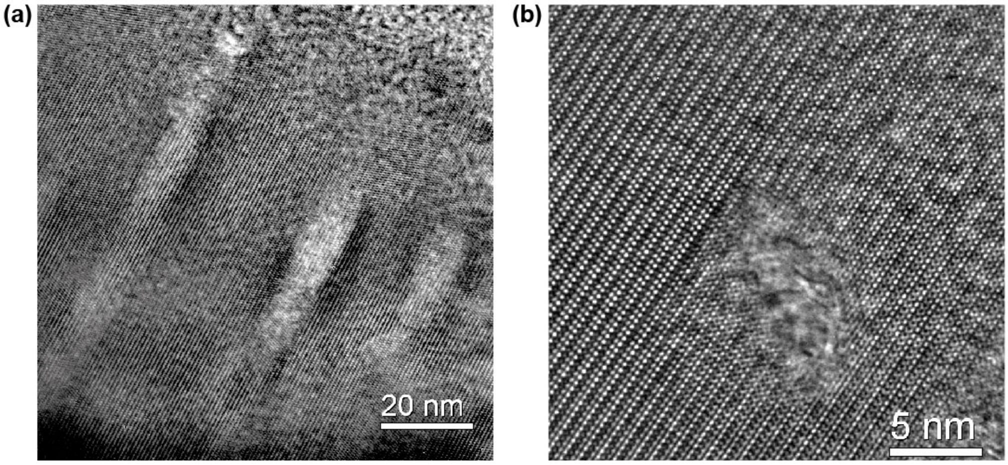

Figure 4.14: Transmission electron microscopy images of apatite irradiated with 2.2 GeV Au ions. (a) Cross-sectional image showing the long columnar structure of the ion tracks. (b) A plan-view high-resolution image of the track cross section which is slightly tilted with respect to the track axis. Both images are taken by Dr. Jiaming Zhang at the University of Michigan.

Figure 4.16 presents the scattering spectra from ion tracks in apatite irradiated

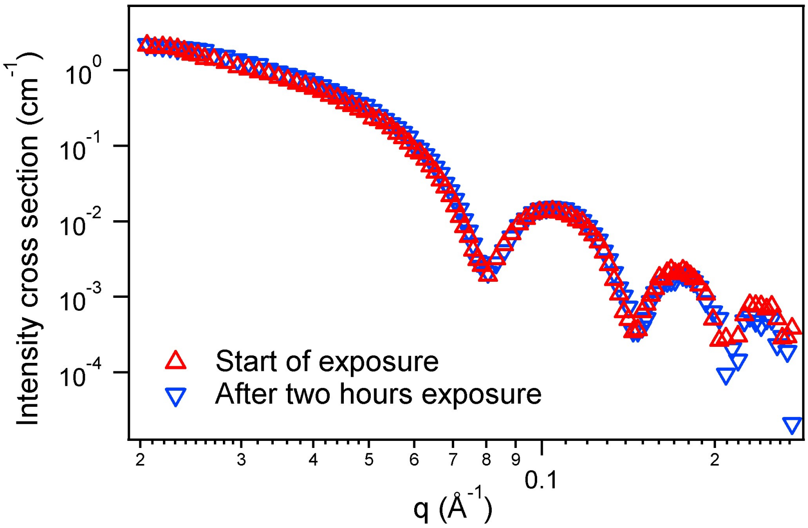

Figure 4.15: SAXS spectra of ion tracks in apatite after 2 hours exposure to the X-ray beam.

with 185 MeV Au ions after background removal for different irradiation fluences along with their corresponding fits to the hard cylinder model. The scattering intensities are normalized to the length of the track and approximately scale with the ion fluence or equivalently the number of tracks generated in the samples. This is an indication that ion track overlap effects are negligible. The extracted track radii for the fluences of 0.5, 1, and 10 $\times 10^{11}$ ions/cm^2 are 5.5±0.1, 5.5±0.1, and 5.5±0.1 nm, respectively. We can estimate the amount of track overlap using an overlap model explained in section 4.1.3. With a fluence of 5×10^{10} ions/cm^2, which is mostly used for our irradiation experiments, the amount of track overlap is less than 1% of the irradiated area for all track radii extracted from the SAXS measurements indicating largely isolated tracks. In apatite irradiated with 185 MeV, a track radius of ~5.5 nm yields ~20% track overlap at a fluence of 1×10^{12} ions/cm^2 which becomes apparent as an attenuation of the oscillations in the scattering spectra, yet track radii can still be reliably fitted.

Absolute calibration of the scattering intensities enables an estimate of the density change within the ion tracks of approximately 1±0.5% as compared with crystalline material for all irradiation parameters, a value typical for amorphous materials. Using SAXS it is not possible to indicate a positive or negative change in the density of the tracks compared to the matrix, however, previous investigations on apatite materials clearly show a decreased density of amorphous material with respect to the crystalline phase [196]. Molecular dynamics simulations of ion tracks in fluorapatite also suggest a similar magnitude [194]. More recently, HRTEM measurements of ion tracks in Durango apatite irradiated with 2.2 GeV Au reported porous tracks with no solid components in the track core [43]. This obvious discrepancy between the density change measured with SAXS and TEM may be explained by outgasing of volatile components in the track core during TEM preparation or imaging. We note that hollow tracks would lead to substantial material errosion at high irradiation fluences. This was not observed by us or others even when tracks were studied in apatite with fluences in the ranges of 10^{12} and 10^{13} ions/cm^2 [198, 199]. Finally, as will be discussed in the next chapter, annealing of the ion tracks in apatite results in

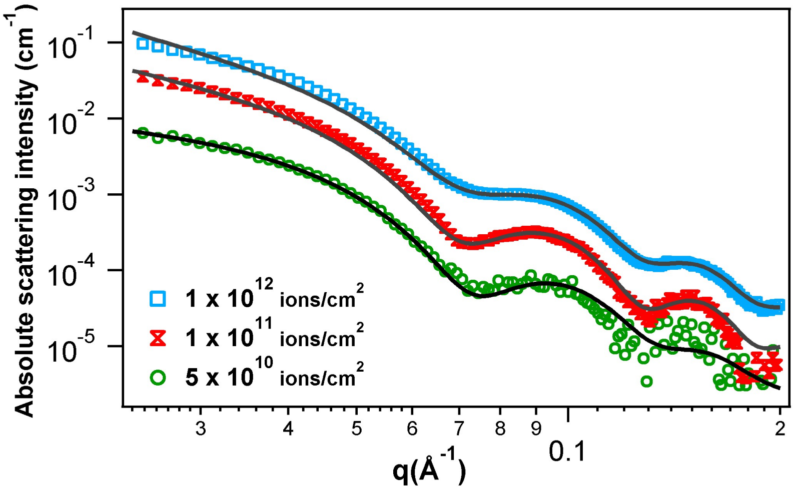

Figure 4.16: Absolute scattering intensities from ion tracks in apatite samples irradiated with 185 MeV Au ions after background removal as a function of scattering vector q. The solid lines are the corresponding fits to the hard cylinder model.

recrystallisation of the tracks. If tracks were hollow, it appears unlikely that the material can fully recover from the irradiation damage.

4.3 Olivine

Olivine is a major rock-forming mineral in the oceanic crust and basaltic rocks and the most common mineral in the Earth's mantle. Olivine is the general name for a range of minerals with the formula $(Mg, Fe)_2SiO_4$ with names forsterite and fayalite referring to magnesium-rich (Mg_2SiO_4) and iron-rich (Fe_2SiO_4) compositions of the mineral, respectively. As shown in figure 4.17, the olivine structure consists of isolated $(SiO_4)^{4-}$ tetrahedral pointing alternately up and down along rows parallel to the c axis. Mg^{2+} and Fe^{2+} cations appear in two distinct octahedral sites: a distorted M1 site and a more regular M2 site [151]. Layers occur parallel to the (100) plane with edge-sharing octahedra cross-linked by isolated $(SiO_4)^{4-}$ tetrahedra [200].

Surfaces of airless bodies including Moon, Mercury, and asteroids are subject to physical and chemical alterations due to bombardment by ions from the solar wind, magnetosphere ions, energetic electrons, cosmic rays, ultraviolet photons and fast interplanetary dust (micrometeorites). This process which is called space weathering [201, 202] can lead to molecular bond breaking and change the elemental composition via ion implantation and preferential sputtering. In some cases these alterations can be studied on returned samples of lunar soil [203] and interplanetary dust [204]. Olivine which is a common mineral in many asteroids has been shown to be susceptible to space weathering [205, 206] and therefore it is an important material for investigating the effects of space weathering. In particular San Carlos olivine (95% Mg_2SiO_4) is extensively used as a standard for the measurement of high temperature physical properties of the earth's upper mantle [207].

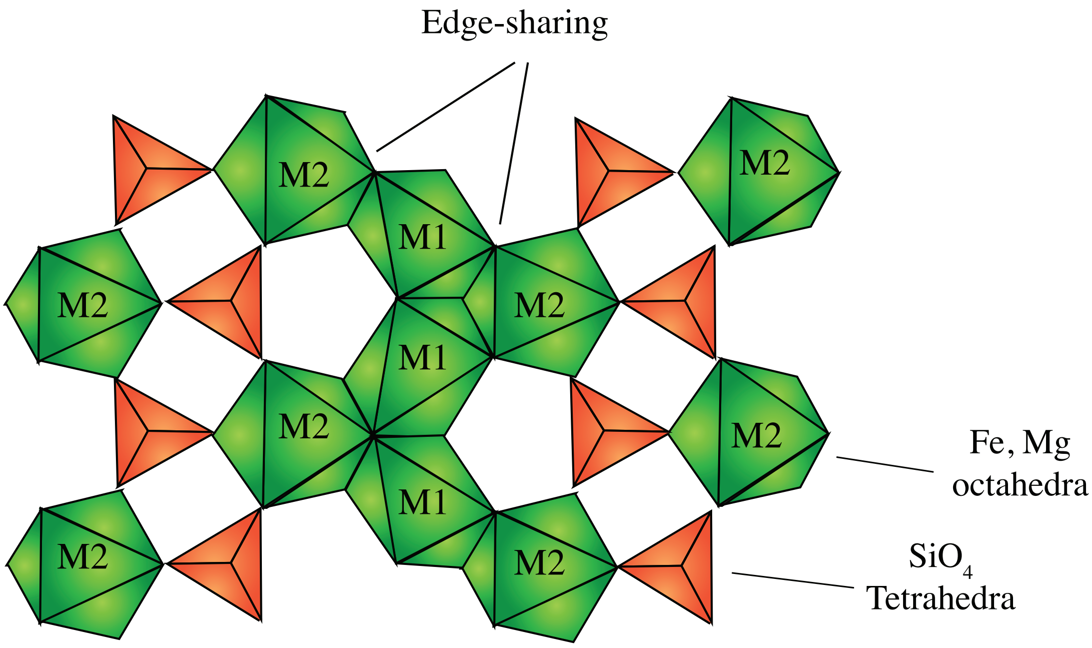

Figure 4.17: Crystal structure of olivine projected on the bc plane. M1 and M2 are the octahedral sites occupied by Mg^{2+} and Fe^{2+} cations without any preference.

4.3.1 Ion tracks in olivine

It has been long known that cosmic radiation primarily consists of energetic nuclei with atomic numbers ranging from 1 to at least 26. However, studies of fossil particle tracks in meteorite crystals indicated the existence of extremely heavy cosmic rays [208]. Detailed studies of abundances of individual nuclei will add valuable information to our knowledge of heavy cosmic rays and help determining the charge of the track-forming nuclei [209, 37]. Some meteoritic minerals such as olivine are more resistant to ionizing radiation and their track formation threshold might only be overcome by particles significantly heavier than Ar ions. This low sensitivity means that the mineral is not completely covered with ion tracks, but instead it has only recorded tracks of specific cosmic rays.

Similar to apatite, ion tracks in olivine have been studied predominantly by means of chemical etching [37, 210] which requires precise calibration of the etching mechanism and the results can be affected by the etching conditions [37]. Etching removes the material inside the ion tracks as well as inside other local damaged zones that may exist in the mineral, therefore dislocation zones and other defects can look like nuclear tracks. Moreover, images of etched tracks do not always provide good visualisation of the original track. In olivine, the etching of the ion tracks in the crystal is very anisotropic and it can produce a broad surface pit with a narrow tail. In some cases tracks in olivine showed up as elongated slits [211, 212].

Because of the importance of detection of heavy and super heavy nuclei of cosmic rays for modern nuclear physics and astrophysics [213] and limitations of conventional methods for studying ion tracks in meteoritic minerals, investigating latent (un-etched) tracks in olivine is of great interest.

4.3.2 Sample preparation

Crystalline samples of San Carlos olivine were initially annealed in order to remove naturally occurring tracks. Samples were then mechanically polished to approximately 40 μm and irradiated at the UNILAC accelerator at GSI using 2.2 GeV ^{197}Au ions, 2.6 GeV ^{238}U ions, and 1.1 GeV ^{101}Ru ions to a fluence of 5×10^{10} ions/cm^2 and 0.64 GeV ^{58}Ni ions to a fluence of 2×10^{11} ions/cm^2. The projected ranges of the ions estimated by SRIM-2008 were greater than 80 μm which means the ion tracks extended through the entire sample thickness. Table 4.3 lists details of the irradiation parameters.

Ion	Ion energy (MeV)	Sample thickness (μm)	Fluence (ions/cm^2)	Surface dE/dx_e (keV/nm)	Projected range (μm)	Track radius (nm)	Polydispersity of track radius (nm)
^{58}Ni	644	40	2×10^{11}	6	88	1.8±0.2	0.5±0.2
^{101}Ru	1121	40	5×10^{10}	13	81	2.7±0.1	0.4±0.1
^{197}Au	2187	40	5×10^{10}	26.2	90	4.6±0.1	0.3±0.1
^{238}U	2642	40	5×10^{10}	34.4	87	5.3±0.1	0.4±0.1

Table 4.3: Irradiation parameters and track radii extracted from SAXS measurements of ion tracks in olivine.

4.3.3 SAXS measurement of ion tracks in San Carlos olivine

As explained earlier in sections 4.1.3 and 4.2.3, SAXS measurements of ion tracks in San Carlos olivine are conducted by first aligning the tracks parallel to the X-ray beam and then tilting them in different angles in order to obtain the anisotropic SAXS images of ion tracks which are used for extracting the scattering intensities. Figure 4.18 shows SAXS images of ion tracks in olivine generated with 2.2 GeV Au ions to a fluence of 5×10^{10} ions/cm^2. Comparing with figure 4.11 which shows scattering from ion tracks in apatite irradiated under the same conditions, it is evident that the scattering signals from tracks in the both minerals are very similar and strong oscillations infer largely monodisperse radii and sharp transitions between the track densities and the surrounding matrix material.

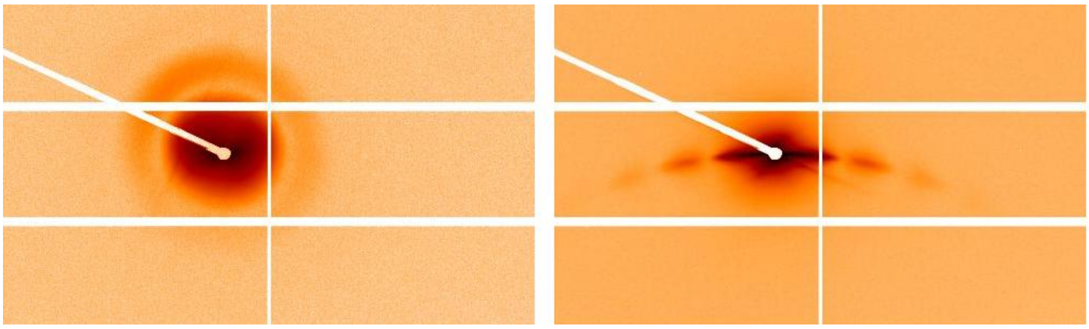

Figure 4.18: Scattering images of an olivine sample irradiated with 2.2 GeV Au ions (a) with the X-ray beam parallel to the ion tracks, (b) with the tracks tilted by ∼10°.

Scattering intensities extracted from the streaks for olivine samples irradiated with different ion/energy combinations are plotted in figure 4.19. Solid lines show the fits using the hard-cylinder model and as apparent, the model provides excellent fits to the experimental data for all irradiation conditions. This model was previously used to fit the scattering intensity from ion tracks in quartz and in Durango apatite (sections 4.1.3 and 4.2.3).

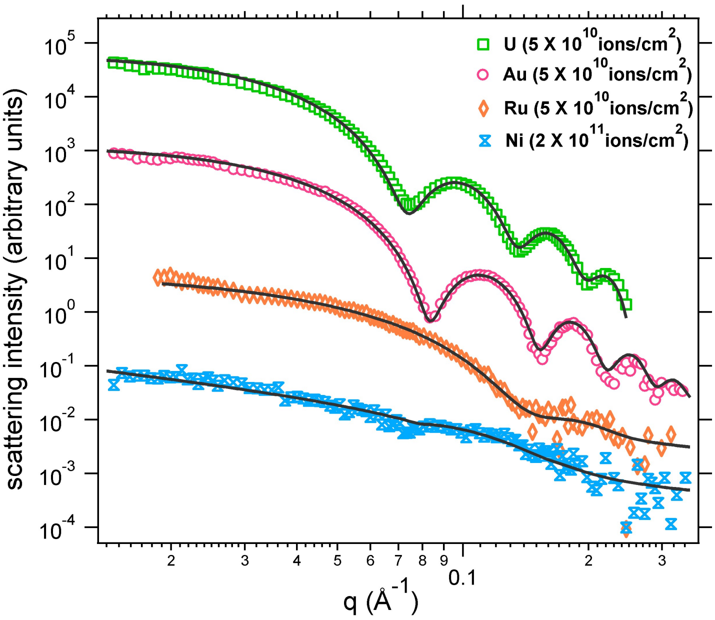

Figure 4.19: SAXS scattering intensity from ion tracks in olivine (symbols) and corresponding fits with the hard cylinder model (solid lines) for different irradiation conditions.

The applicability of the model assuming a constant density in the ion tracks with sharp boundaries to the matrix material is consistent with the formation of amorphous tracks in both materials [214, 9]. The track radii are plotted as a function of the electronic energy loss in figure 4.20. Track radii in apatite extracted from SAXS measurement are also plotted in the figure as a comparison. In olivine, the polydispersity of the track radius or equivalently the width of the Gaussian distribution amounts to approximately 10% of the radius or less for most irradiation conditions. The values for dE/dx_e were calculated using SRIM-2008 and represent the surface energy loss of the ion. The results are also listed in table 4.3. The track radii in olivine increase almost linearly with increasing dE/dx_e up to about 26 keV/nm and flattens afterward. This trend as well as the magnitude of the track radii are very similar to those observed for ion tracks in apatite. As the tracks are generated closer to the track formation threshold, the weaker oscillations in the SAXS spectra apparent in figure 4.19 can possibly result from a less homogeneous energy dissipation along the ion trajectory and resulting fluctuations in the track radial density.

Absolute calibration of the scattering intensities enables an estimation of the density change within the ion tracks in olivine to be about 1±0.7% as compared with the crystalline matrix. This value is similar to the density change observed in apatite [46]. In

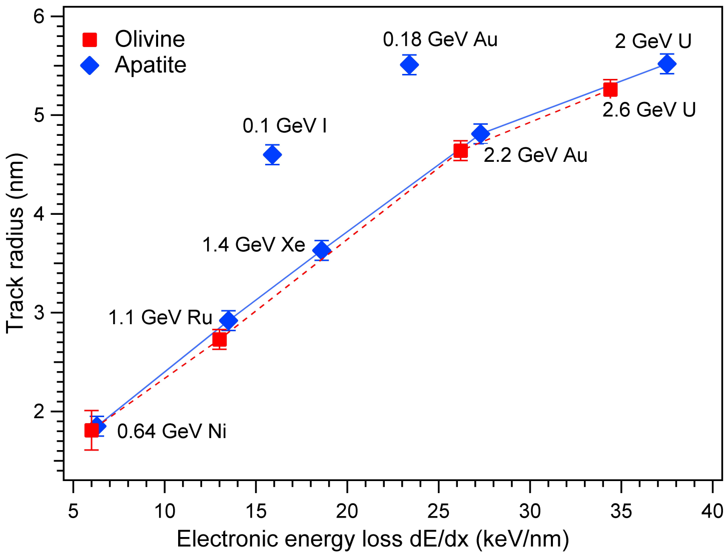

Figure 4.20: Track radii in olivine as a function of the electronic energy loss for different irradiation conditions; the solid line is to guide the eye. Track radii in apatite extracted from SAXS measurement are also plotted as a comparison.

the next chapter, where the annealing behaviour of ion tracks in apatite and olivine is studied, we will see that despite the very similar density change and track radii at room temperature, ion tracks in the two minerals behave very differently when annealed at elevated temperatures.

4.4 Conclusions

In summary, swift heavy ion induced tracks were studied by means of synchrotron based small-angle X-ray scattering in synthetic quartz, Durango apatite and San Carlos olivine. The track morphology in quartz is consistent with amorphous cylinders surrounded by a stressed, possibly defective crystal matrix. At high dE/dx_e, the SAXS track radius saturates at a value of approximately 4 nm in contrast with MD simulations and predictions from a thermal spike model. The weak dependence of the track radius on the electronic energy loss indicates that track formation is probably a more complex process than a simple melt and quench predicted by the thermal spike model. Alternative explanations include the presence of a defective halo, which indicates track formation proceeds via point defect generation, and/or the presence of a boiling phase during track formation. The observed density change of $\sim$2% in the amorphous core (with respect to the matrix) is consistent with observations from macroscopic swelling measurement for low fluences but is significantly lower than the $\sim$15% density difference between bulk silica and quartz, leading to high stresses in the material.

In apatite and olivine, SAXS measurements revealed very similar track radii for a variety of irradiation conditions and results are consistent with the formation of amorphous ion tracks in both minerals. Track radii increase by increasing the electronic energy loss and the trend is almost linear up to about 26 keV/nm and flattens for higher dE/dx_e.

Different ion velocities with similar energy loss yielded significantly different track radii in apatite consistent with the velocity effect. The measured ∼1% electron density change of tracks with respect to the matrix in both minerals is consistent with amorphous materials.

While SAXS can not provide visual images of individual tracks inside the material and it requires modeling of the data for extracting the track properties, it is capable of determining properties such as radii of latent ion tracks with great precision and statistics. This nondestructive technique simultaneously measures large ensembles of tracks and allows for the measurement of bulk samples along with short acquisitions time facilitated by high flux synchrotron radiation. It is well suited for studying ion tracks in a variety of materials.

Chapter 5

Annealing behavior of ion tracks

5.1 Introduction

Several factors have been identified to cause damage recovery of ion tracks and affect their long-term stability including heat, chemical environment, and pressure [123, 215, 216]. Among these, the most important factor for the minerals commonly used in geological applications is heat.

Ion-track annealing has been studied in a variety of minerals and insulators by means of chemical etching [64, 217, 162, 164]. In these studies the mean fission track length and number density of the spontaneous fission tracks are used for calculating the annealing/recrystallisation rates of the tracks. In general the fission track length distribution exhibits properties indicative of the nature of the thermal history experienced [23] and the present knowledge of the annealing process is limited to empirical fits to data of etched track lengths as a function of temperature, time, and composition [10, 64, 218]. The empirical analysis can not reflect the correlation between the internal (un-etched) structure and the annealing behavior as the etching removes some of the essential information [64]. There are only few investigations of the annealing behavior during heating of latent ion tracks by TEM [219, 220, 14, 18] where the tracks were observed in very thin layers of the samples or in grains of the crushed material.

We have combined synchrotron based small-angle X-ray scattering with *in situ* and *ex situ* annealing to study the effect of heating on ion tracks in three crystalline materials: synthetic quartz, Durango apatite and San Carlos olivine. Our first annealing experiments were conducted on ion tracks in apatite. Isochronal annealing was performed *ex situ* using a conventional furnace. After each annealing step, a SAXS measurement was performed. This experiment provided some insight into the feasibility of measuring the annealing behavior of ion tracks using SAXS and calculating an activation energy for the damage recovery. To study track annealing as a function of time, we initially performed *in situ* annealing experiments using a heat gun which was placed underneath the samples while the SAXS measurements were performed. Isothermal annealing of ion tracks in apatite and olivine samples was conducted in this way. For later experiments we utilised a commercial heating stage discussed in section 3.4.5, which enabled *in situ* annealing experiments with well defined temperature/time profiles. Annealing of ion tracks in quartz samples were performed using this heating stage. The different experimental designs for the annealing experiments in apatite and quartz led to calculating the relevant activation energies of the damage recovery in two different ways, e.g. using the cross-cut method [221, 222] for quartz and an empirical formula [223] based on an Arrhenius equation for apatite.

To keep this chapter consistent with the previous one, the sequence of the results is not chronological and starts with the ion-track annealing in quartz.

5.2 Annealing of ion tracks in quartz

Studies of ion tracks in natural quartz are often conducted due to their applications in geochronology and fission track dating [155]. In synthetic quartz the stability of ion tracks under high temperature conditions is important as the material is used for electronic instruments and solid state track detectors [224, 33, 225].

In the low ion irradiation energy regime with predominant nuclear stopping, it has been shown by means of RBS/C, that ion irradiation of quartz causes three-dimensional nucleation and growth of defect agglomerates which can lead to formation of a continuous amorphous layer at the depth of maximum energy deposition. This layer extends into greater depths by continuing ion bombardment [226]. In a different RBS/C study, the epitaxial regrowth of an amorphous layer generated with 175 keV Rb ion implantations has been reported to occur in a two stage recrystallisation process [227]. The observed planar movement of the crystalline/amorphous interface towards the surface which starts at 1073 K is consistent with epitaxial recrystallization of the amorphous layer. Complete recrystallization was achieved at 1173 K [227]. The observed activation energies for this process are 0.6±0.1 and 3.6±0.4 eV below and above 1070 K, respectively [227].

Annealing of radiation damage was also studied for amorphization as a result of fast neutron irradiation, where several natural quartz samples were annealed at elevated temperatures up to 1200 °C [228]. The effect of annealing was studied by different techniques including floating the samples in a liquid mixture with the same density as the sample and measuring the change in the density of the samples, the linear expansion upon annealing and the change in the refractive index [228]. An observed peculiarity in the annealing of the irradiation damage from fast neutrons was referred to as “anti-annealing”: an alteration toward the properties of disordered material at lower temperatures (∼350 °C) and toward that of quartz at higher temperatures (∼500 °C) [228]. This behavior was explained by the low stability of the SiO_2 lattice and small movements of the $Si-O_4$ tetrahedral with respect to each other [228]. The same study suggests a broad activation-energy spectrum for annealing of the disorder in quartz as the material anneals over a broad range of temperatures [228].

In the regime of high-energy ion irradiation, the interior of the damage track has been shown to be completely disordered and presumably amorphous [48]. In previous annealing studies of swift heavy ion induced tracks, chemical etching was used to measure the etched track length and estimate the track retention or registration efficiency ratio between annealed and unannealed samples [162, 229, 163, 164]. In natural quartz, by using isochronal annealing data for tracks generated with ^{252}Cf fission fragments, and applying an Arrhenius type equation, an activation energy of 3.83 eV for track annealing is reported [162]. Using a modified form of the equation for relating the track retention rate with the activation energy, a value of 2.11 eV is reported [163] for annealing of tracks in natural quartz generated with ∼2.8 GeV ^{208}Pb ions. Both studies have assumed a single recrystallisation process. In some studies track annealing was studied for tracks generated with respect to specific crystallographic orientations [229, 164]. In natural quartz it was shown that different crystallographic planes have different track registration properties and it was concluded that a particular plane might be exceptionally highly heat-resistant [229]. In synthetic quartz annealing of ion tracks induced with respect to the crystallographic orientation of the samples indicated that tracks parallel to the z axis of the crystal are more resistant to heat and therefore z-cut quartz is a better track detector at high temperatures than x- and y-cut quartz [164]. The reported activation energies which are based on chemical etching experiments may not be identical to the activation energies for track damage recovery but reflect more the specific experiment and the method of data evaluation [230]. A fundamental understanding of the annealing processes involved in the recovery of damage tracks requires consistent microstructural description of the temperature dependent track properties prior to chemical etching.

In this work we have studied the annealing behavior of swift heavy ion tracks in synthetic quartz. Two different experiments focus on the low temperature range, e.g. between room temperature and 620 °C where track expansion/relaxation and the elastic properties of the material inside the track and the matrix are responsible for a change in the track radius, and the high temperature range (above 620 °C up to 1070 °C) where the annealing results in track damage recovery.

5.2.1 Experimental

Single crystalline wafers of synthetic α-quartz with a thickness of 360 μm were irradiated with 2.0 GeV ^{238}U ions to fluences of 0.5, 1, and 3 $\times 10^{11}$ ions/cm^2 at the UNILAC accelerator at GSI. In order to vary the energy loss of the ions, degrader foils of aluminum with a thickness of 16 μm were placed in front of some of the samples. For samples covered with the foil, the energy of the ion impinging on the sample was reduced to 1.5 GeV. All irradiations were performed at normal incidence and room temperature.

After irradiation, samples were mechanically polished from the backside using a tripod method. Samples irradiated with 0.5 and 1×10^{11} ions/cm^2 were thinned down to a thickness between 50 and 90 μm while samples irradiated with 3×10^{11} ions/cm^2 were polished to approximately 240 μm as stresses in the latter samples led to fracturing of the samples during polishing.

Transmission SAXS was conducted at the SAXS/WAXS beam line of the Australian Synchrotron with an X-ray energy of 12 keV and a camera length of approximately 1600 mm. *In situ* annealing of ion tracks was performed using a LINKAM TS1500 heating stage. The stage was placed in front of the X-ray beam and SAXS measurements were taken periodically with 2 and 5 s exposure times followed by approximately 40 s of delay during the annealing. The track radii were studied over a temperature range between room temperature and 1070 °C by isochronal and isothermal annealing experiments. Details on the temperature profiles of each experiment are given in the relevant section (sections 5.2.2 and 5.2.3).

5.2.2 Elastic properties of ion tracks in quartz

To study the temperature dependence of the ion-track morphology in quartz, we have performed *in situ* annealing on samples irradiated with 2.0 GeV ^{238}U ions to fluences of 0.5, 1, and 3 $\times 10^{11}$ ions/cm^2. A first set of samples was annealed between room temperature and 620 °C with a temperature profile illustrated in figure 5.1. The ramping rate between different temperature steps was 130 °C/min and the sample was kept at each temperature for 5 min. After 5 min at 620 °C, the sample was cooled down to 50 °C and kept at this temperature for 15 min. This cycle of annealing was repeated for a second time (for some samples also for a third time).

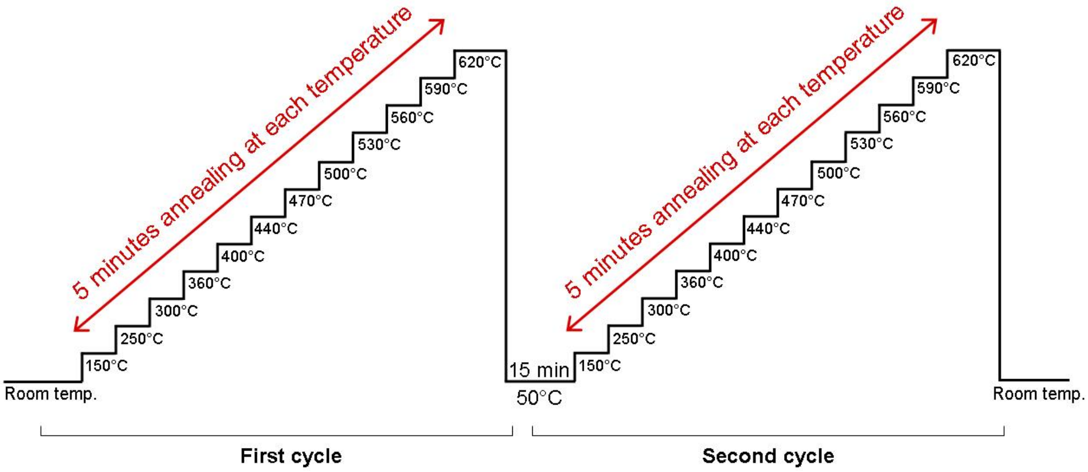

Figure 5.1: Temperature profile for annealing of ion tracks between room temperature and 620 °C. After the last annealing step in the first cycle, ion tracks are cooled down to 50 °C (close to room temperature) and then annealed in a second cycle with the same temperature steps.

Figure 5.2 shows scattering intensities from ion tracks generated by 2.0 GeV U ions with a fluence of 1×10^{11} ions/cm^2 at selected temperatures during the first and second annealing cycles at the end of the 5 min annealing step. The SAXS spectrum of ion tracks at 50 °C after the second cycle is also shown. While qualitatively the shape of the scattering intensities does not change, e.g. no deviation from the cylindrical track shape is apparent, a shift in the minima is an indication of a change in the track radii. The solid lines in figure 5.2 show the fits using the hard cylinder model discussed in sections 3.4.6 and 4.1.3. We have also applied other models such as soft cylinder and core-shell and the best model that can describe the data for all annealing temperatures is the hard cylinder model.

Figure 5.3 shows the extracted track radii as a function of the annealing temperature during (a) the first and (b) the second annealing cycle (symbols). The track radius for each temperature corresponds to the radius after 5 min annealing. In the first cycle the evolution of the track radius below 570 °C is characterised by an initial increase followed by a sharp decrease. Upon returning to room temperature ($\sim$50 °C), before the second cycle starts, the radius is significantly larger as compared to the room temperature value in the first cycle, indicating an irreversible expansion of the ion track. However, above approximately 400 °C, the track radii decreases with temperature, similar to the first cycle. When a third annealing cycle was applied, the track radii were found to be the same as those in the second cycle, indicating a reversible process. The inset in figure 5.3 shows the change in the track radii as a function of time during the 5 min annealing at 250 °C. Even though the total change during this time is very small, it is evident that the change is not "instant" but proceeds on a time scale of minutes. The data point corresponding to the track radius after 5 min annealing at 250 °C is circled.

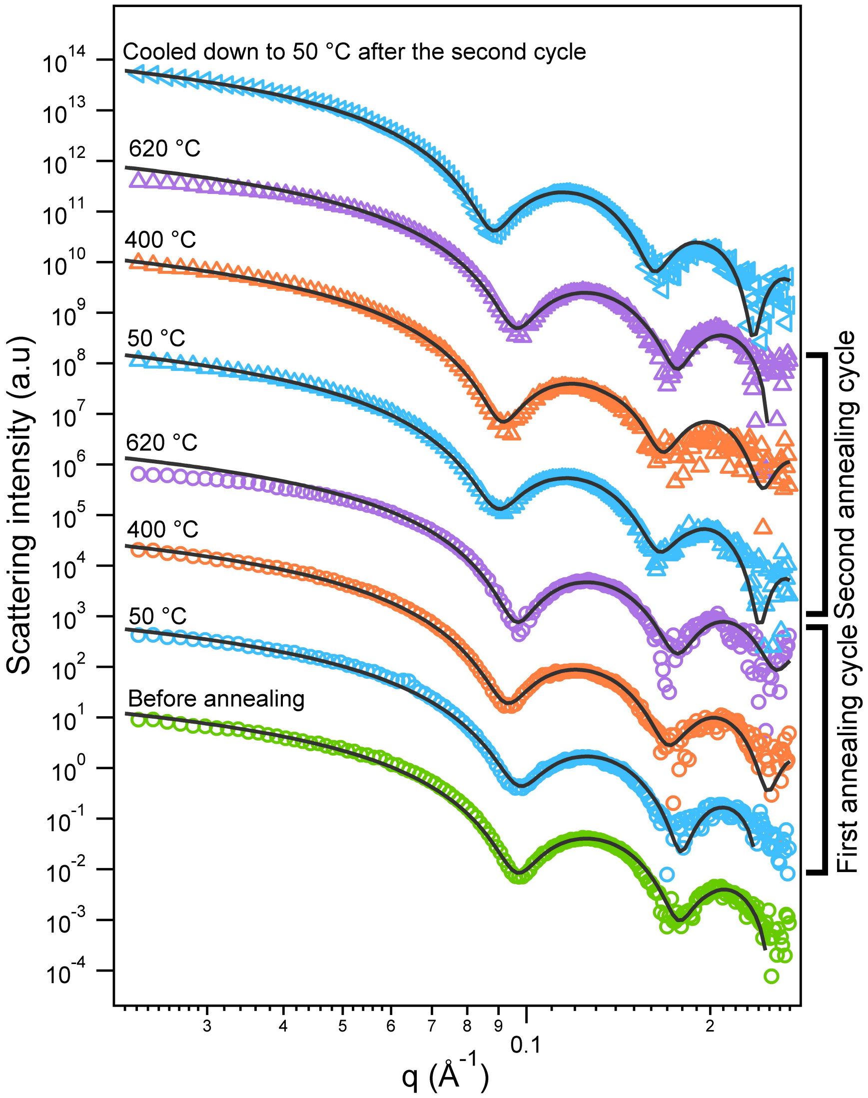

Figure 5.2: Selected SAXS spectra from ion tracks at room temperature and at different annealing temperatures between 50 and 620 °C. The solid lines are the fits to the hard cylinder model. Tracks were generated by 2.0 GeV U ions to a fluence of $1{\times}10^{11}$ ions/cm^2.

In order to assess if pre-annealing causes any relaxation of the tracks and changes the evolution of the ion track radii during the annealing cycles, a second sample with the same irradiation condition (2.0 GeV U ions with a fluence of $1{\times}10^{11}$ ions/cm^2) was pre-annealed at 400 °C for 20 min and then cooled down to 50 °C, where it was exposed to the same annealing cycle as the first sample. The evolution of the track radii in the second sample is shown in figure 5.4 for the pre-annealing stage, the two annealing cycles and upon returning to room temperature. As evident from plot (b), the pre-annealing stage resulted in a larger track radius at the beginning of the first annealing cycle. Thus, annealing of the tracks up to 400 °C can also cause an irreversible expansion of the ion tracks. Above 400 °C, the decrease in the track radius with temperature is similar to the first sample. Moreover, for both samples the change in the track radii during the second

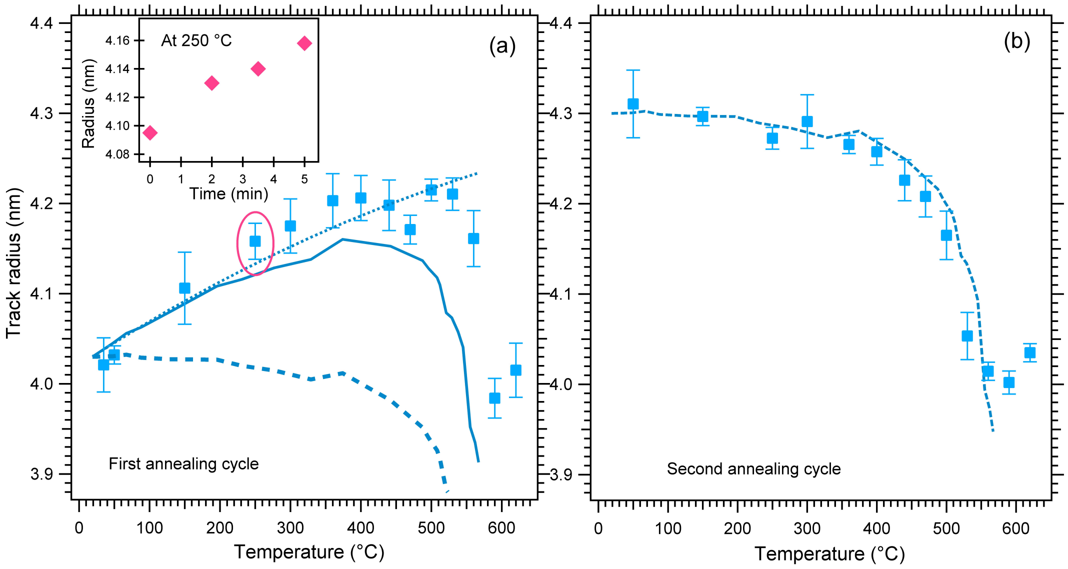

Figure 5.3: Ion track radii in quartz as a function of the annealing temperature in the (a) first and (b) second annealing cycles between room temperature and 620 °C. The track radius for each temperature corresponds to the radius after 5 min annealing. In (a): the solid line shows a model calculation of a track as an elastic cylindrical inclusion with the temperature dependent elastic constants of amorphous silica and quartz for the track and matrix material, respectively. The dashed line shows the calculation when only the elastic constants of the matrix are temperature dependent, and the dotted line is the model calculation when only elastic constants of the track are temperature dependent. The inset shows the change in the track radii during the 5 min annealing at 250 °C as a function of time. The data point corresponding to the track radii after 5 min annealing at 250 °C is circled. In (b), the dashed line shows a modified model calculation with an initial constant pressure on the track.

cycles are similar. Plot (d) in figure 5.4 shows that after the second cycle, the track radius returns to its value at the beginning of the second cycle.

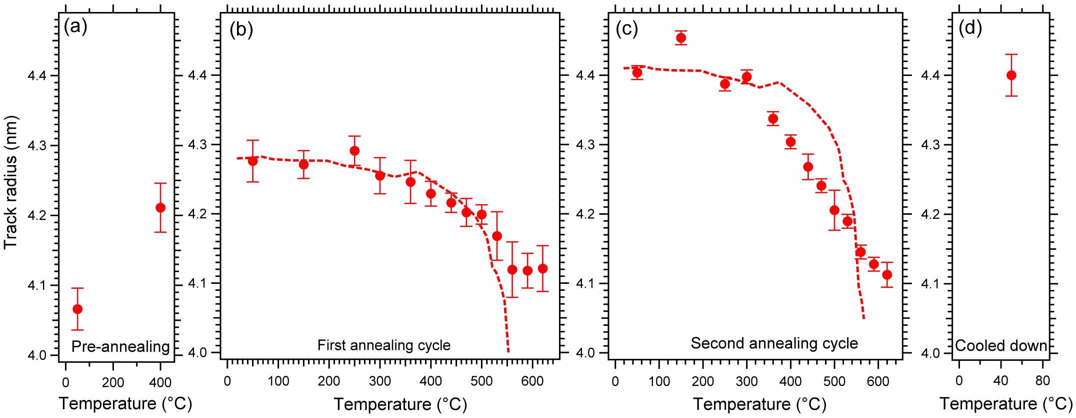

Figure 5.4: Ion track radii in quartz as a function of the annealing temperature. The sample was (a) initially annealed at 400 °C for 20 min and cooled down to 50 °C before being annealed up to 620 °C during a (b) first and (c) second annealing cycle. After the second cycle, the sample was (d) cooled down to room temperature. The dashed lines show the model calculation.

In order to investigate the effect of the irradiation fluence on the annealing behavior of the tracks, we have studied the change in the track radius for three quartz samples irradiated with 2.0 GeV ^{238}U ions to fluences of 0.5, 1, and 3 $\times 10^{11}$ ions/cm^2 in similar annealing cycles as explained earlier. The extracted track radii are plotted as a function of the annealing temperature in figure 5.5. Annealing of the samples started without any pre-annealing and samples were annealed over two (1 $\times 10^{11}$ ions/cm^2) or three (0.5, and 3 $\times 10^{11}$ ions/cm^2) cycles. It is apparent that the difference in the fluence or equivalently the number density of the tracks has no considerable effect on the on the temperature evolution of ion track radii with temperature. Moreover, regardless of the annealing history of the tracks, the second and any further annealing cycles result in a similar change in the track radii.

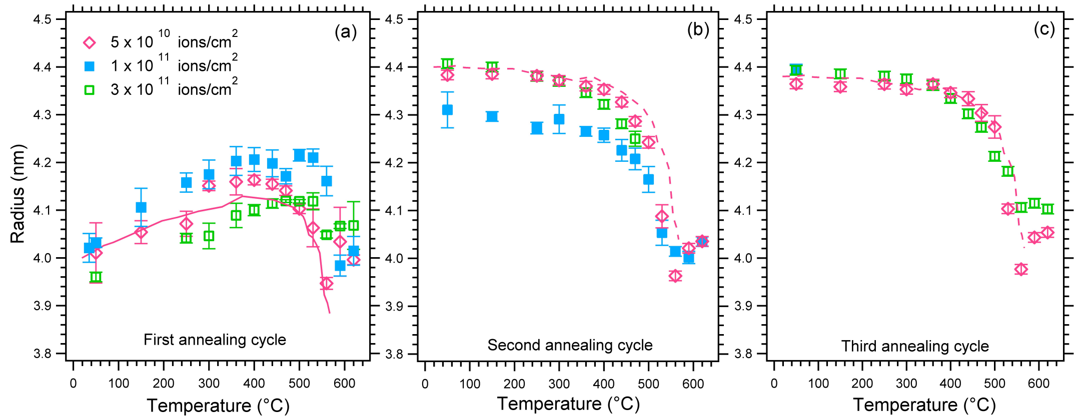

Figure 5.5: Evolution of the track radii in quartz as a function of the annealing temperature for three different fluences. The sample irradiated with a fluence of 1 $\times 10^{11}$ ions/cm^2 is annealed only over two cycles. The lines are the model calculations for the sample with a fluence of 5 $\times 10^{10}$ ions/cm^2.

In the following, we will suggest an explanation for the observed peculiar annealing behavior of ion tracks in quartz using the temperature dependent elastic constants of amorphous silica ($a - SiO_2$) and quartz ($c - SiO_2$). We assume that tracks in quartz consist of amorphous SiO_2 which is consistent with our previous observations described in section 4.1.3 and other studies. Both silica and quartz are known to show an unusual dependence of the elastic properties with temperature. Silica becomes elastically harder from room temperature up to about 1100 °C [231, 232]. Quartz, on the other hand, becomes elastically softer, and its aggregate Poisson's ratio changes rapidly and becomes negative close to the β-quartz transition temperature (~573 °C) [233].

To understand how the elastic constants affect the track radius, we use classical elasticity theory [234, 235], approximating an ion track as an infinitely long cylindrical elastic inclusion in an infinite elastic medium. This approximation is justified for the low fluence irradiation under investigation, where the distance between tracks is large compared to the track radius. For isotropic linear elastic materials, with a volume mismatch and different elastic constants in the cylinder and surrounding medium, the static elastic behavior of this system has an exact analytical solution [236, 237]. The radial strain ε^t_{rr} of the material in the track (relative to the equilibrium size of the same material at zero pressure) can be written as [237]:

$$\varepsilon^t_{rr} \quad = \quad -\frac{1}{E^t}[1-\nu^t-2(\nu^t)^2]P-\nu^t\varepsilon \tag{5.1}$$

where the contact pressure P is given by

$$P \quad = \quad -\varepsilon\frac{1+\nu^t}{\frac{1+\nu^m}{E^m}+\frac{1-\nu^t-2(\nu^t)^2}{E^t}} \tag{5.2}$$

Here E is the Young's modulus and ν the Poisson's ratio. The superscripts t and m denote the properties of the amorphous track and the crystalline matrix, respectively. ε is the relative linear size mismatch between the track and matrix material in their equilibrium states. This can be determined from the difference in the densities of the matrix and track material, which we have measured to be approximately 2% (see section 4.1.3). Using the density $\rho^m = 2.641\ g/cm^3$ for α-quartz [233], and considering that the linear size is proportional to $\rho^{-1/3}$, we obtain $\varepsilon = (2.588/2.641)^{-1/3} = 1.007$. We note that the exact value for ε is not crucial and values calculated from density differences between 0 and 15%, the latter corresponding to the density difference between bulk fused silica and quartz, have only an insignificant effect on the results. To determine the temperature dependence of the track radius, we use experimental values for the temperature dependence of the elastic constants of fused silica [231] and quartz [233]. For silica we used a parabolic fit to the data reported in reference [231] to obtain E^t and ν^t. The selection of Young's modulus for quartz is somewhat ambiguous, since a crystalline material does not have a single value for Young's modulus [234]. We used the shear modulus C_{S1} for directions perpendicular to the c axis. The elastic constants used are shown in figure 5.6. Other moduli [233], that are comparable in magnitude to macroscopically reported Young's moduli for commercial quartz [238] (~70 GPa), gave similar results. For ν^m we used the aggregate Poisson's ratio ν^* [233].

The radial strain ε^t_{rr} can be calculated from the temperature dependent elastic behavior using equation 5.1. Using the track radius R_0 and strain $\varepsilon^t_{rr}(T_0)$ at room temperature, the temperature dependent track radius is given by:

$$R(T) \quad = \quad R_0\frac{(1-\varepsilon^t_{rr}(T))}{(1-\varepsilon^t_{rr}(T_0))} \tag{5.3}$$

The calculations using this model are shown in figures 5.3 (a) and 5.5 (a) as solid lines. To understand this behavior we performed the calculations by keeping the E and ν, constant to the room temperature values for either silica or quartz. Results of these calculations are shown in figure 5.3 as dashed and dotted lines, respectively. As apparent from the dotted line (only silica temperature dependent), the initial rise in radius is due to the elastic hardening of the silica, allowing it to expand. The elastic constants of the quartz do not change appreciably at lower temperatures. The dramatic drop close to the β-quartz transition temperature is a result of the rapidly changing Poisson's ratio of quartz close to this temperature (dashed line). This was further verified by keeping E^m constant, and letting only ν^m vary with temperature. The same drop in the radius

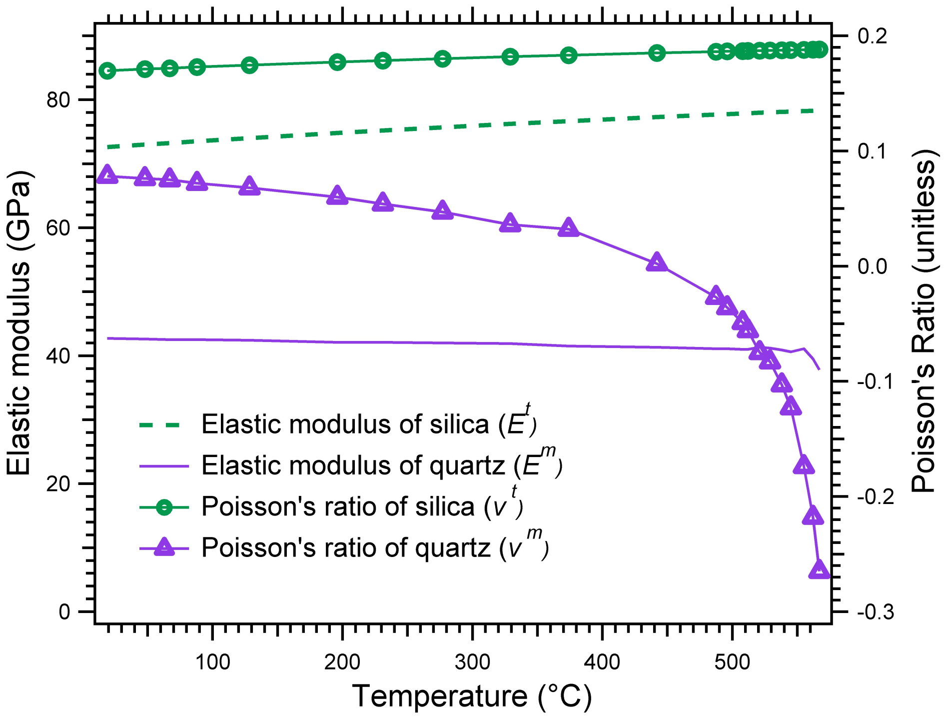

Figure 5.6: Experimental data for elastic modulus E and Poissons ratio ν in silica and quartz as a function of temperature. The data for silica is from [231] and for quartz from [233].

was observed. We note that ν^m becomes negative close to the transition temperature. A negative Poisson's ratio implies that the material expands sidewards on tension. In the current case, the quartz close to the track cannot expand sidewards, hence when ν^m becomes negative, the quartz "presses back" on the silica, reducing its expansion. We stress that it is not clear what the exact structure of silica inside an ion track is and thus whether it is appropriate to use the elastic constants of bulk fused silica in the analysis. The good agreement with the experiment however indicates that even if the silica in the track might differ from bulk fused silica, the temperature dependence of the elasticity is very similar.

The thermally-induced expansion of the silica tracks embedded in quartz in the first annealing cycle is well reproduced by the model described above. However, the track expansion is irreversible as evident from the second annealing cycle and the pre-annealing at 400 °C and thus unlikely to be mainly due to the elastic properties of the track. We note that the change in the track radius due to the elastic behavior propagates with the speed of sound and the observed increase occurs over minutes. The agreement of the model with the initial increase in the first cycle might thus be coincidental. However, after the initial irreversible track expansion, the drastic reduction in the track radius near the α-β quartz transition temperature is completely reversible.

Assuming the elastic constants of track and matrix material follow the temperature dependence of $a - SiO_2$ and $c - SiO_2$, a simple modification of the model yields a good agreement with the temperature cycles following the initial irreversible increase in the track radius. Adding an initial pressure offset P_0 to the contact pressure, P:

$$P \quad = \quad -\varepsilon\frac{1+\nu^t}{\frac{1+\nu^m}{E^m}+\frac{1-\nu^t-2(\nu^t)^2}{E^t}}+P_0 \tag{5.4}$$

in equation 5.1 with a magnitude of 35±3 GPa, explains the experimental data for the annealing cycles following the initial irreversible expansion very well. The calculations using this modified model are shown in figures 5.3 (b), 5.4 (b) and (c), and 5.5 (b) and (c) as dashed lines. The added offset pressure is in the same order of magnitude as the pressure that is experienced by the track at ~400 °C when it is first annealed (e.g. P calculated from equation 5.2 at ~400 °C). Strain in the vicinity of ion tracks in quartz has been reported previously [42] and fracturing of the samples irradiated with a fluence of 4 $\times 10^{11}$ ions/cm^2 (explained in section 4.1.2) also confirms the high stresses in the material. It is thus conceivable that the tracks are subjected to significant pressure before annealing, in fact, the observed behavior yields a measure of that pressure. The initial irreversible expansion may be a consequence of the complex volume change of $a-SiO_2$ under different temperature and pressure conditions that has been reported previously [239, 240]. The volume expansion of densified silica glass annealed at different temperatures has been observed within a few minutes and it was indicated that the annealing process is dependent on the mechanical and thermal history and can also be affected by temperature [239].

5.2.3 Track damage recovery in quartz

To study the annealing kinetics and calculating the activation energy of ion track recovery in quartz, three samples irradiated with 1.5 GeV ^{238}U ions to a fluence of 1×10^{11} ions/cm^2 that were polished to 60-70 μm thick, were annealed isothermally. In an initial annealing step, the temperature of each sample was increased to 650 °C with a rate of 130 °C/min and the sample was annealed at this temperature for ~20 min to allow the initial expansion/relaxation of the ion tracks discussed in the last section. The temperature of the samples was then increased to 1010, 1040, or 1070 °C and frequent SAXS measurement taken until a significant change in the scattering image from ion tracks was apparent. Figure 5.7 shows the evolution of the scattering signal from ion tracks in the SAXS images after the sample just reaches its isothermal annealing temperature of 1070 °C and after approximately 5, 10, 15, and 20 min annealing. By increasing the annealing time, the spacing of the oscillations in the streaks increases and eventually the outer oscillations fade away. This is an indication that the track radius is decreasing. However, the presence of the track scattering as narrow streaks even after annealing for 20 min indicates a remaining large aspect-ratio and thus no significant fragmentation of the tracks. After about 20 min annealing, the signal from the tracks is very weak and no reliable data can be extracted. Later in this chapter we will show the effect of track fragmentation in the SAXS images apparent for ion tracks in olivine.

Figure 5.8 shows SAXS spectra from ion tracks for the three quartz samples at room temperature, just before reaching the temperature for each isothermal annealing (1010, 1040, or 1070 °C), and after 10 min annealing at their specific temperatures. The solid lines are the fits to the hard cylinder model. It is clear that after 10 min of annealing, for the samples annealed at 1010 and 1040 °C, the shift in the position of the first minima which results in the change in the track radii is relatively smaller than for the sample

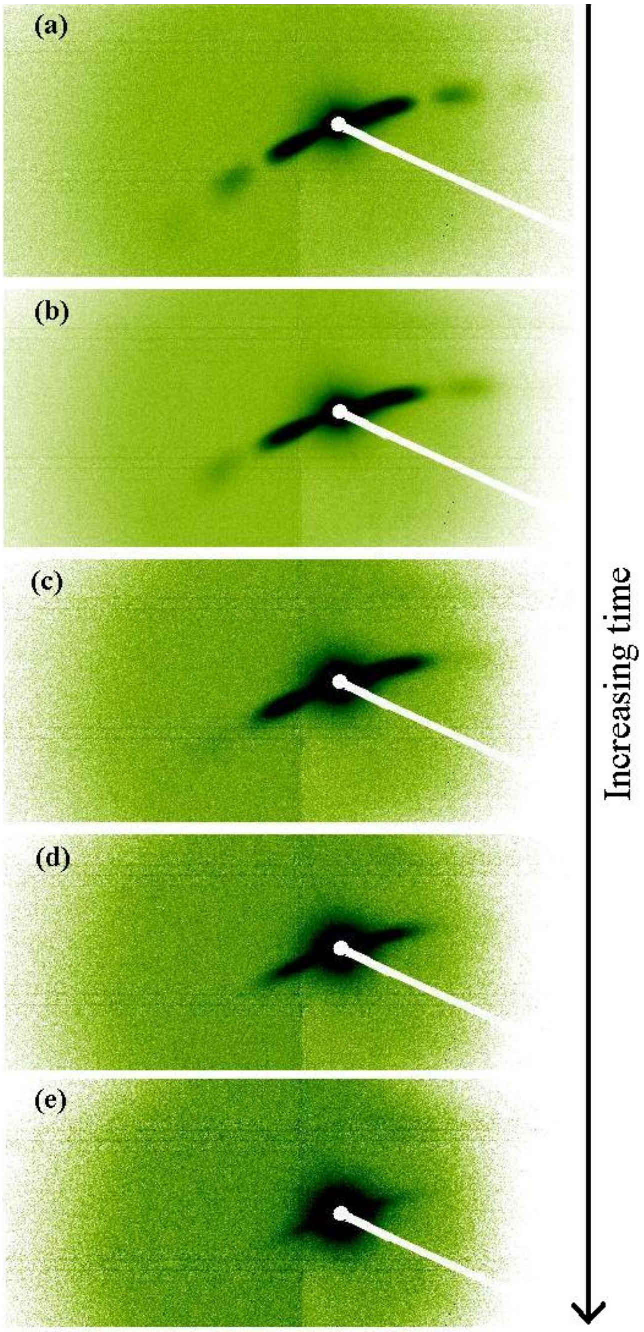

Figure 5.7: SAXS images of ion tracks in quartz (a) just as the sample temperature reaches 1070 °C, and after (b) 5 min, (c) 10 min, (d) 15 min, and (e) 20 min annealing at this temperature.

annealed at 1070 °C. This is expected as the rate of track damage recovery is higher at higher temperatures.

By fitting the SAXS data using the hard cylinder model, track radii are extracted and plotted in figure 5.9 as a function of time for the three isothermal annealing experiments. After passing the initial annealing at 650 °C, the temperature of ion tracks was rapidly increased to the specific temperatures required.

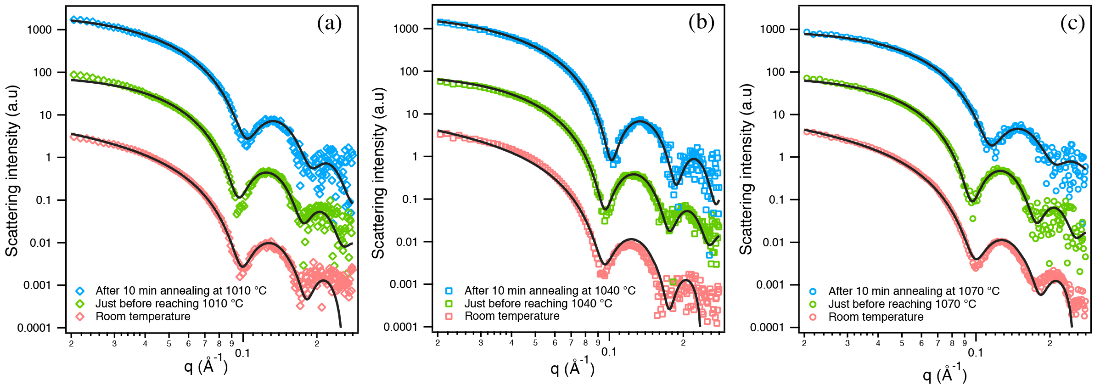

Figure 5.8: Selected scattering intensities from ion tracks in three quartz samples used for isothermal annealing. Spectra are shown at room temperature, just before reaching the specific temperature for isothermal annealing and after about 10 min annealing at each temperature.

In order to calculate the activation energy of damage recovery in quartz, we take into account the changes in the track radii from the time that the temperature reaches 1010, 1040, or 1070 °C for each sample. This point is shown on the plot as time equal zero in figure 5.9.

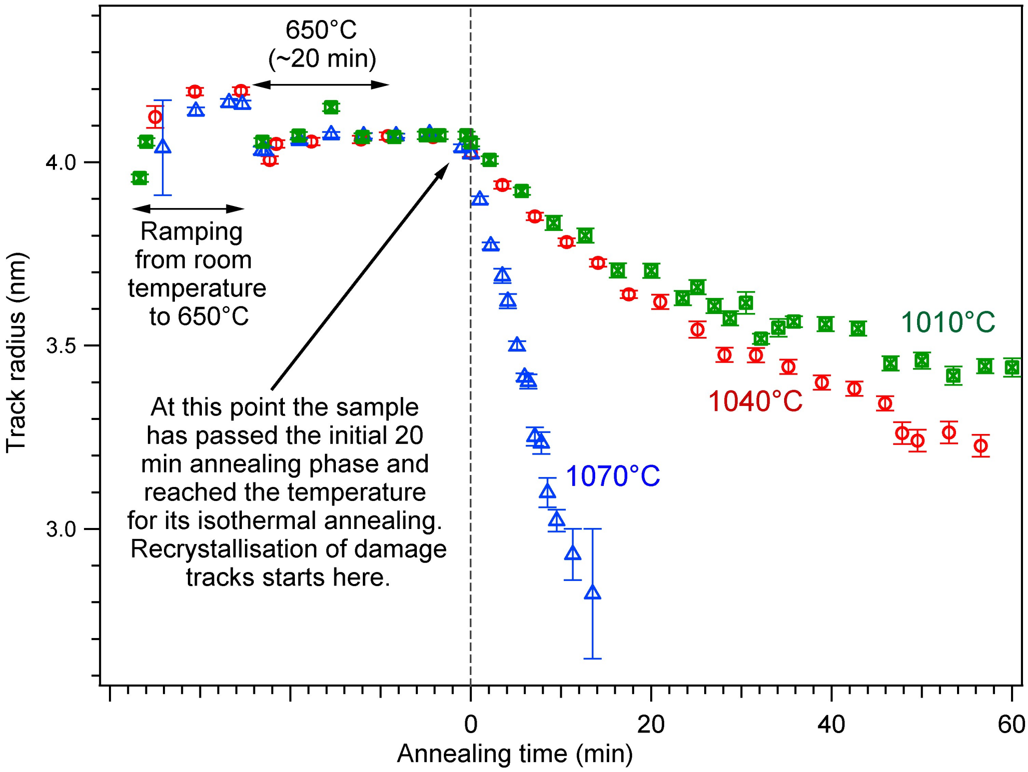

Figure 5.9: Ion track radii in quartz as a function of annealing time for the 3 isothermal annealing experiments.

In order to calculate the activation energy (E_a) for the damage recovery of the amorphous tracks in quartz, we have used the cross-cut method [221, 222]. By assuming that track damage occurs as a result of a single activated process with a constant E_a, the rate of change of the concentration of defects can be described as [221]:

$$dn/dt \quad = \quad -F(n)A_0\exp(-E_a/kT) \tag{5.5}$$

where n is the fractional concentration of defects, $F(n)$ is any continuous function of n, A_0 is a pre-exponential constant, and k is the Boltzmann constant. Here we take the *cross sectional area* of the ion tracks (πr^2) as the fractional concentration of defects n. A plot of the area as a function of time from the start of the recovery process is shown in figure 5.10. At time equal zero the initial defect concentration (n_0) is same for the three samples. In order to simulate a continuous annealing behavior, the three experimental data sets are fitted with an exponential function ($y = A\exp(-x/C)+B$) which are shown as solid lines.

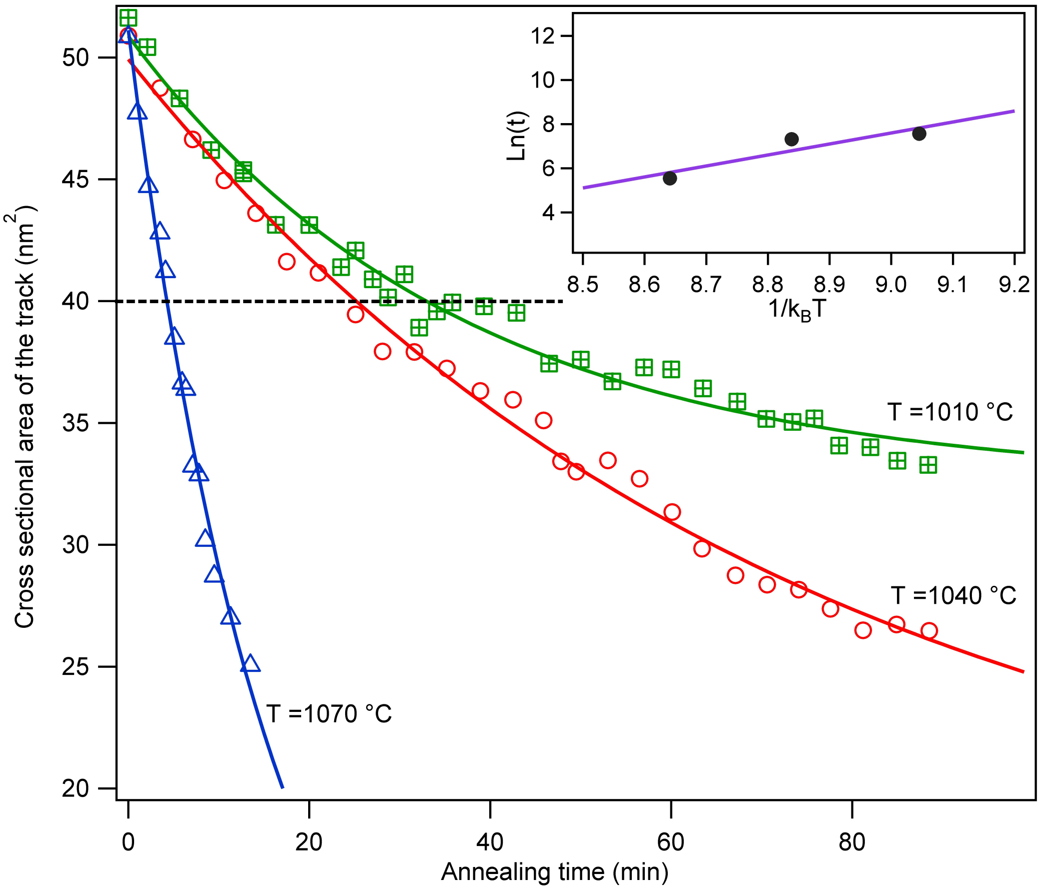

Figure 5.10: Cross sectional area of ion tracks as a function of time in isothermal annealing of tracks in quartz for three different temperatures. The solid lines are exponential fits to the data. The dashed line is the cross cut for calculating the activation energy. The inset shows the linear fit to the data from the three points intersected with the cross cut horizontal dashed line.

By rearranging the equation 5.5 we have:

$$-\int_{n_0}^{n_1} \frac{dn}{F(n)} = A_0 t \exp(-E_a/kT) \quad (5.6)$$

If a horizontal line is drawn on the plot of area versus time at a given value of n (as drawn in figure 5.10), then the left hand side of the equation 5.6 becomes a constant C:

$$t \exp(-E_a/kT) = C \quad (5.7)$$

Therefore to reach a constant value of n at temperatures T_1 and T_2, time t_1 and time t_2 are required:

$$ln\frac{t_1}{t_2} = \frac{E_a}{k}(\frac{1}{T_1} - \frac{1}{T_2}) \quad (5.8)$$

When the horizontal cut crosses each curve, for each crossing point, t_i can be related to T_i:

$$ln(t_i) = lnC + E_a/kT_i \quad (5.9)$$

Linear plotting of the $Ln(t_i)$ versus $1/kT_i$, returns a slope which is E_a, an example of which is shown in the inset of figure 5.10. Ideally, taking the horizontal cut at different points would only change the constant in equation 5.9 and the lines described by the equation should be parallel and result in a same E_a. To obtain a value for E_a from the experimental data, we have taken 100 sets of three points from 100 cross cuts. Taking the average of the slope of the linear fits calculates an activation energy of 4.6±0.2 eV. A distribution plot of the E_a values is shown in figure 5.11

A broad activation energy spectrum for recovery of the radiation damage in quartz has been suggested before [228]. Previously a two stage annealing process proposed for epitaxial regrowth of amorphised quartz in reference [227] obtained values of 0.6±0.1 eV and 3.6±0.4 eV for temperatures below and above 1070 K, respectively [227]. For damage recovery of swift heavy ion tracks in natural quartz activation energies of 2.11 and 3.83 eV were calculated based on data from chemical etching experiments [163, 162]. The activation energy calculated from our SAXS experiment is slightly higher than the previously reported values. We note that damage recovery can be different in natural and synthetic quartz and it can also be affected by crystallographic orientation with respect to the tracks [229, 164].

5.3 Damage recovery of ion tracks in apatite

Annealing of ion tracks in apatite is of interest for applications in geochronology [6, 241, 218]. Many of the studies conducted on annealing of induced or natural fission tracks in apatite are performed by means of chemical etching [242, 218, 64] where the distribution of etched length of the tracks is investigated. For example, Green et al. [218] have shown that the rate of track shortening increases exponentially with increasing

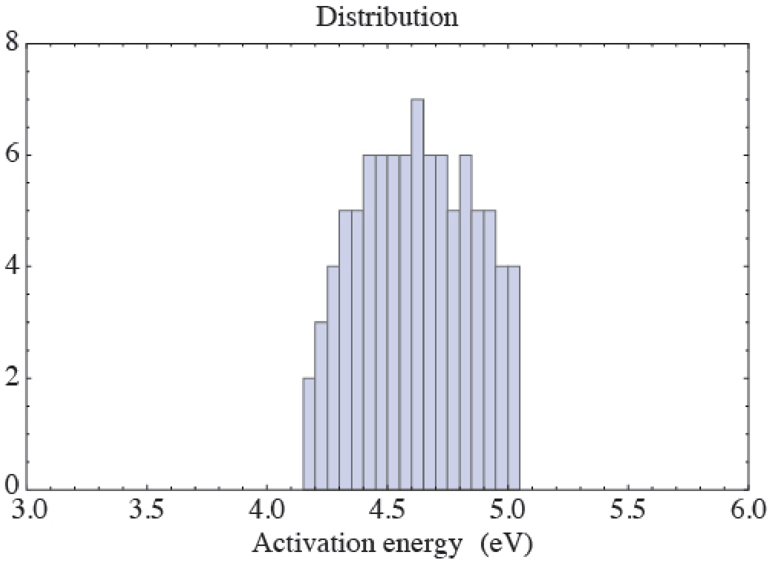

Figure 5.11: Histogram of the distribution of the activation energy for damage recovery in quartz from the cross-cut method.

annealing temperature. Annealing rates have also been shown to be dependent on the chemical composition of apatite [241, 243] and crystallographic orientation [242, 244]. Annealing studies on un-etched ion tracks in Durango apatite have been performed using high-resolution TEM combined with *ex situ* and *in situ* heating [43, 107]. In one study the apatite sample irradiated with 2.2 GeV Au ions was crushed and suspended on a carbon film and was studied under a high-resolution TEM [43]. The tracks were reported to be porous and annealing at 700 °C resulted in segmentation of the long tracks into isolated droplets due to Rayleigh instabilities and preferential motion of highly porous segments, in addition to the shrinkage of porous tracks by thermal emission of vacancies to the surrounding solid [43]. Remnants of the tracks, in the form of isolated segments, were present even after 130 min of annealing at 700 °C [43]. In a more recent TEM study shorter tracks (~8 μm) generated with 80 MeV Xe ions in Durango apatite were imaged along their entire length and annealed *in situ* [107]. Results indicated a dependency of the annealing rate on track diameter along its length with track annealing significantly increased as the track diameter decreased along the ion trajectory [107]. Annealing of the tracks for 1 h at 330 °C and 1 h at 380 °C resulted in almost no significant change in the track size close to the sample surface, yet significant segmentation and shrinkage of tracks in the middle section of the track along its length and disappearance of the track closer to the end of ion trajectory was observed [107].

In this section the annealing kinetics of ion tracks in Durango apatite is studied using SAXS and activation energies for the track damage recovery are determined. In contrast to the TEM work, the use of bulk samples avoids possible artifacts due to sample preparation and the measurement of a large number of tracks provides superior statistics.

5.3.1 Experimental

A 30 μm thick Durango apatite sample was irradiated at the UNILAC accelerator at the GSI Helmholtz Centre using 2.2 GeV ^{197}Au ions to a fluence of 5×10^{10} ions/cm^2.

The range of the projectile ion exceeds far beyond the sample thickness as estimated by SRIM-2008. Therefore, the ion tracks generated in the crystal extend through the entire thickness of the sample. The sample was then cut in to two parts and one part was used for isochronal annealing experiments as a function of temperature (*ex situ*) and another part for isothermal annealing as a function of time (*in situ*).

SAXS measurements were performed with an X-ray energy of 12 keV and a camera length of approximately 1600 mm. For the *ex situ* annealing measurements, the sample was sequentially annealed at temperatures between 200 and 500 °C for 30 min in a furnace under ambient conditions. SAXS measurements were taken in between annealing steps. For the *in situ* annealing, the second part of the same sample was heated to 350 °C for 360 min during the SAXS measurements using a hot-air heater that was positioned underneath the sample. The sample temperature was monitored with a thermocouple at sample height. The temperature reached 335 °C after approximately 5 min and 350 °C after about 30 min. Measurements were taken approximately every 40 s with exposure times of 2 and 5 s.

5.3.2 Isochronal annealing of ion tracks in Durango apatite

Figure 5.12 shows SAXS images from the apatite sample at room temperature, 380 and 500 °C. At 380 °C it is evident that the signal from the tracks (the bent streak) is fading compared to the signal at room temperature. However the projection of the scattering intensity in a direction perpendicular to the streaks is still small and has not changed compared to the SAXS image at room temperature. This implies that the tracks still largely remain as continuous long cylindrical objects and no fragmentation is apparent. At 500 °C the signal from the tracks has vanished which is an indication of complete recovery of the damage. We note that the straight lines in the SAXS image at 500 °C are parasitic scattering from the sample and do not originate from the tracks.

Scattering intensities from the *ex situ* annealing experiment extracted from the SAXS image taken after each temperature step are shown in figure 5.13 as symbols. Solid lines are corresponding analytical fits to the hard cylinder model explained in section 3.4.6.

Figure 5.13 reveals a smoothing of the oscillations in the scattering intensity with increasing temperature. A variety of conceivable density distributions in the cylindrical tracks was explored in order to explain this behavior, including introduction of a density gradient between track and matrix, increasing polydispersity in the track radius, and damping as a consequence of amorphous/crystalline track interface roughness [140], the latter producing the best fits. At temperatures above 400 °C, reliable analysis of the scattering intensities due to the absence of oscillations could not be performed. After annealing at 500 °C no residual scattering could be detected.

With increasing temperature, an increase in the spacing of the oscillations in the scattering intensities, indicates a reduction in track radius, the evolution of which is plotted in figure 5.14 as a function of annealing temperature. Initially, below 300 °C, there is a small reduction of the track radius which is followed by a significant change in the track radius above 300 °C when its value drops to approximately 3 nm.

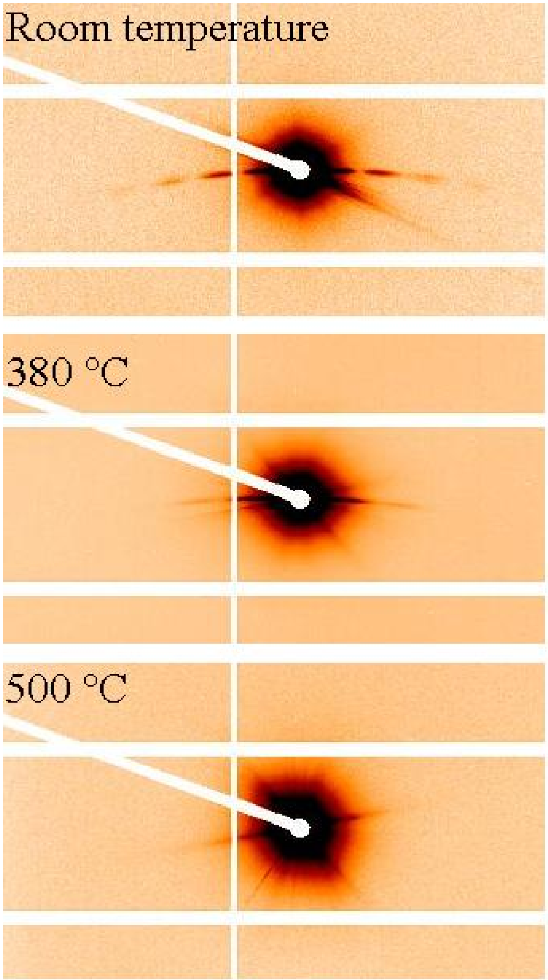

Figure 5.12: SAXS images of ion tracks in the apatite sample at room temperature, 380 and 500 °C.

5.3.3 Isothermal annealing of ion tracks in Durango apatite

The *in situ* annealing experiments were performed recording the evolution of the scattering intensity over a duration of approximately 6 h. Figure 5.15 shows the evolution of the scattering intensity with time. It is evident that by increasing the annealing time, the oscillations of the scattering spectra are fading and by extracting the track radii, it is clear that the tracks are shrinking in size as plotted in figure 5.16.

Similar to the *ex situ* annealing result, two regimes are apparent, the first characterized by a decrease in the track radius with a rate of $\sim 2 \times 10^{-2}$ nm/min in the first 15 min, followed by a significantly slower, approximately constant rate of $\sim 3 \times 10^{-4}$ nm/min over the remaining duration of the experiment.

5.3.4 Activation energy for track recrystallisation in Durango apatite

In order to quantify the kinetics of annealing, Modgil and Virk [223] proposed an empirical formula based on an Arrhenius equation, relating the annealing rate, V_a, which is the rate

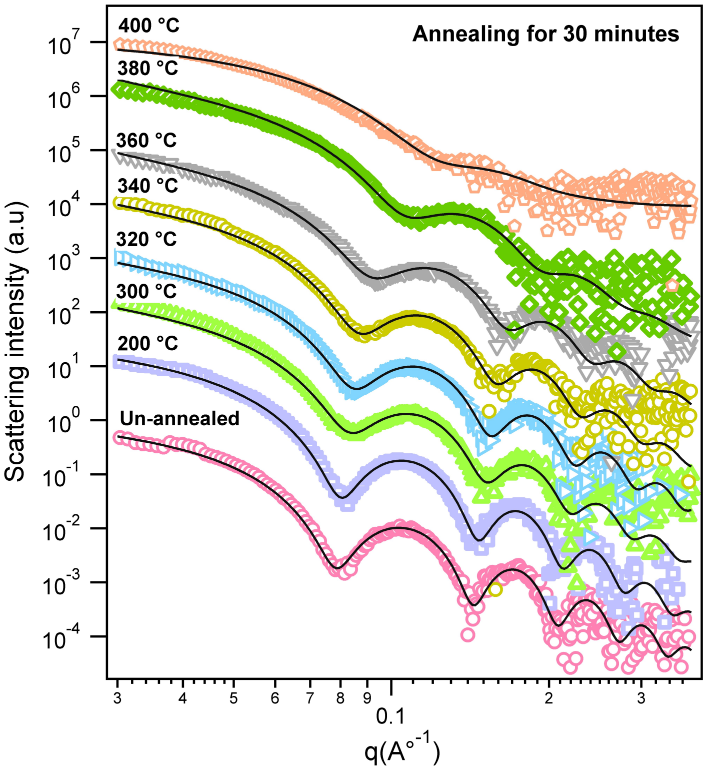

Figure 5.13: Scattering intensities as a function of scattering vector q for the same sample irradiated with 2.2 GeV Au ions before and after annealing at different temperatures for 30 min. The solid lines correspond to the fits assuming cylinders with sharp boundaries. The spectra are offset for clarity.

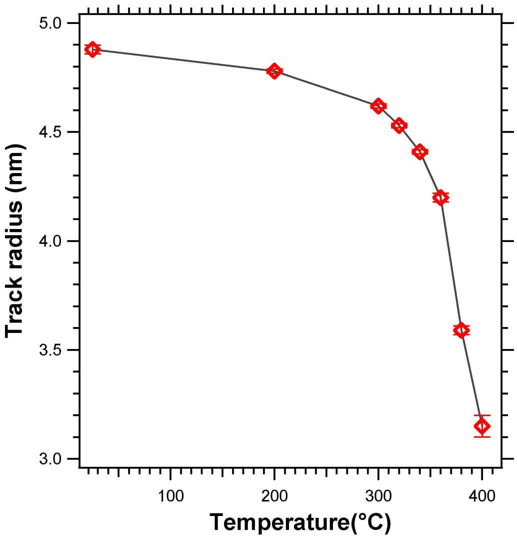

Figure 5.14: Ion-track radius as a function of annealing temperature; the solid line is to guide the eye.

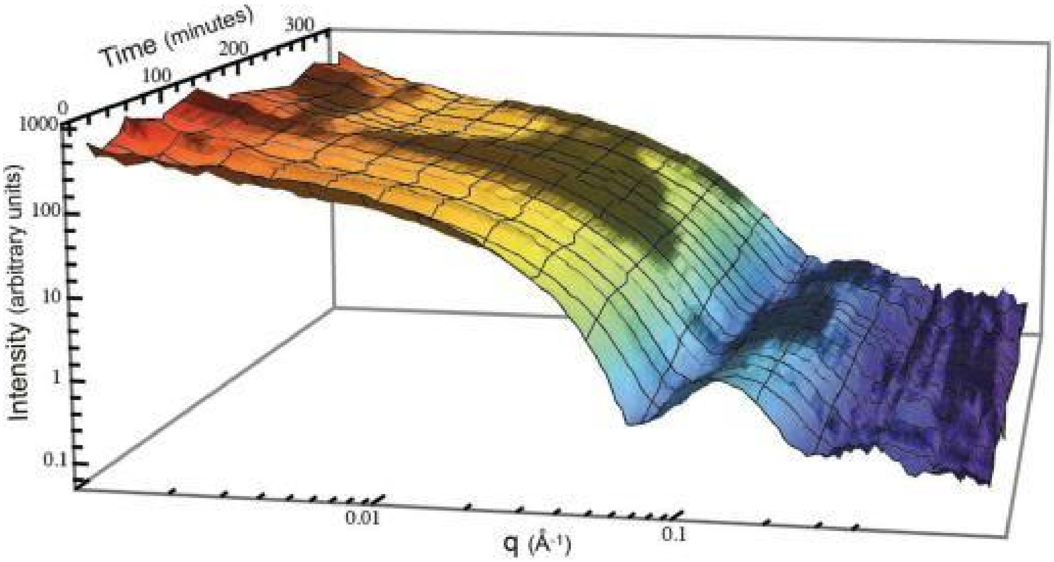

Figure 5.15: *In situ* annealing of ion tracks at 350 °C, the evolution of the scattering intensity with time for the apatite sample irradiated with 2.2 GeV Au ions.

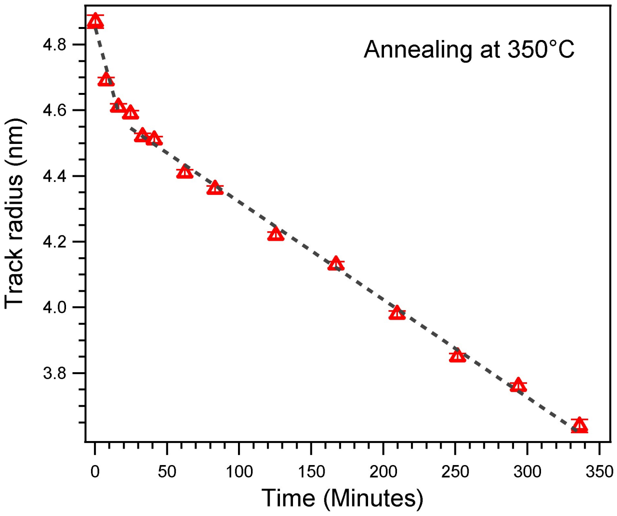

Figure 5.16: *In situ* annealing of ion tracks in apatite: the ion track radius is plotted as a function of the annealing time (red triangles); the dotted lines are linear fits for the two recovery stages. The error bars relating to the fits are smaller than the symbol size.

of change of length or diameter, to the activation energy E_a:

$$V_a = At^{-n}\exp(-\frac{E_a}{k_BT}) \tag{5.10}$$

where k_B is the Boltzmann constant, T is the annealing temperature, n is the exponent of the annealing time and A is the proportionality constant. To find the activation energy from our *ex situ* annealing experiments, equation 5.10 can be written in the form of:

$$\begin{aligned}\frac{dR}{dt} &= V_a, \\ \int_{R_0}^{R} dR &= \int_0^t At^{-n}\exp(-\frac{E_a}{k_B T})dt, \\ R - R_0 &= \frac{A}{-n+1}t^{-n+1}\exp(-\frac{E_a}{k_B T}) + C\end{aligned} \tag{5.11}$$

At the time equal to zero, the radius of the track is the initial radius, thus the integration constant is zero. Taking into account that the sample was annealed at each temperature for a constant time, we have:

$$ln(1 - \frac{R}{R_0}) = -\frac{E_a}{k_B T} + A' \tag{5.12}$$

With A' including all constants. $ln(1-R/R_0)$ versus $1/K_B T$ thus resembles a straight line with the slope of $-E_a$. The annealing time only affects the offset of the line with no effect on the activation energy.

Figure 5.17 shows the fit of the extracted data from *ex situ* annealing of ion tracks in apatite to the discussed model. The linear regression of the data yields two activation energies for low and high temperatures and the annealing is characterized by two stages. In stage I, up to 300 °C, there is a small but measurable reduction of the track radius, while stage II exhibits a more rapid decrease at higher temperatures. The activation energies of the two stages for the given annealing conditions, extracted from the *ex situ* annealing data [223], are 0.23±0.05 eV for stage I and 0.72±0.02 eV for stage II. The latter is consistent with previously reported value for the activation energy of track recovery in apatite measured by means of chemical etching [245].

A two-stage recrystallization process due to progressive 200 keV electron irradiation has previously been reported for a synthetic apatite structure-type $[Sr_2Nd_8(SiO_4)_6O_2]$ pre-amorphized by low-energy ion irradiation [196]. Stage I of the annealing is essentially athermal and consistent with a structural relaxation of the amorphous phase, possibly facilitated by point defect annihilation. A rapid quenching of the liquid phase in the ion track can leave an amorphous phase in a state that relaxes into an energetically more favorable configuration upon annealing below the recrystallization temperature, as reported for semiconductor materials [246]. Stage II of the annealing process, characterized by the higher activation energy and lower rate, is consistent with recrystallization of the amorphous material in the ion track. This is corroborated by the fact that the best fit to the data was achieved with a constant narrow distribution of sharp track radii, although with a roughness parameter that increases with increasing annealing temperature and time. As the ion tracks are not oriented with respect to a particular crystallographic axis or plane, an increase in interface roughness due to intrinsic differences in recrystallization kinetics for different crystallographic directions can be expected. Differences in annealing kinetics of fission tracks with different orientations are well documented for etched tracks in apatite [242]. For annealing up to 400 °C, where reliable analysis of the scattering intensities could be performed, the remaining high anisotropy in the scattering images

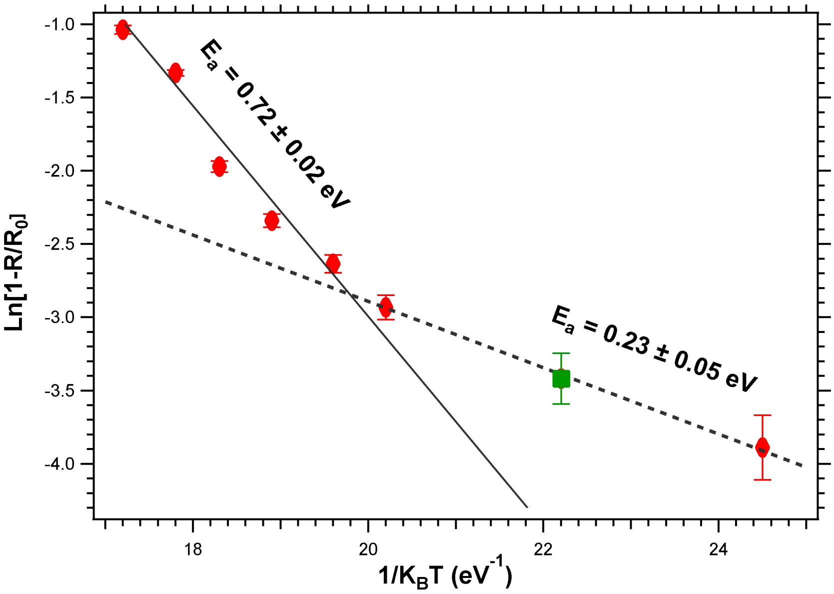

Figure 5.17: An Arrhenius plot of the ion-track radii for extraction of the activation energies associated with track damage recovery. The solid line is a linear fit to the data points from annealing at temperatures ≥300 °C. The dashed line is a linear fit to the data points from annealing at temperatures ≤300 °C. The green square is extracted from a repetition of the experiment under identical conditions.

indicates the absence of significant track fragmentation. We note that the temperatures in our annealing experiments, leading to recrystallization of the amorphous material, are significantly lower than the melting temperature of apatite [∼1300 °C (reference [247])], as typical for most solid phase recrystallization processes.

In summary, SAXS measurements of ion tracks in Durango apatite indicated recovery of the damage tracks at 500 °C in contrast to TEM observations of similar tracks at 700 °C [43]. We note that SAXS measures an ensemble of tracks in a sample and the extracted track radii are representative of the average track size. Moreover, the samples used in this work are bulk samples which have not been exposed to complicated preparation processes. In the recent TEM work of Li *et al.* [107], where e.g. annealing was performed *in situ* on short tracks (approximately 8 μm long), it was found that in the area where the track size becomes significantly smaller, closer to where the projectile ion stops in the sample, the annealing effect is much more pronounced. In our experiments, in contrast, the sample thicknesses were significantly smaller than the track length and thus they did not contain the "track end" section where the track radius is much smaller or includes point defects. Overall, despite the excellent agreement of SAXS and TEM for the track size at room temperature (explained in section 4.2.3), measurement of the damage recovery in apatite is different between the two techniques. This deviation may be explained by the different density changes measured with SAXS and TEM [43]. As indicated earlier, track recovery for porous fission tracks can be expected to behave significantly different from that of amorphous tracks.

5.4 Annealing of ion tracks in olivine

Previous investigations of the annealing behavior of irradiation damage in olivine have been mainly conducted to study the charge spectrum of ancient cosmic rays [248, 249]. Discrepancies in studies of the variation of the track etch velocity with the primary ionization rate or the variation of etchable track length with the atomic number of the incident ion has been attributed to partial annealing of the cosmic ray tracks occurring over time scales of 10^7 years [250, 251, 252, 253]. No work has been reported on the annealing of un-etched ion tracks to date.

5.4.1 Experimental

Crystalline samples of San Carlos olivine with thicknesses of 40 μm were irradiated at the UNILAC accelerator at the GSI Helmholtz Centre using 2.2 GeV ^{197}Au ions to a fluence of 5×10^{10} ions/cm^2. The length of the generated ion tracks exceeds the sample thickness as estimated by SRIM-2008.

Annealing of the ion tracks in olivine was conducted in similar ways to the annealing of apatite. For *in situ* annealing a hot-air heater was used and an external furnace was used for the *ex situ* annealing. Annealing at temperatures up to 1000 °C was performed for olivine where notable changes in the scattering signal were observed.

5.4.2 Annealing experiments of ion tracks in San Carlos olivine

Figure 5.18 shows SAXS spectra from ion tracks in olivine during 6 h of annealing at 350 °C. The solid lines are the fits to the hard cylinder model. Only small yet continuous changes in the extracted track radii as a function of time are observed as apparent in figure 5.19.

Unlike apatite, ion tracks in the olivine sample do not show substantial change after annealing for approximately 6 h at 350 °C. The total reduction of the track radius is less than 3% of the initial value with a rate of ~0.02 nm/ hour. In contrast, identical annealing results in about 25% reduction of the track radius in apatite with a rate of ~0.2 nm/hour, about a factor of 10 higher compared to olivine. The difference in the track radius reduction rate clearly indicates different recrystallization behavior despite the similar track morphology and radius prior to annealing.

In order to better understand the annealing behavior of ion tracks in olivine a second olivine sample was annealed *ex situ* at elevated temperatures up to 1050 °C. The sample was annealed at each temperature for 30 min and SAXS measurements were performed in between annealing steps. Figure 5.20 shows SAXS images at room temperature and at selected higher temperatures. The tracks are tilted by ~10° with respect to the X-ray beam. From the image at 510 °C one can see that the spacing of the oscillations is increased with respect to the room temperature image and thus the track is expected to be reduced in radius. The image at 650 °C shows the appearance of a new feature in the scattering signal in form of a bulging of the streaky signal which started at ~620 °C and increased in size with increasing annealing temperature. This bulging is most likely a consequence of fragmentation of the tracks.

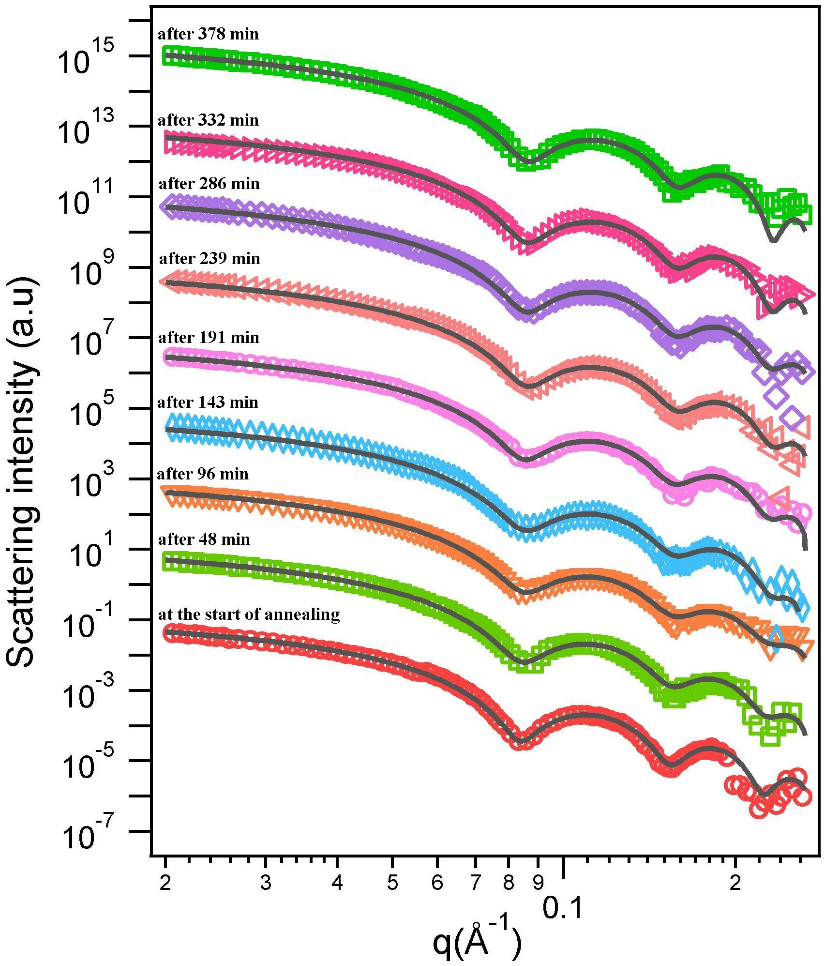

Figure 5.18: Scattering intensities from ion tracks in olivine as a function of scattering vector. Tracks were annealed at 350 °C for 6 h. Solid lines are fits to the hard cylinder model.

Up to the temperature where fragmentation of the tracks began, the scattering intensities from ion tracks can be extracted and are shown in figure 5.21 along with the fits using the hard cylinder model. At higher temperatures, existence of the new features in the scattering images resulted in scattering intensities that could not be fitted with the available track models including different core-shell and soft-cylinder models. Oxidation of the olivine that occurs in air above 600 °C [254, 255] can also have an effect on the anomaly seen in the scattering images at higher temperatures. Even though we can not quantify the amount of oxidation or separate its effect from the scattering signals of the tracks, we have annealed an un-irradiated olivine sample at 1050 °C for 30 min and the SAXS image from this sample also shows an anisotropic scattering signal as shown in figure 5.22.

The track radii extracted from the fits to the SAXS spectra up to 570 °C are plotted as a function of the annealing temperature in figure 5.23 which shows that a significant reduction of the track radius starts at about 400 °C. The inset of figure 5.23 shows an Arrhenius plot with linear fits to two regions in order to obtain the activation energies

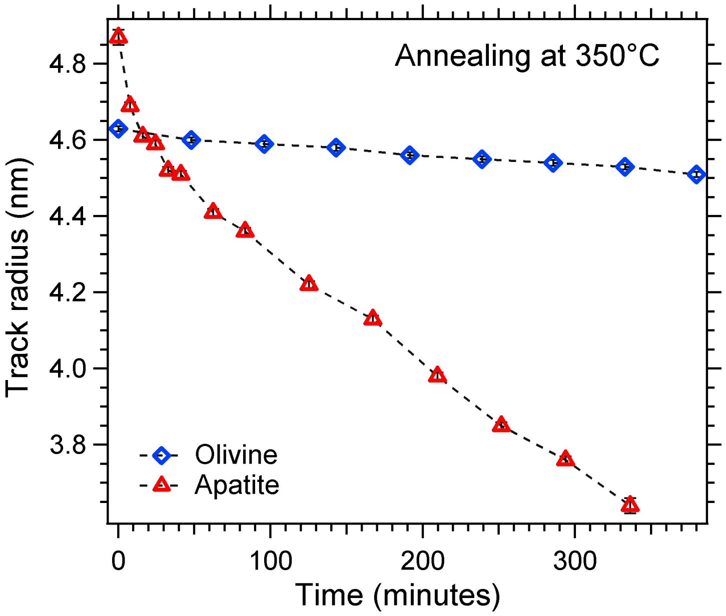

Figure 5.19: Track radius as a function of annealing time for *in situ* annealing at 350 °C extracted from the hard cylinder fits. Error bars are included in the graph and in some cases are smaller than size of the data point. Dashed lines are to guide the eye. The data from the apatite sample is added for comparison.

involved. Similar to the annealing of ion tracks in apatite, the recovery process in olivine appears to proceed in two stages. However, below 360 °C, due to lack of sufficient data points, estimation of an activation energy was not pursued. For temperatures above 360 °C, (solid line), the activation energy for the damage recovery is 0.40±0.04 eV. In order to understand the full damage recovery of ion tracks in olivine isothermal *in situ* annealing experiments will need to be performed at a variety of temperatures. In addition, to avoid oxidation, annealing experiments should preferably be carried out in reducing atmospheres. To extract more quantitative results from annealing above 600 °C more sophisticated models need to be developed to account for the observed track fragmentation.

Although the set of experiments performed for this work can not provide a full explanation of the recovery of ion irradiation damage in olivine, our SAXS results provide some insight into the annealing behavior of tracks in the crystal and are useful for designing appropriate experiments in order to further quantify the recovery process. Our preliminary results indicate that despite a very similar track morphology at room temperature, the annealing behavior of the damage tracks is very different to that of apatite.

5.5 Conclusions

We have demonstrated that SAXS is well suited for determining the annealing behavior of ion tracks and can resolve relative changes of the track radius in the order of 0.1 nm in quartz, apatite, and olivine. Combined with the quick acquisition times, SAXS is well suited for studying the annealing kinetics of the ion-track damage using *in situ* experiments.

Isochronal annealing of ion tracks in synthetic quartz was carried out in an attempt to understand an observed peculiar change in the track radius in the temperature range below 620 °C, e.g. before the start of the damage recovery. Results revealed that a thermally-induced expansion of the ion tracks in quartz is irreversible when tracks are annealed up to ∼450 °C. Moreover, we have observed that elastic properties of quartz close to the temperature of its phase transition cause a reversible shrinkage of the track which can be explained by changes in the elastic behavior of quartz at these temperatures. Isothermal annealing of ion tracks in quartz at temperatures above 1000 °C enabled calculation of an activation energy for recrystallisation of 4.6±0.2 eV using the cross-cut method.

In apatite, the annealing kinetics suggests a two stage process is operational, consistent with structural relaxation followed by recrystallisation of the damage tracks. While the track radii in apatite and olivine are very similar, the *in situ* annealing experiments revealed a significantly higher recovery rate of the damaged areas in apatite as compared with olivine. *Ex situ* annealing of ion tracks in olivine indicated fragmentation of the tracks above ∼600 °C and possible oxidation of the material at temperatures above 800 °C. In order to fully address the difference of ion tracks in the two minerals, further annealing experiments and advanced analytical models are needed. Using an Arrhenius plot activation energies of 0.72±0.02 eV and 0.40±0.04 eV were calculated for the recrystallisation of the damage in apatite and olivine, respectively.

The high accuracy with which the track radii can be determined, as well as the implementation of *in situ* annealing experiments with good time resolution, provides a new means for in-depth studies of ion-track annealing. In minerals such as apatite, it enables to study track annealing for a wide variety of geological conditions, including variations in composition, crystal orientation, and pressure, without the need for chemical etching. This understanding is central to a fuller development and exploitation of current fission track methods in both geochronology and thermochronology and to broader applications of unambiguous interpretation of etched ion track distributions.

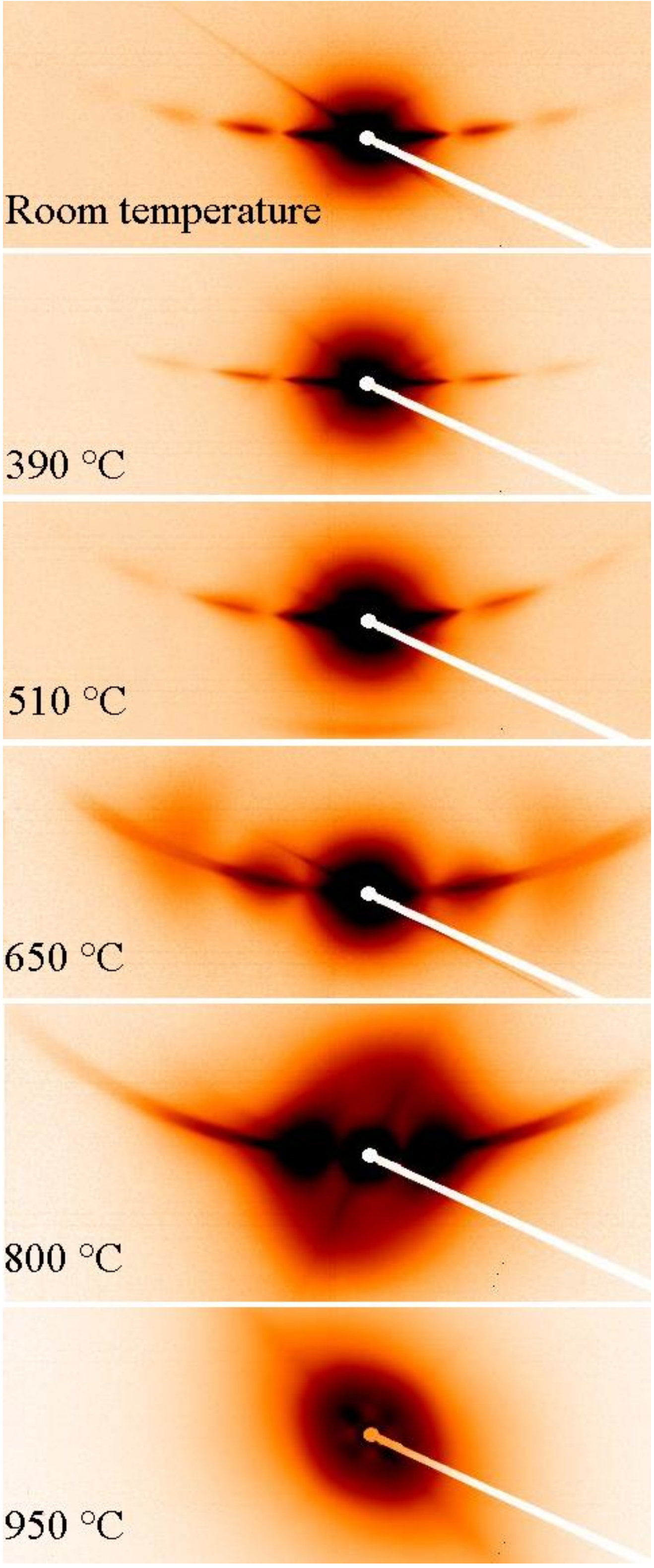

Figure 5.20: SAXS images of ion tracks in olivine sample at room temperature and selected temperatures during *ex situ* annealing. At higher temperatures (above ~700 °C), the bulging of the scattering signals indicates track fragmentation.

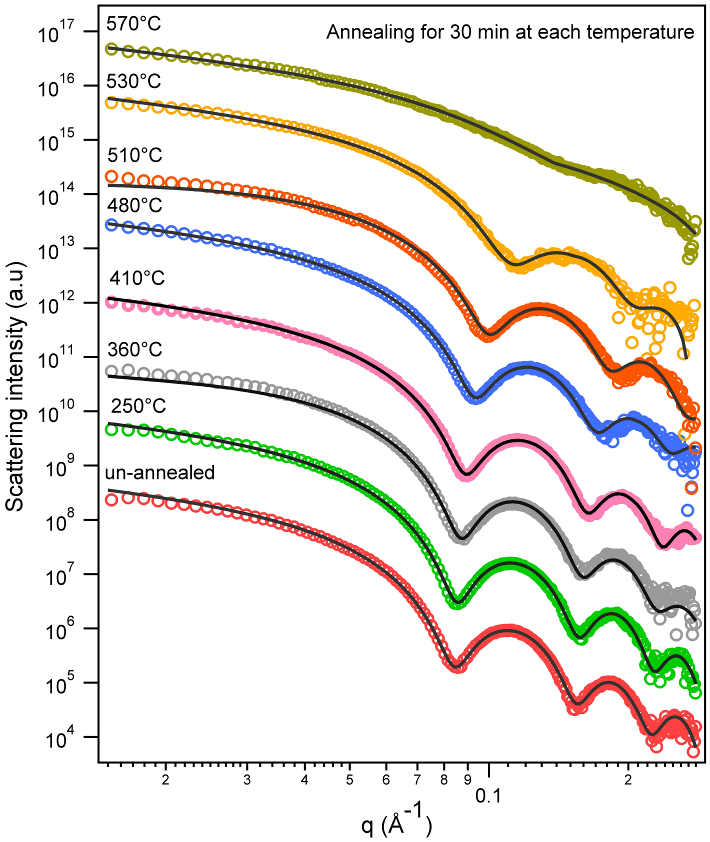

Figure 5.21: Scattering intensities as a function of the scattering vector q for ion tracks in olivine sample irradiated with 2.2 GeV Au at room temperature and at elevated temperatures up to 570 °C. The solid lines correspond to the fits using the hard cylinder model. The spectra are offset for clarity.

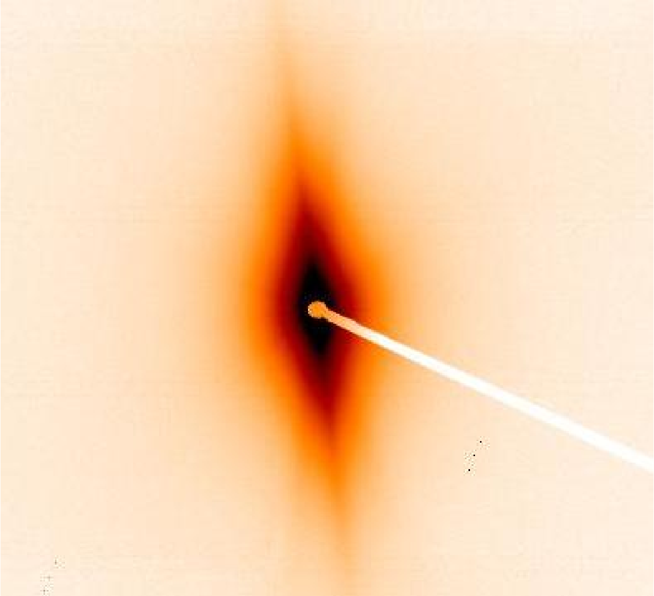

Figure 5.22: SAXS image from an un-irradiated San Carlos olivine sample annealed at 1050 °C for 30 min.

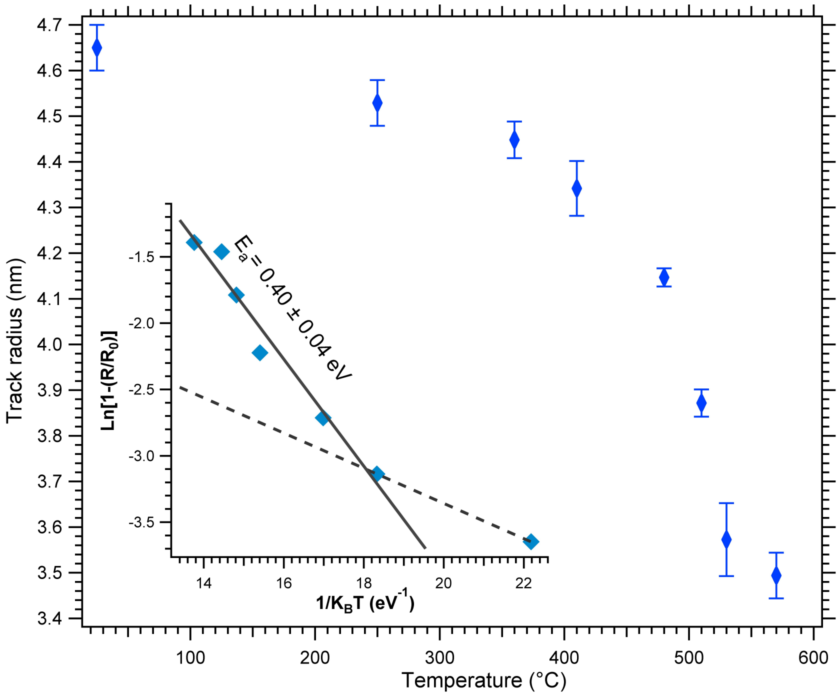

Figure 5.23: Ion track radii in olivine as a function of the annealing temperature. Above 600 °C the signal from the tracks could not be extracted and analysed. The inset shows an Arrhenius plot of ion track radii for extraction of an activation energy. The solid line is the linear fit to the data points from annealing at temperatures ≥360 °C (E_a = 0.40±0.04 eV). The dashed line indicates that the recovery process may have an initial stage, however, there are insufficient data points to calculate an activation energy.

Chapter 6

Summary and conclusions

In this work, swift heavy ion tracks were studied in synthetic quartz and two minerals, Durango apatite and San Carlos olivine using synchrotron-based small-angle X-ray scattering (SAXS). The tracks were generated using a variety of heavy ions (Au, U, Pb, Xe, Ru, I, and Ni) with energies in the range of hundreds of MeV to a few GeV. Irradiation fluences ranged mainly between 5×10^{10} and 3×10^{11} ions/cm^2 to create well separated tracks. Ion irradiation of all samples was performed at room temperature and normal to the sample surface.

SAXS was used to study the morphology of the ion tracks, and combination with *ex situ* isochronal and *in situ* isothermal annealing experiments enabled investigation of the annealing behavior and recovery of the damage tracks. Theoretical models developed for the analysis of the SAXS data were used for detailed characterization of the track morphology and determination of the track radii with great precision both at room temperature and upon annealing. The morphology of the ion track studied in the three crystals was consistent with a cylinder with constant electron density, different from that of its matrix. The sharp boundaries between the electron density of the track and the matrix is consistent with amorphous tracks inside a crystalline material. The optimization of SAXS protocols facilitated measurement of ion track ensembles in bulk samples in a variety of materials and under different experimental conditions. The short data acquisition times enabled time resolved measurements with sufficient resolution to study kinetic processes operational during annealing. Absolute calibration of the scattering intensities facilitated an estimate of the electron density change within the ion tracks.

In quartz, SAXS measurements of ion tracks indicated an increase in the track radii with increasing electronic energy loss (dE/dx_e) up to ∼17 keV/nm whereafter the track radii remain constant at approximately 4 nm with further increasing of dE/dx_e. In contrast, RBS/C measurements [48, 160, 161] and molecular dynamics simulations indicate larger track radii at high values of dE/dx_e. The deviation of the results from the three techniques may be explained by the different sensitivity of each technique to different aspects of the track. SAXS measures the volume where the electron density of the damaged material is different from that of the matrix while RBS/C measures the area where the damage is amorphous or the crystal is imperfect. Using the absolute scattering intensity from SAXS measurements, the electron density difference between the tracks and the matrix in quartz is estimated to be approximately 2±1% for all irradiation conditions. The latter result is in contrast with observations from macroscopic swelling measurement for low fluences but is significantly lower than the ∼15% density difference between bulk silica and quartz, leading to high stresses in the material.

Ion tracks in quartz were cycled through 5 min annealing steps between room temperature and 620 °C. The annealing leads to an initial irreversible increase in the track radius by ∼6%, whereafter a reversible shrinkage is apparent near the transition temperature from α to β-quartz. An elastic model considering the ion tracks as cylindrical inclusions was used to explain the decrease in the track radii. The model was modified by adding an initial constant pressure on the tracks after the irreversible expansion. The agreement of the model with the data verifies the validity of the macroscopic elastic model on a nano scale. Annealing of ion tracks at temperatures above 1000 °C was performed in order to study the damage recovery in quartz. Three isothermal *in situ* annealing experiments were conducted at temperatures of 1010, 1040, and 1070 °C. Using a cross-cut method [221], an average value of 4.6±0.2 eV was estimated for the activation energy, attributed to recrystallisation of the amorphous tracks.

SAXS measurements of ion tracks in apatite and olivine show very similar track radii at room temperature. In both minerals track radii increase almost linearly with dE/dx_e up to about 26 keV/nm and flattens afterward. Different ion velocities with similar energy loss yielded significantly different track radii in apatite consistent with the velocity effect. The measured electron density change in the track damage has a similar value of approximately 1% compared to the matrix in both crystals, independent of the irradiation conditions. However, annealing of ion tracks in apatite and olivine showed a very different damage recovery behavior. Ion tracks in apatite and olivine generated under the same irradiation condition were annealed isothermally at 350 °C for about 6 h. While this annealing resulted in about 25% reduction of the track radius in apatite, the total reduction in olivine was less than 3% of the initial value, indicating that tracks in olivine are more resistent to annealing.

Annealing of ion tracks in apatite and olivine was further investigated by isochronal *ex situ* annealing experiments where each sample was annealed at temperatures in a furnace and after each annealing step, the SAXS measurement was performed. In apatite, a two stage recovery process was observed with activation energies of 0.23±0.05 eV for temperatures below 300 °C and 0.72±0.02 eV for temperatures above 300 °C. SAXS spectra from ion tracks in apatite indicated no fragmentation of the tracks even when the track radii decreased by ∼40%. After annealing at 500 °C no residual scattering from ion tracks could be detected in apatite. A two stage activation energy can be explained in terms of the relaxation of the material followed by the recrystallisation of the damage.

Analysis of the SAXS data from the *ex situ* annealing of ion tracks in olivine indicated that unlike apatite, tracks in olivine resist much higher temperatures and even at 800 °C, there is a clear signal from the tracks in the SAXS images. However, at temperatures above ∼600 °C, fragmentation of the tracks is evident from the scattering signal. At temperatures close to 1000 °C oxidation of olivine might also be present. Using an Arrhenius plot for the track radii extracted from the *ex situ* annealing of the tracks up to ∼600 °C, an activation energy of 0.40±0.04 eV was calculated for the recrystallisation of the damage in olivine.

In conclusion, the results of this work represent a valuable contribution to the understanding of the morphology and annealing behavior of swift heavy ion tracks in the three crystalline solids. It has been demonstrated that synchrotron SAXS is well suited for measuring track radii with very high precision and capable of resolving even subtle changes in the electron density of the track damage compared to the matrix. Combining SAXS with *in situ* and *ex situ* annealing experiments enables studying the full annealing kinetics of un-etched ion tracks and calculation of the relevant activation energies for the damage recovery processes that have not been achievable by other means. SAXS thus becomes an important technique for a richer understanding of swift heavy ion tracks. During the course of the project, ion tracks in many other materials have been successfully measured including metallic glasses, polymers, and oxide materials.

6.1 Future directions

Studying ion tracks with respect to crystallographic orientation of the target material

During fission-track formation, the random decay direction induces tracks of different crystallographic orientations, which may additionally modify the radiation damage. Orientation effects are not only important during track formation, but also affect the thermal annealing behavior of tracks at elevated temperatures [218, 256]. The high accuracy with which SAXS can determine track radii is well suited for studying tracks generated normal to different crystallographic planes and investigating the possible difference in damage recovery. Preliminary results of SAXS measurement of ion track radii in apatite and quartz generated with respect to different crystallographic orientation indeed show the differences are present.

SAXS investigation of the morphology and annealing behavior of ion tracks in other materials

In addition to apatite, there are other geologically important minerals such as zircon and sphene that have applications for fission track dating. Systematic investigation of ion tracks using SAXS can be performed to study the nm-sized un-etched damage and their dependence on relevant geological environment in these minerals. Investigation of the ion-track morphology and annealing behavior in different compositions of apatite (e.g. Strontium-apatite and calcium apatite) has already started and results indicate a difference in the radius as well as resistivity of the tracks to annealing. Moreover, as SAXS is capable of measuring subtle density changes that often happen in the track damage in both crystalline and amorphous materials, it can be used for identifying tracks in materials that were not known before to be sensitive to track formation, due to the lack of suitable measurement techniques.

Studying the effect of pressure and temperature on ion tracks

Under some conditions, such as during uplift of deep crustal rocks to the surface, tracks in minerals are exposed to elevated pressures [257]. The influence of pressure on the stability and annealing behavior of fission tracks has been a controversial issue [257, 258, 259]; however, no final picture on the role of pressure has been achieved so far, and there are just a few, but inconsistent, experimental results at elevated pressures and temperatures for etched tracks. First measurements have indicated that irradiation under high-pressure yields reduced track radii. Furthermore, *in situ* SAXS measurements of the track radius under pressure (where the tracks are formed at room pressure) showed a change in the track radius at elevated pressures, however, after release of the pressure the track radius returned to its original value. SAXS enables *in situ* measurement of ion tracks under elevated pressures in diamond anvil cells. Their stability can also be investigated by simultaneous combination of pressure and temperature to simulate the conditions experienced by fission tracks in the earth's crust.

SAXS modeling of ion tracks in 2D

The current method of SAXS data analysis involves extracting data from the scattering images and fitting the one dimensional data in order to model the radial density profile of the ion tracks. Examples of 2D simulation of scattering from ion tracks are shown in chapter 3. As the scattering intensities from SAXS measurements are recorded in two dimensions, improvement of the 2D simulation of the SAXS images can lead to a more comprehensive understanding of the ion-track morphology and ultimately implementation of the models for fitting the data in 2D and eliminate the need for masking of the scattering intensities performed currently.

Bibliography

[1] Wagner, G. A. & Van den haute, P. Fission track dating. *Kluwer Academic Publishers* (1992).

[2] Weber, W. J., Ewing, R. C. & Wang, L. M. The radiation-induced crystalline-to-amorphous transition in zircon. *Journal of Materials Research* **9**, 688–698 (1994).

[3] Ewing, R. C., Meldrum, A., Wang, L. M., Weber, W. J. & Corrales, L. R. Radiation effects in zircon. *Zircon* **53**, Mineral Soc Amer (2003).

[4] Gallagher, K., Brown, R. & Johnson, C. Fission track analysis and its applications to geological problems. *Annual Review of Earth and Planetary Sciences* **26**, 519–572 (1998).

[5] Price, P. B. & Walker, R. M. Fossil tracks of charged particles in mica and age of minerals. *Journal of Geophysical Research* **68**, 4847 (1963).

[6] Fleischer, R. L., Price, P. B. & Walker, R. M. Nuclear tracks in solids: Principles and applications. *University of California Press, Berkeley* (1975).

[7] Naeser, C. W. Fission track dating. *U.S. Geological Survey* (1978).

[8] Wagner, G. A. Fission track dating of apatites. *Earth and Planetary Science Letters* **4**, 411 (1968).

[9] Tagami, T. Zircon fission-track thermochronology and applications to fault studies. *Low-temperature Thermochronology: Techniques, Interpretations, and Applications* **58**, 95–122 (2005).

[10] Gleadow, A. J. W., Belton, D. X., Kohn, B. P. & Brown, R. W. Fission track dating of phosphate minerals and the thermochronology of apatite. *Phosphates: Geochemical, Geobiological, and Materials Importance* **48** (2002).

[11] Tagami, T. & O'Sullivan, P. B. Fundamentals of fission-track thermochronology. *Low-temperature Thermochronology: Techniques, Interpretations, and Applications* **58**, 19–47 (2005).

[12] Silk, E. C. H. & Barnes, R. S. Examination of fission fragment tracks with an electron microscope. *Philosophical Magazine* **4**, 970–972 (1959).

[13] Price, P. B. & Zinner, E. Robert M . Walker 1929-2004 (a biographical memoir). *The National Academies Press* (2005).

[14] Price, P. B. & Walker, R. M. Electron microscope observation of a radiation-nucleated phase transformation in mica. *Journal of Applied Physics* **33**, 2625 (1962).

[15] Reiners, P. W. & Shuster, D. L. Thermochronology and landscape evolution. *Physics Today* **62**, 31–36 (2009).

[16] *http://www.geo.arizona.edu/ reiners/GleadowFTSCslides.pdf* .

[17] Price, P. B. & Walker, R. M. Chemical etching of charged-particle tracks in solids. *Journal of Applied Physics* **33**, 3407 (1962).

[18] Li, W., Wang, L., Lang, M., Trautmann, C. & Ewing, R. C. Thermal annealing mechanisms of latent fission tracks: Apatite vs. zircon. *Earth and Planetary Science Letters* **302**, 227–235 (2011).

[19] Perelygin, V. P. *et al.* On search and identification of short-lived super heavy cosmic-ray nuclei ($Z \geq 110$) by fossil track study of the extraterrestrial crystals: Results and perspectives. *Nuclear Physics A* **718** (2003).

[20] Farid, S. M. Annealing of Xe$^{54}_{32}$-ion tracks in a soda glass track detector. *International Journal of Applied Radiation and Isotopes* **36**, 455–462 (1985).

[21] Hurford, A. J. & Green, P. F. The zeta-age calibration of fission-track dating. *Isotope Geoscience* **1**, 285–317 (1983).

[22] Gleadow, A. J. W., Duddy, I. R., Green, P. F. & Lovering, J. F. Confined fission-track lengths in apatite - a diagnostic-tool for thermal history analysis. *Contributions To Mineralogy and Petrology* **94**, 405–415 (1986).

[23] Donelick, R. A., O'Sullivan, P. B. & Ketcham, R. A. Apatite fission-track analysis. *Low-temperature Thermochronology: Techniques, Interpretations, and Applications* **58**, 49–94 (2005).

[24] Price, P. B. & Walker, R. *Molecular sieves and methods for producing same, United states Patent Office* **3303085** (1967).

[25] Apel, P. Swift ion effects in polymers: industrial applications. *Nuclear Instruments and Methods In Physics Research Section B-beam Interactions With Materials and Atoms* **208**, 11–20 (2003).

[26] Ensinger, W., Sudowe, R., Brandt, R. & Neumann, R. Gas separation in nanoporous membranes formed by etching ion irradiated polymer foils. *Radiation Physics and Chemistry* **79**, 204–207 (2010).

[27] Toimil-Molares, M. E., Buschmann, V., Dobrev, D., Neumann, R., Scholz, R., Schuchert, I. U. & Vetter, J. Single-crystalline copper nanowires produced by electrochemical deposition in polymeric ion track membranes. *Advanced Materials* **13**, 62 (2001).

[28] Spohr, R. Status of ion track technology - prospects of single tracks. *Radiation Measurements* **40**, Int Nucl Track Soc; Grup Fis Radiac (2005).

[29] Dobrev, D., Vetter, J., Angert, N. & Neumann, R. Electrochemical growth of copper single crystals in pores of polymer ion-track membranes. *Applied Physics A-materials Science and Processing* **69**, 233–237 (1999).

[30] Thornell, G., Spohr, R., van Veldhuizen, E. J. & Hjort, K. Micromachining by ion track lithography. *Sensors and Actuators A-physical* **73**, 176–183 (1999).

[31] Chandler, P. J., Lama, F. L., Townsend, P. D. & Zhang, L. Buried double wave-guide by ion-implantation in quartz. *Applied Physics Letters* **53**, 89–91 (1988).

[32] Hjort, K., Thornell, G., Spohr, R. & Schweitz, J. A. Heavy ion induced etch anisotropy in single crystalline quartz. *Ninth Annual International Workshop On Micro Electro Mechanical Systems, Ieee Proceedings: An Investigation of Micro Structures, Sensors, Actuators, Machines and Systems* (1996).

[33] Hjort, K., Thornell, G., Schweitz, J. A. & Spohr, R. Quartz micromachining by lithographic control of ion track etching. *Applied Physics Letters* **69**, 3435–3436 (1996).

[34] Fleischer, R. L., Hart, H. R. & Giard, W. R. Particle track identification - application of a new technique to apollo helmets. *Science* **170**, 1189 (1970).

[35] Fleischer, R. L., Alter, H. W., Walker, R. M., Furman, S. C. & Price, P. B. Particle track etching. *Science* **178**, 255– (1972).

[36] Comstock, G. M., Fleische, R. L., Giard, W. R., Hart, H. R., Nichols, G. E. & Price, P. B. Cosmic-ray tracks in plastics - apollo helmet dosimetry experiment. *Science* **172**, 154 (1971).

[37] Perron, C. Relativistic u-238 ion tracks in olivine and cosmic-ray track studies. *Nature* **310**, 397–399 (1984).

[38] Young, D. A. Etching of radiation damage in lithium fluoride. *Nature* **182**, 375–377 (1958).

[39] Fleischer, R. L., Price, P. B., Walker, R. M. & Hubbard, E. L. Track registration in various solid-state nuclear track detectors. *Physical Review A-general Physics* **133**, 1443 (1964).

[40] Spohr, R. Ion tracks and microtechnology: Principles and applications. *Friedrich Vieweg and Sohn Verlagsgesellschaft MBH* (1990).

[41] Awazu, K., Ishii, S., Shima, K., Roorda, S. & Brebner, J. L. Structure of latent tracks created by swift heavy-ion bombardment of amorphous SiO_2. *Physical Review B* **62**, 3689–3698 (2000).

[42] Follstaedt, D. M., Norman, A. K., Doyle, B. L. & McDaniel, F. D. Strain fields around high-energy ion tracks in alpha-quartz. *Journal of Applied Physics* **100**, 064306 (2006).

[43] Li, W., Wang, L., Sun, K., Lang, M., Trautmann, C. & Ewing, R. C. Porous fission fragment tracks in fluorapatite. *Physical Review B* **82**, 144109 (2010).

[44] Lang, M., Lian, J., Zhang, F., Hendriks, B. W. H., Trautmann, C., Neumann, R. & Ewing, R. C. Fission tracks simulated by swift heavy ions at crustal pressures and temperatures. *Earth and Planetary Science Letters* **274**, 355–358 (2008).

[45] Wiesner, J., Traeholt, C., Wen, J. G., Zandbergen, H. W., Wirth, G. & Fuess, H. High resolution electron microscopy of heavy-ion induced defects in superconducting Bi-2212 thin films in relation to their effect on J_c. *Physica C* **268**, 161–172 (1996).

[46] Afra, B., Lang, M., Rodriguez, M. D., Zhang, J., Giulian, R., Kirby, N., Ewing, R. C., Trautmann, C., Toulemonde, M. & Kluth, P. Annealing kinetics of latent particle tracks in durango apatite. *Physical Review B* **83**, 064116 (2011).

[47] Afra, B. *et al.* SAXS investigations of the morphology of swift heavy ion tracks in alpha-quartz. *Journal of physics. Condensed matter* **25**, 045006–045006 (2013).

[48] Meftah, A., Brisard, F., Costantini, J. M., Dooryhee, E., Hageali, M., Hervieu, M., Stoquert, J. P., Studer, F. & Toulemonde, M. Track formation in SiO_2 quartz and the thermal-spike mechanism. *Physical Review B* **49**, 12457–12463 (1994).

[49] Ramos, S. M. M., Clerc, C., Canut, B., Chaumont, J., Toulemonde, M. & Bernas, H. Damage kinetics in MeV gold ion - irradiated crystalline quartz. *Nuclear Instruments and Methods In Physics Research Section B-beam Interactions With Materials and Atoms* **166** (2000).

[50] Villa, F., Grivet, M., Rebetez, M., Dubois, C., Chambaudet, A., Chevarier, N., Blondiaux, G., Sauvage, T. & Toulemonde, M. Damage morphology of Kr ion tracks in apatite: Dependence on thermal annealing. *Nuclear Instruments and Methods In Physics Research Section B-beam Interactions With Materials and Atoms* **168**, 72–77 (2000).

[51] Thibaudau, F., Cousty, J., Balanzat, E. & Bouffard, S. Atomic-force-microscopy observations of tracks induced by swift Kr ions in mica. *Physical Review Letters* **67**, 1582–1585 (1991).

[52] Khalfaoui, N., Rotaru, C. C., Bouffard, S., Jacquet, E., Lebius, H. & Toulemonde, M. Study of swift heavy ion tracks on crystalline quartz surfaces. *Nuclear Instruments and Methods In Physics Research Section B-beam Interactions With Materials and Atoms* **209**, 165–169 (2003).

[53] Trautmann, C., Toulemonde, M., Schwartz, K., Costantini, J. M. & Muller, A. Damage structure in the ionic crystal lif irradiated with swift heavy ions. *Nuclear Instruments and Methods In Physics Research Section B-beam Interactions With Materials and Atoms* **164**, 365–376 (2000).

[54] Guinier, A. & Fournet, G. Small-angle scattering of x-rays. *New York: Wiley* (1955).

[55] Glatter, O. & Kratky, O. Small angle x-ray scattering. *London: Academic* (1982).

[56] Narayanan, T. High brilliance small-angle x-ray scattering applied to soft matter. *Curr. Opin. Colloid Interface Sci* **14**, 409–15 (2009).

[57] Changizi, V., Oghabian, M. A., Speller, R., Sarkar, S. & Kheradmand, A. A. Application of small angle x-ray scattering (SAXS) for differentiation between normal and cancerous breast tissue. *International journal of medical sciences* **2**, 118–21 (2005).

[58] Jensen, T. H., Bech, M., Bunk, O., Thomsen, M., Menzel, A., Bouchet, A., Le Duc, G., Feidenhans'l, R. & Pfeiffer, F. Brain tumor imaging using small-angle x-ray scattering tomography. *Physics In Medicine and Biology* **56**, 1717–1726 (2011).

[59] Hubbard, A. Encyclopedia of surface and colloid science. *CRC Press* (2002).

[60] Lifshin, E. X-ray characterization of materials. *Wiley-VCH* (1999).

[61] Liu, X. X., Yin, J. H., Sun, D. B., Bu, W. B., Cheng, W. D. & Wu, Z. H. Small-angle x-ray scattering study on nanostructures of polyimide films. *Chinese Physics Letters* **27**, 096103 (2010).

[62] Trinkaus, H. Anisotropic creep and growth of amorphous solids under swift heavy ion bombardment: An asymptotic thermal spike approach. *Nuclear Instruments and Methods In Physics Research Section B-beam Interactions With Materials and Atoms* **107** (1996).

[63] Kluth, P. *et al.* Fine structure in swift heavy ion tracks in amorphous SiO_2. *Physical Review Letters* **101**, 175503 (2008).

[64] Crowley, K., Cameron, M. & Schaefer, R. L. Experimental studies of annealing of etched fission tracks in fluorapatite. *Geochim. Cosmochim. Acta* **55**, 1449–1465 (1991).

[65] Gleadow, A., Duddy, I., Green, P. & Lovering, J. Confined fission track lengths in apatite: a diagnostic tool for thermal history analysis. *Contrib. Mineral. Petrol.* **94**, 405–415. (1986).

[66] Ewing, R. Nuclear waste forms for actinides. *Proc. Natl. Acad. Sci. U. S. A.* **96**, 3432–3439 (1999).

[67] Ewing, R., Weber, W. & Lian, J. Nuclear waste disposal-pyrochlore ($A_2B_2O_7$): Nuclear waste form for the immobilization of plutonium and minor actinides. *J. Appl. Phys.* **95**, 5949–5971 (2004).

[68] Murakami, T., Chakoumakos, B., Ewing, R., Limpkin, G. & Weber, W. Alpha-decay event damage in zircon. *Am. Mineral.* **76**, 1510 (1991).

[69] Dodd, P. & Massengill, L. Basic mechanisms and modeling of single-event upset in digital microelectronics. *IEEE Trans. Nucl. Sci.* **50**, 583 (2003).

[70] Mara, A., Siwy, Z., Trautmann, C., Wan, J. & Kamme, F. An asymmetric polymer nanopore for single molecule detection. *Nano Lett.* **4**, 497–501 (2004).

[71] Toulemonde, M., Trautmann, C., Balanzat, E., Hjort, K. & Weidinger, A. Track formation and fabrication of nanostructures with mev-ion beams. *Nucl. Instrum. Methods Phys. Res., Sect. B* **216**, 1–8 (2004).

[72] Whitney, T., Jiang, J., Searson, P. & Chien, C. Fabrication and magnetic properties of arrays of metallic nanowires. *Science* **261**, 1316–1319 (1993).

[73] Miller, D. & Wagner, G. Fission-track ages applied to obsidian artifacts from south america using the plateau-annealing and the track-size age-correction techniques. *Nuclear Tracks* **5**, 147–155 (1981).

[74] Brill, R. H., Fleischer, R. L., Price, P. B. & Walker, R. M. The fission-track dating of man-made glasses. Schenectady General Electric Company Research Laboratory (N.Y.) (1964).

[75] Palumbo, F., Main, I. G. & Zito, G. The thermal evolution of sedimentary basins and its effect on the maturation of hydrocarbons. *Geophys. J. Int.* **139**, 248–260 (1999).

[76] Nastasi, M., Mayer, J. & Hirvonen, J. K. Ion-solid interactions: Fundamentals and applications. *Cambridge University Press* (1996).

[77] Burcham, W. E. Elements of nuclear physics. *Longman Group Ltd.* (1979).

[78] Lindhard, J., Scharff, M. & Shitt, H. E. Range concepts and heavy ion ranges. *Matematisk-fysiske Meddelelser Det Kongelige Danske Videnskabernes Selskab* **33** (1963).

[79] Ziegler, J. F., Biersack, J. P. & Littmark, U. The stopping and range of ions in matter, vol 1. *Pergamon Press, New York* (1985).

[80] Ziegler, J. F. The stopping and range of ions in matter. *http://www.srim.org/* (2008).

[81] Kinchin, G. H. & Pease, R. S. The displacement of atoms in solids by radiation. *Reports On Progress In Physics* **18**, 1–51 (1955).

[82] Primak, W. Threshold for radiation effects in silica. *Physical Review B* **6**, 4846–4851 (1972).

[83] Robinson, M. T. The binary collision approximation - background and introduction. *Radiation Effects and Defects In Solids* **130**, 3–20 (1994).

[84] Averback, R. S. & de la Rubia, T. D. Displacement damage in irradiated metals and semiconductors. *Solid State Physics* **51**, 281–402 (1998).

[85] Seitz, F. & Koehler, J. S. Displacement of atoms during irradiation. *Solid State Physics-advances In Research and Applications* **2**, 305–448 (1956).

[86] Hines, R. L. & Arndt, R. Radiation effects of bombardment of quartz and vitreous silica by 7.5-kev to 59-kev positive ions. *Physical Review* **119**, 623–633 (1960).

[87] Biersack, J. P. & Haggmark, L. G. A monte-carlo computer-program for the transport of energetic ions in amorphous targets. *Nuclear Instruments and Methods* **174**, 257–269 (1980).

[88] Sigmund, P. & Schinner, A. Binary theory of electronic stopping. *Nuclear Instruments and Methods In Physics Research Section B-beam Interactions With Materials and Atoms* **195** (2002).

[89] Toulemonde, M., Assmann, W., Dufour, C., Meftah, A., Studer, F. & Trautmann, C. Experimental phenomena and thermal spike model description of ion tracks in amorphisable inorganic insulators. *Ion Beam Science: Solved and Unsolved Problems, Pts 1 and 2* **52**, Danish Nat Sci Res Council; Carlsberg Fdn (2006).

[90] Bethe, H. & Ashkin, J. Experimental nuclear physics. *New York* (1953).

[91] Schiwietz, G., Czerski, K., Roth, M., Staufenbiel, F. & Grande, P. L. Femtosecond dynamics - snapshots of the early ion-track evolution. *Nuclear Instruments and Methods In Physics Research Section B-beam Interactions With Materials and Atoms* **226**, 682–704 (2004).

[92] Johnson, R. E. & Brown, W. L. Electronic mechanisms for sputtering of condensed-gas solids by energetic ions. *Nuclear Instruments and Methods In Physics Research* **198**, 103–118 (1982).

[93] Leuseur, D. & Dunlop, A. Damage creation via electronic excitations in metallic targets .2. a theoretical-model. *Radiation Effects and Defects In Solids* **126** (1993).

[94] Stampfli, P. & Bennemann, K. H. Time-dependence of the laser-induced femtosecond lattice instability of si and gaas - role of longitudinal optical distortions. *Physical Review B* **49**, 7299–7305 (1994).

[95] Watson, C. C. & Tombrello, T. A. A modified lattice potential model of electronically mediated sputtering. *Radiation Effects* **89**, 263–283 (1985).

[96] Wang, Z. G., Dufour, C., Paumier, E. & Toulemonde, M. The Se sensitivity of metals under swift-heavy-ion irradiation - a transient thermal-process. *Journal of Physics-condensed Matter* **6**, 6733–6750 (1994).

[97] Szenes, G. Thermal spike model of amorphous track formation in insulators irradiated by swift heavy ions. *Nuclear Instruments and Methods In Physics Research Section B-beam Interactions With Materials and Atoms* **116** (1996).

[98] Ritchie, R. H. & Claussen, C. A core plasma model of charged-particle track formation in insulators. *Nuclear Instruments and Methods In Physics Research* **198**, 133–138 (1982).

[99] Toulemonde, M., Bouffard, S. & Studer, F. Swift heavy-ions in insulating and conducting oxides - tracks and physical-properties. *Nuclear Instruments and Methods In Physics Research Section B-beam Interactions With Materials and Atoms* **91**, 108–123 (1994).

[100] Schenkel, T., Hamza, A. V., Barnes, A. V., Schneider, D. H., Banks, J. C. & Doyle, B. L. Ablation of gaas by intense, ultrafast electronic excitation from highly charged ions. *Physical Review Letters* **81**, 2590–2593 (1998).

[101] Levalois, M., Bogdanski, P. & Toulemonde, M. Induced damage by high-energy heavy-ion irradiation at the ganil accelerator in semiconductor-materials. *Nuclear Instruments and Methods In Physics Research Section B-beam Interactions With Materials and Atoms* **63** (1992).

[102] Wesch, W., Kamarou, A. & Wendler, E. Effect of high electronic energy deposition in semiconductors. *Nuclear Instruments and Methods In Physics Research Section B-beam Interactions With Materials and Atoms* **225**, 111–128 (2004).

[103] Barbu, A., Dunlop, A., Lesueur, D. & Averback, R. S. Latent tracks do exist in metallic materials. *Europhysics Letters* **15**, 37–42 (1991).

[104] Dufour, C., Audouard, A., Beuneu, F., Dural, J., Girard, J. P., Hairie, A., Levalois, M., Paumier, E. & Toulemonde, M. A high-resistivity phase induced by swift heavy-ion irradiation of bi - a probe for thermal spike damage. *Journal of Physics-condensed Matter* **5**, 4573–4584 (1993).

[105] Dunlop, A. & Lesueur, D. Damage creation via electronic excitations in metallic targets .1. experimental results. *Radiation Effects and Defects In Solids* **126** (1993).

[106] Meftah, A., Costantini, J. M., Khalfaoui, N., Boudjadar, S., Stoquert, J. P., Studer, F. & Toulemonde, M. Experimental determination of track cross-section in $Gd_3Ga_5O_{12}$ and comparison to the inelastic thermal spike model applied to several materials. *Nuclear Instruments and Methods In Physics Research Section B-beam Interactions With Materials and Atoms* **237**, 563–574 (2005).

[107] Li, W., Lang, M., Gleadow, A. J. W., Zdorovets, M. V. & Ewing, R. C. Thermal annealing of unetched fission tracks in apatite. *Earth and Planetary Science Letters* **321**, 121–127 (2012).

[108] Sigrist, A. & Balzer, R. Formation of track in crystals. *Helvetica Physica Acta* **50**, 49–64 (1977).

[109] Trautmann, C., Boccanfuso, M., Benyagoub, A., Klaumunzer, S., Schwartz, K. & Toulemonde, M. Swelling of insulators induced by swift heavy ions. *Nuclear Instruments and Methods In Physics Research Section B-beam Interactions With Materials and Atoms* **191**, 144–148 (2002).

[110] Waligorski, M. P. R., Hamm, R. N. & Katz, R. The radial-distribution of dose around the path of a heavy-ion in liquid water. *Nuclear Tracks and Radiation Measurements* **11**, 309–319 (1986).

[111] Vineyard, G. H. Thermal spikes and activated processes. *Radiation Effects* **29**, 245–248 (1976).

[112] Toulemonde, M., Dufour, C., Meftah, A. & Paumier, E. Transient thermal processes in heavy ion irradiation of crystalline inorganic insulators. *Nuclear Instruments & Methods In Physics Research Section B-beam Interactions With Materials and Atoms* **166** (2000).

[113] Dufour, C., Wang, Z. G., Paumier, E. & Toulemonde, M. Transient thermal process induced by swift heavy ions: Defect annealing and defect creation in Fe and Ni. *Bulletin of Materials Science* **22**, 671–677 (1999).

[114] Dufour, C., Khomenkov, V., Rizza, G. & Toulemonde, M. Ion-matter interaction: the three-dimensional version of the thermal spike model. application to nanoparticle irradiation with swift heavy ions. *Journal of Physics D-applied Physics* **45**, 065302 (2012).

[115] Mizutani, U. Introduction to the electron theory of metals. *Cambridge University Press* 604 (2001).

[116] Tritt, T. M. Thermal conductivity: Theory, properties, and applications, physics of solids and liquids. *Springer* (2005).

[117] Lozano, F. M. *Thermal Conductivity and specific heat measurements for power electronics packaging materials.* Ph.D. thesis, Universitat Autonoma de Barcelona (2005).

[118] Caron, M., Rothard, H., Toulemonde, M., Gervais, B. & Beuve, M. Theoretical and experimental study of electronic temperatures in heavy ion tracks from auger electron spectra and thermal spike calculations. *Nuclear Instruments and Methods In Physics Research Section B-beam Interactions With Materials and Atoms* **245**, 36–40 (2006).

[119] Allen, P. B. Theory of thermal relaxation of electrons in metals. *Physical Review Letters* **59**, 1460–1463 (1987).

[120] Baranov, I. A., Martynenko, Y. V., Tsepelevich, S. O. & Yavlinskii, Y. N. Inelastic sputtering of solids by ions. *Uspekhi Fizicheskikh Nauk* **156**, 477–511 (1988).

[121] Dale, A. E. & Gary, S. W. Thermal spike model of ion-induced grain growth. In *MRS Proceedings*, vol. 202 (1990).

[122] Amirkhanov, I. V., Didyk, A. Y., Muzafarov, D. Z., Puzynin, I. V., Puzynina, T. P., Sarkar, N. R., Sarkhadov, I. & Sharipov, Z. A. Application of the thermal spike model for explanation of variations of surface structure of highly oriented pyrolytic graphite under bombardment by ^{86}Kr and ^{209}Bi fast ions with high ionization energy loss. *Journal of Surface Investigation. X-ray, Synchrotron and Neutron Techniques* **2**, 331–339 (2008).

[123] Fleischer, R. L., Price, P. B. & Walker, R. M. Ion explosion spike mechanism for formation of charged-particle tracks in solids. *Journal of Applied Physics* **36**, 3645 (1965).

[124] Schiwietz, G., Luderer, E., Xiao, G. & Grande, P. L. Energy dissipation of fast heavy ions in matter. *Nuclear Instruments and Methods In Physics Research Section B-beam Interactions With Materials and Atoms* **175**, Inst Fis UFRGS, Ion Implantat Lab (2001).

[125] Pakarinen, O. H., Djurabekova, F., Nordlund, K., Kluth, P. & Ridgway, M. C. Molecular dynamics simulations of the structure of latent tracks in quartz and amorphous SiO_2. *Nuclear Instruments and Methods In Physics Research Section B-beam Interactions With Materials and Atoms* **267**, 1456–1459 (2009).

[126] Toulemonde, M., Paumier, E. & Dufour, C. Thermal spike model in the electronic stopping power regime. *Radiation Effects and Defects In Solids* **126** (1993).

[127] Urbassek, H. M., Kafemann, H. & Johnson, R. E. Atom ejection from a fast-ion track - a molecular-dynamics study. *Physical Review B* **49**, 786–795 (1994).

[128] R, M. & Adams, C. T. Close to universal negative-ion source. *Nuclear Instruments and Methods* **118**, 329–336 (1974).

[129] Middleton, R. Survey of negative-ion sources for tandem accelerators. *Nuclear Instruments and Methods* **122**, 35–43 (1974).

[130] Betz, H. D. Charge states and charge-changing cross-sections of fast heavy-ions penetrating through gaseous and solid media. *Reviews of Modern Physics* **44**, 465 (1972).

[131] Dyson, N. A. X-rays in atomic and nuclear physics (1990).

[132] Pavlinsky, G. V. Fundamentals of x-ray physics (2008).

[133] Rohlsberger, R. Nuclear condensed matter physics with synchrotron radiation: Basic principles, methodology and applications. *Springer Verlag* (2005).

[134] Wiedemann, H. *Particle Accelerator Physics* (Springer, 1999).

[135] Raubenheimer, T. O. Tolerances to limit the vertical emittance in future storage rings. *Particle Accelerators* **36**, 75–119 (1991).

[136] Hubbell, J. H., Veigele, W. J., Briggs, E. A., Brown, R. T., Cromer, D. T. & Howerton, R. J. Atomic form factors, incoherent scattering functions, and photon scattering cross sections. *Journal of Physical and Chemical Reference Data* **4**, 471 (1975).

[137] Hubbell, J. H. & Overbo, I. Relativistic atomic form-factors and photon coherent scattering cross-sections. *Journal of Physical and Chemical Reference Data* **8**, 69–105 (1979).

[138] Warren, B. E. X-ray diffraction. *Courier Dover Publications* (1969).

[139] Feigin, L. A. & Svergun, D. I. Structre analysis by small-angle x-ray and neutron scattering. *Plenum Press, New York* (1987).

[140] Engel, M., Stuehn, B., Schneider, J. J., Cornelius, T. & Naumann, M. Small-angle x-ray scattering (SAXS) off parallel, cylindrical, well-defined nanopores: from random pore distribution to highly ordered samples. *Applied Physics A-materials Science and Processing* **97**, 99–108 (2009).

[141] Russell, T. P., Lin, J. S., Spooner, S. & Wignall, G. D. Intercalibration of small-angle x-ray and neutron scattering data. *Journal of applied crystallography* **21**, 629–638 (1988).

[142] Dreiss, C. A., Jack, K. S. & Parker, A. P. On the absolute calibration of bench-top small-angle x-ray scattering instruments: a comparison of different standard methods. *Journal of Applied Crystallography* **39**, 32–38 (2006).

[143] Soontaranon, S. & Rugmai, S. Small angle x-ray scattering at siam photon laboratory. *Chinese journal of physics* **50**, 204–210 (2012).

[144] Katz, L. Absolute intensity measurements of small angle x-ray scattering. *University of Wisconsin–Madison* (1959).

[145] Ilavsky, J. & Jemian, P. R. Irena: tool suite for modeling and analysis of small angle scattering. *Journal of Applied Crystallography* **42**, 347–353 (2009).

[146] Wavemetrics. Igor pro 6. *http://www.wavemetrics.com/* .

[147] Afra, B., Rodriguez, M. D., Lang, M., Ewing, R. C., Kirby, N., Trautmann, C. & Kluth, P. Saxs study of ion tracks in San Carlos olivine and Durango apatite. *Nuclear Instruments and Methods In Physics Research Section B-beam Interactions With Materials and Atoms* **286**, 243–246 (2012).

[148] Rodriguez, M. D., Afra, B., Trautmann, C., Toulemonde, M., Bierschenk, T., Leslie, J., Giulian, R., Kirby, N. & Kluth, P. Morphology of swift heavy ion tracks in metallic glasses. *Journal of Non-crystalline Solids* **358**, 571–576 (2012).

[149] Eyal, Y. & Saleh, S. A. Structure model and small-angle scattering cross sections of latent ion tracks in dielectric solids. *J. Appl. Cryst.* **40**, 71–76 (2007).

[150] Sosman, R. The phases of silica. *Rutgers University Press, New Brunswick, New Jersey* (1965).

[151] Megaw, H. D. Crystal structures: a working approach. *Saunders* (1973).

[152] Lager, G. A., Jorgensen, J. D. & Rotella, F. J. Crystal-structure and thermal-expansion of alpha-quartz SiO_2 at low-temperatures. *Journal of Applied Physics* **53**, 6751–6756 (1982).

[153] Lide, D. R. CRC handbook of chemistry and physics 2004-2005: A ready-reference book of Chemical and Physical Data. *CRC Press I LLC* 2712 (2004).

[154] Fan, X. D., Peng, J. L. & Bursill, L. A. Joint density of states of wide-band-gap materials by electron energy loss spectroscopy. *Modern Physics Letters B* **12**, 541–554 (1998).

[155] Liu, X. M., Wang, S. J. & Zhang, F. Fission track dating of authigenic quartz in red weathering crusts of carbonate rocks in guizhou province. *Acta Geologica Sinica-english Edition* **78**, 1136–1142 (2004).

[156] Gong, G. L., Li, S. H., Sun, W. D., Guo, F., Xia, B. & Lu, B. F. Quartz thermoluminescence - another potential paleo-thermometer for sedimentary basin thermal history. *Chinese Journal Of Geophysics (Acta Geophysica Sinica)* **53**, 103–112 (2010).

[157] Manzano-Santamaria, J., Olivares, J., Rivera, A. & Agullo-Lopez, F. Electronic damage in quartz (c-SiO_2) by MeV ion irradiations: Potentiality for optical waveguiding applications. *Nuclear Instruments and Methods In Physics Research Section B-beam Interactions With Materials and Atoms* **272**, 271–274 (2012).

[158] Thurston, R. N., Pierce, A. D. & Papadakis, E. P. Reference for modern instrumentation, techniques, and technology: Ultrasonic instruments and devices II: Ultrasonic instruments and devices ii. *Elsevier* **24** (1998).

[159] Walls, F. L. & Vig, J. R. Fundamental limits on the frequency stabilities of crystal-oscillators. *Ieee Transactions On Ultrasonics Ferroelectrics and Frequency Control* **42**, 576–589 (1995).

[160] Tombrello, T. A. Track damage and erosion of insulators by ion-induced electronic processes. *Nuclear Instruments and Methods In Physics Research Section B-beam Interactions With Materials and Atoms* **2**, 555–563 (1984).

[161] Trautmann, C., Costantini, J. M., Meftah, A., Schwartz, K., Stoquert, J. P. & Toulemonde, M. Swelling of SiO_2 quartz induced by energetic heavy ions. *Atomistic Mechanisms In Beam Synthesis and Irradiation of Materials* **504** (1998).

[162] Aframian, A. Track retaining properties ofquartz for high-temperature in-core neutron fluence measurements. *Radiation Effects and Defects In Solids* **33**, 95–100 (1977).

[163] Singh, L., Sandhu, A. S., Singh, S. & Virk, H. S. Etching and annealing kinetics of heavy-ion tracks in quartz crystal. *Nuclear Instruments and Methods In Physics Research Section B-beam Interactions With Materials and Atoms* **46** (1990).

[164] Sawamura, T., Baba, S. & Narita, M. Anisotropic annealing of fission fragments in synthetic quartz. *Radiation Measurements* **30**, 453–459 (1999).

[165] Szenes, G. Amorphous track formation in SiO_2. *Nuclear Instruments and Methods In Physics Research Section B-beam Interactions With Materials and Atoms* **122** (1997).

[166] Szenes, G., Paszti, F., Peter, A. & Popov, A. I. Tracks induced in TeO_2 by heavy ions at low velocities. *Nuclear Instruments and Methods In Physics Research Section B-beam Interactions With Materials and Atoms* **166** (2000).

[167] Pena-Rodriguez, O., Manzano-Santamaria, J., Rivera, A., Garcia, G., Olivares, J. & Agullo-Lopez, F. Kinetics of amorphization induced by swift heavy ions in alpha-quartz. *Journal of Nuclear Materials* **430** (2012).

[168] Toulemonde, M., Ramos, S. M. M., Bernas, H., Clerc, C., Canut, B., Chaumont, J. & Trautmann, C. MeV gold irradiation induced damage in alpha-quartz: Competition between nuclear and electronic stopping. *Nuclear Instruments and Methods In Physics Research Section B-beam Interactions With Materials and Atoms* **178**, E–MRS (2001).

[169] *http://www.mindat.org/min-3337.html* .

[170] Riedel, C. & Spohr, R. Statistical properties of etched nuclear tracks .1. analytical theory and computer-simulation. *Radiation Effects and Defects In Solids* **42**, 69–75 (1979).

[171] Kluth, P., Schnohr, C. S., Sprouster, D. J., Byrne, A. P., Cookson, D. J. & Ridgway, M. C. Measurement of latent tracks in amorphous SiO_2 using small angle x-ray scattering. *Nuclear Instruments and Methods In Physics Research Section B-beam Interactions With Materials and Atoms* **266** (2008).

[172] *http://www.gatan.com/imaging/dig-micrograph.php* .

[173] Nordlund, K. Parcas computer code. the main principles of the MD algorithms are presented by Nordlund 1998 and Ghaly 1999. The adaptive time step and electronic stopping algorithms are the same as Nordlund 1995 (2006).

[174] Watanabe, T., Yamasaki, D., Tatsumura, K. & Ohdomari, I. Improved interatomic potential for stressed Si, O mixed systems. *Applied Surface Science* **234**, 207–213 (2004).

[175] Samela, J., Nordlund, K., Popok, V. N. & Campbell, E. E. B. Origin of complex impact craters on native oxide coated silicon surfaces. *Physical Review B* **77**, 075309 (2008).

[176] Berendsen, H. J. C., Postma, J. P. M., Vangunsteren, W. F., Dinola, A. & Haak, J. R. Molecular-dynamics with coupling to an external bath. *Journal of Chemical Physics* **81**, 3684–3690 (1984).

[177] Studer, F., Houpert, C., Toulemonde, M. & Dartyge, E. Local environment of iron in heavy ion-irradiated amorphous magnetic oxides by mossbauer and x-ray absorption-spectroscopy. *Journal of Solid State Chemistry* **91**, 238–249 (1991).

[178] Spohr, R., Armbruster, P. & Schaupert, K. Structure and diffusion properties of latent ion tracks. *Radiation Effects and Defects In Solids* **110**, 27–31 (1989).

[179] Olivares, J., Garcia-Navarro, A., Garcia, G., Myndez, A. & Agullo-Lopez, F. Optical determination of three-dimensional nanotrack profiles generated by single swift-heavy ion impacts in lithium niobate. *Applied Physics Letters* **89**, 071923 (2006).

[180] Agullo-Lopez, F., Garcia, G. & Olivares, J. Lattice preamorphization by ion irradiation: Fluence dependence of the electronic stopping power threshold for amorphization. *Journal of Applied Physics* **97**, 093514 (2005).

[181] Rivera, A., Olivares, J., Garcia, G., Cabrera, J. M., Agullo-Rueda, F. & Agullo-Lopez, F. Giant enhancement of material damage associated to electronic excitation during ion irradiation: The case of $LiNbO_3$. *Physica Status Solidi A-applications and Materials Science* **206**, 1109–1116 (2009).

[182] Zhang, J., Lang, M., Ewing, R. C., Devanathan, R., Weber, W. J. & Toulemonde, M. Nanoscale phase transitions under extreme conditions within an ion track. *Journal of Materials Research* **25**, 1344–1351 (2010).

[183] Rutherford, A. M. & Duffy, D. M. The effect of electron-ion interactions on radiation damage simulations. *Journal of Physics-condensed Matter* **19**, 496201 (2007).

[184] Toulemonde, M., Assmann, W., Trautmann, C. & Gruner, F. Jetlike component in sputtering of lif induced by swift heavy ions. *Physical Review Letters* **88**, 057602 (2002).

[185] Bres, E. F., Hutchison, J. L., Senger, B., Voegel, J. C. & Frank, R. M. HREM study of irradiation damage in human dental enamel crystals. *Ultramicroscopy* **35**, 305–322 (1991).

[186] Hench, L. L. Bioceramics. *Journal of the American Ceramic Society* **81**, 1705–1728 (1998).

[187] McConnell, D. Apatite; its crystal chemistry, mineralogy, utilization, and geologic and biologic occurrences. *Applied mineralogy, Springer-Verlag* **5** (1973).

[188] Geron, C. A., Danneberger, T. K., Traina, S. J., Logan, T. J. & Street, J. R. The effects of establishment methods and fertilization practices on nitrate leaching from turfgrass. *Journal of Environmental Quality* **22**, 119–125 (1993).

[189] Ma, Q. Y., Logan, T. J., Traina, S. J. & Ryan, J. A. Effects of NO_3^-, Cl^-, F^-, SO_4^{2-} and CO_3^{2-} on Pb^{2+} immobilization by hydroxyapatite. *Environmental Science and Technology* **28**, 408–418 (1994).

[190] Ma, Q. Y., Traina, S. J., Logan, T. J. & Ryan, J. A. In-situ lead immobilization by apatite. *Environmental Science and Technology* **27**, 1803–1810 (1993).

[191] Rakovan, J., Reeder, R. J., Elzinga, E. J., Cherniak, D. J., Tait, C. D. & Morris, D. E. Structural characterization of U(VI) in apatite by x-ray absorption spectroscopy. *Environmental Science and Technology* **36**, 3114–3117 (2002).

[192] Young, E. J., Myers, A., Munson, E. L. & Conklin, N. M. Mineralogy and geochemistry of fluorapatite from Cerro de Mercado, Durango, Mexico. *US geological survey professional paper 650-D* D84–D93 (1969).

[193] Villa, F. *et al.* Damage morphology of Kr ion tracks in apatite: Dependence on dE/dx. *Radiation Measurements* **31**, 65–70 (1999).

[194] Rabone, J. A. L., Carter, A., Hurford, A. J. & de Leeuw, N. H. Modelling the formation of fission tracks in apatite minerals using molecular dynamics simulations. *Physics and Chemistry of Minerals* **35**, 583–596 (2008).

[195] Tisserand, R., Rebetez, M., Grivet, M., Bouffard, S., Benyagoub, A., Levesque, F. & Carpena, J. Comparative amorphization quantification of two apatitic materials irradiated with heavy ions using XRD and RBS results. *Nuclear Instruments and Methods In Physics Research Section B-beam Interactions With Materials and Atoms* **215**, 129–136 (2004).

[196] Bae, I. T., Zhang, Y., Weber, W. J., Ishimaru, M., Hirotsu, Y. & Higuchi, M. Ionization-induced effects in amorphous apatite at elevated temperatures. *Journal of Materials Research* **23**, 962–967 (2008).

[197] Meldrum, A., Wang, L. M. & Ewing, R. C. Electron-irradiation-induced phase segregation in crystalline and amorphous apatite: A tem study. *American Mineralogist* **82**, 858–869 (1997).

[198] Weikusat, C., Glasmacher, U. A., Schuster, B., Trautmann, C., Miletich, R. & Neumann, R. Raman study of apatite amorphised with swift heavy ions under various irradiation conditions. *Physics and Chemistry of Minerals* **38**, 293–303 (2011).

[199] Liu, J., Glasmacher, U. A., Lang, M., Trautmann, C., Voss, K. O., Neumann, R., Wagner, G. A. & Miletich, R. Raman spectroscopy of apatite irradiated with swift heavy ions with and without simultaneous exertion of high pressure. *Applied Physics A-materials Science and Processing* **91**, 17–22 (2008).

[200] Papike, J. J. Chemistry of the rock-forming silicates - ortho, ring, and single-chain structures. *Reviews of Geophysics* **25**, 1483–1526 (1987).

[201] Chapman, C. R. Space weathering of asteroid surfaces. *Annual Review of Earth and Planetary Sciences* **32**, 539–567 (2004).

[202] Hapke, B. Space weathering from mercury to the asteroid belt. *Journal of Geophysical Research-planets* **106**, 10039–10073 (2001).

[203] Pillinger, C. T. Solar-wind exposure effects in the Lunar Soil. *Reports On Progress In Physics* **42**, 897 (1979).

[204] Bradley, J. P. Chemically anomalous, preaccretionally irradiated grains in interplanetary dustfrom comets. *Science* **265**, 925–929 (1994).

[205] Sasaki, S., Nakamura, K., Hamabe, Y., Kurahashi, E. & Hiroi, T. Production of iron nanoparticles by laser irradiation in a simulation of lunar-like space weathering. *Nature* **410**, 555–557 (2001).

[206] Moroz, L. V., Fisenko, A. V., Semjonova, L. F., Pieters, C. M. & Korotaeva, N. N. Optical effects of regolith processes on S-asteroids as simulated by laser shots on ordinary chondrite and other mafic materials. *Icarus* **122**, 366–382 (1996).

[207] Kohlsledt, D. L. & Mackwell, S. J. High-temperature stability of San Carlos olivine. *Contributions To Mineralogy and Petrology* **95**, 226–230 (1987).

[208] Fleischer, R. L., Price, P. B., Walker, R. M., Maurette, M. & Morgan, G. Tracks of heavy primary cosmic rays in meteorites. *Journal of Geophysical Research* **72**, 355 (1967).

[209] Aleksandrov, A. B. *et al.* Technique for determining the charge of cosmic ray nuclei by tracks in olivine crystals from meteorites. *Bulletin of the Lebedev Physics Institute* **35**, 205–210 (2008).

[210] Aleksandrov, A. B. *et al.* Study of the charge distribution of galactic cosmic rays and search for superheavy nuclei traces in olivine crystals from meteorites. *Bulletin of the Lebedev Physics Institute* **35**, 276–285 (2008).

[211] Fleischer, R. L. & Price, P. B. Techniques for geological dating of minerals by chemical etching of fission fragment tracks. *Geochimica Et Cosmochimica Acta* **28**, 1705 (1964).

[212] Maurette, M., Pellas, P. & Walker, R. M. Cosmic-ray-induced particle tracks in meteorite. *Nature* **204**, 821 (1964).

[213] Ginzburg, V. L. What problems of physics and astrophysics seem now to be especially important and interesting. *Uspekhi Fizicheskikh Nauk* **169**, 419–441 (1999).

[214] Miro, S., Grebille, D., Chateigner, D., Pelloquin, D., Stoquert, J. P., Grob, J. J., Costantini, J. M. & Studer, F. X-ray diffraction study of damage induced by swift heavy ion irradiation in fluorapatite. *Nuclear Instruments and Methods In Physics Research Section B-beam Interactions With Materials and Atoms* **227**, 306–318 (2005).

[215] Ahrens, T. J., Fleischer, R. L., Price, P. B. & Woods, R. T. Erasure of fission tracks in glasses and silicates by shock waves. *Earth and Planetary Science Letters* **8**, 420 (1970).

[216] Gleadow, A. J. W. Anisotropic and variable track etching characteristics in natural sphenes. *Nuclear Track Detection* **2**, 105 (1978).

[217] Green, P. F. The relationship between track shortening and fission-track age reduction in apatite - combined influences of inherent instability, annealing anisotropy, length bias and system calibration. *Earth and Planetary Science Letters* **89**, 335–352 (1988).

[218] Green, P. F., Duddy, I. R., Gleadow, A. J. W., Tingate, P. R. & Laslett, G. M. Thermal annealing of fission tracks in apatite .1. a qualitative description. *Chemical Geology* **59**, 237–253 (1986).

[219] Paul, T. A. Transmission electron-microscopy investigation of unetched fission tracks in fluorapatite physical process of annealing. *Nuclear Tracks and Radiation Measurements* **21** (1993).

[220] Paul, T. A. & Fitzgerald, P. G. Transmission electron-microscopic investigation of fission tracks in fluorapatite. *American Mineralogist* **77**, 336–344 (1992).

[221] Damask, A. C. Point defects in metals. *Gordon and Breach, Science Publishers* (1963).

[222] Parkins, W. E., Dienes, G. J. & Brown, F. W. Pulse-annealing for the study of relaxation processes in solids. *Journal of Applied Physics* **22**, 1012–1019 (1951).

[223] Modgil, S. K. & Virk, H. S. Annealing of fission fragment tracks in inorganic solids. *Nuclear Instruments and Methods In Physics Research Section B-beam Interactions With Materials and Atoms* **12**, 212–218 (1985).

[224] Fertig, N., Blick, R. H. & Behrends, J. C. Whole cell patch clamp recording performed on a planar glass chip. *Biophysical Journal* **82**, 3056–3062 (2002).

[225] L'Annunziata, M. F. Handbook of radioactivity analysis. *Academic Press* (2012).

[226] Harbsmeier, F. & Bolse, W. Ion beam induced amorphization in alpha quartz. *Journal of Applied Physics* **83**, 4049–4054 (1998).

[227] Gasiorek, S., Dhar, S. & Lieb, K. P. Epitaxial recrystallization of rb-irradiated alpha-quartz during thermal annealing in air. *Nuclear Instruments and Methods In Physics Research Section B-beam Interactions With Materials and Atoms* **193**, 283–287((2002).

[228] Primak, W. Fast-neutron-induced changes in quartz and vitreous silica. *Physical Review* **110**, 1240–1254 (1958).

[229] Khan, H. A. Natural quartz - useful detector for in-core measurements. *Nuclear Instruments and Methods* **128**, 245–250 (1975).

[230] Klaumunzer, S. Ion tracks in quartz and vitreous silica. *Nuclear Instruments and Methods In Physics Research Section B-beam Interactions With Materials and Atoms* **225**, 136–153 (2004).

[231] Spinner, S. Temperature dependence of elastic constants of vitreous silica. *Journal of the American Ceramic Society* **45**, 394–397 (1962).

[232] Bucaro, J. A. & Dardy, H. D. High-temperature brillouin-scattering in fused quartz. *Journal of Applied Physics* **45**, 5324–5329 (1974).

[233] Ohno, I., Harada, K. & Yoshitomi, C. Temperature variation of elastic constants of quartz across the alpha-beta transition. *Physics and Chemistry of Minerals* **33**, 1–9 (2006).

[234] Nye, J. F. Physical properties of crystals. *Oxford University Press, Oxford, UK* (1957).

[235] Kittel, C. Introduction to solid state physics. *John Wiley and Sons, New York* (1968).

[236] Nishi, K., Yamaguchi, A. A., Ahopelto, J., Usui, A. & Sakaki, H. Analyses of localized confinement potential in semiconductor strained wires and dots buried in lattice-mismatched materials. *Journal of Applied Physics* **76**, 7437–7445 (1994).

[237] Grundmann, M., Stier, O. & Bimberg, D. InAs/GaAs pyramidal quantum dots - strain distribution, optical phonons, and electronic-structure. *Physical Review B* **52**, 11969–11981 (1995).

[238] *http://www.almazoptics.com/Quartz.htm* .

[239] Bruckner, R. Properties and structure of vitreous silica I. *J. Non-Crystaline Solids* **5**, 123–175 (1970).

[240] Mukherjee, G. D., Vaidya, S. N. & Sugandhi, V. Direct observation of amorphous to amorphous apparently first-order phase transition in fused quartz. *Physical Review Letters* **87**, 195501 (2001).

[241] Green, P. F., Duddy, I. R., Gleadow, A. J. W., Tingate, P. R. & Laslett, G. M. Fission-track annealing in apatite - track length measurements and the form of the arrhenius plot. *Nuclear Tracks and Radiation Measurements* **10**, 323–328 (1985).

[242] Sandhu, A. S., Singh, S. & Virk, H. S. Anisotropic track annealing in apatite. *Mineralogical Journal* **13**, 307–313 (1986).

[243] Crowley, K. D. & Cameron, M. Annealing of etchable fissiontrack damage in apatite: Effects of anion chemistry. *Geological Society of America Abstracts with Programs* **19**, 631–632 (1987).

[244] Donelick, R. A. Crystallographic orientation dependence of mean etchable fission-track length in apatite - an empirical-model and experimental-observations. *American Mineralogist* **76**, 83–91 (1991).

[245] Sandhu, A. S., Singh, L., Ramola, R. C., Singh, S. & Virk, H. S. Annealing kinetics of heavy-ion radiation-damage in crystalline minerals. *Nuclear Instruments and Methods In Physics Research Section B-beam Interactions With Materials and Atoms* **46** (1990).

[246] Schnohr, C. S., Kluth, P., Byrne, A. P., Foran, G. J. & Ridgway, M. C. Comparison of the atomic structure of inp amorphized by electronic or nuclear ion energy-loss processes. *Physical Review B* **77**, 073204 (2008).

[247] Vukadinovic, D. & Edgar, A. D. Phase-relations in the phlogopite-apatite system at 20 kbar - implications for the role of fluorine in mantle melting. *Contributions To Mineralogy and Petrology* **114**, 247–254 (1993).

[248] Fleischer, R. L., Price, P. B., Walker, R. M. & Maurette, M. Origins of fossil charges-particle tracks in meteorites. *Journal of Geophysical Research* **72**, 331 (1967).

[249] Plieninger, T., Kratschmer, W. & Gentner, W. Charge assignment to cosmic ray heavy ion tracks in lunar pyroxenes. *Proc. 3rd Lun. Sci. Conf.* 2933–2939 (1972).

[250] Price, P. B., Lal, D., Tamhane, A. S. & Perelygin, V. P. Characteristics of tracks of ions of $14 \leq z \leq 36$ in common rock silicates. *Earth and Planetary Science Letters* **19**, 377–395 (1973).

[251] Green, P. F., Bull, R. K. & Durrani, S. A. Particle identification from track-etch rates in minerals. *Nuclear Instruments and Methods* **157**, 185–193 (1978).

[252] Bull, R. K. & Durrani, S. A. Cosmic-ray tracks in shalka meteorite. *Earth and Planetary Science Letters* **32**, 35–39 (1976).

[253] Bull, R. K. & Durrani, S. A. Studies of fresh and fossil tracks in meteoritic hypersthene. *Nuclear Track Detection* **1**, 75–80 (1977).

[254] Haggerty, S. E. & Baker, I. The alteration of olivine in basaltic and associated lavas. part I: High temperature alteration. *Contributions to Mineralogy and Petrology* **16**, 233–257 (1967).

[255] Kondoh, S., Kitamura, M. & Morimoto, N. Synthetic laihunite (classxfe-2/2+)-3xfe-2x(3+)sio4), an oxidation-product of olivine. *American mineralogist* **70**, 737–746 (1985).

[256] Donelick, R. A. & Carlson, W. D. Variability of apatite fission-track annealing kinetics: Crystallographic orientation effects. *American Mineralogist* **85**, 1565–1565 (1999).

[257] Brix, M. R., Stockhert, B., Seidel, E., Theye, T., Thomson, S. N. & Kuster, M. Thermobarometric data from a fossil zircon partial annealing zone in high pressure-low temperature rocks of eastern and central crete, greece. *Tectonophysics* **349**, 309–326 (2002).

[258] Wendt, A. S., Vidal, O. & Chadderton, L. T. Experimental evidence for the pressure dependence of fission track annealing in apatite. *Earth and Planetary Science Letters* **201** (2002).

[259] Yamada, K., Tagami, T. & Shimobayashi, N. Experimental study on hydrothermal annealing of fission tracks in zircon. *Chemical Geology* **201**, 351–357 (2003).